

FINAL TECHNICAL REPORT

Asia Pacific Research Initiative for Sustainable Energy Systems

Office of Naval Research

Grant Award Number N00014-16-1-2116

March 1, 2016 through December 31, 2020



March 2021

Table of Contents

EXECUTIVE SUMMARY.....	1
TASK 1: PROGRAM MANAGEMENT AND OUTREACH.....	3
TASK 2: FUEL CELL, BATTERY, FILTRATION AND HYDROGEN RESEARCH	3
2.1 Development and Testing of Membrane-Based Energy Systems	4
2.2 Evaluation and Modeling of Commercial Battery Systems	10
2.3 Purification Technology	16
2.4 Hydrogen Refueling Support	23
2.5 Printable Photovoltaics.....	27
TASK 3: BIOFUELS	30
3.1 Bioenergy Systems	30
3.2 High-Rate Anaerobic Digestion	31
3.3 Liquid Fuels from Syngas	34
3.4 Marine Fuels.....	42
TASK 4: METHANE HYDRATES	43
TASK 5: SECURE MICROGRIDS	59
5.1 Moloka‘i Dynamic Load Bank.....	60
5.2 Conservation Voltage Reduction Demonstration.....	65
5.3 Coconut Island DC Microgrid.....	71
5.4 Bi-Directional EV Charging Demonstration Project	77
5.5 Hawai‘i BESS + PV Virtual Power Plant Demonstration	81
5.6 Power Grid Monitoring and Controls.....	87

5.7 Real-Time Health Assessment of Distribution Transformers	90
5.8 Automated Distribution Circuit PV Hosting Capacity Estimation	97
5.9 Load and PV Synthesis	99
5.10 Solar Forecasting.....	104
5.11 Marine Corps Base Hawai‘i Installation Energy Security Plan	114
TASK 6: OCEAN ENERGY.....	116
6.1 Ocean Thermal Energy Conversion (OTEC)	116
6.2 Wave Energy Advancement.....	117
TASK 7: ENERGY EFFICIENCY	121
7.1 Energy and Indoor Air Quality in Mixed Mode Buildings	121
7.2 Ceiling Fan and Thermal Comfort Assessment for Mixed-Mode Classrooms in Hawai‘i....	129

Final Technical Report
Asia Pacific Research Initiative for Sustainable Energy Systems
Grant Award Number N00014-16-1-2116
March 1, 2016 through December 31, 2020

EXECUTIVE SUMMARY

This report summarizes work conducted under Grant Award Number N00014-16-1-2116 the Asia Pacific Research Initiative for Sustainable Energy Systems 2015 (APRISES15), funded by the Office of Naval Research (ONR) to the Hawai‘i Natural Energy Institute (HNEI) of the University of Hawai‘i at Mānoa (UH). The work conducted under APRISES15 was intended to research, develop, test, and evaluate (RTD&E) distributed energy systems, novel energy technologies, and power grid integration using Hawai‘i as a model for applicability throughout the Pacific Region. APRISES15 comprised fuel cell research, contaminant mitigation and evaluation; seafloor methane hydrates destabilization; microbial degradation and reservoir mapping; synthetic fuels processing and production to accelerate the use of biofuels for Navy needs; alternative energy systems for electric power generation and integration into smart microgrids; and energy efficient building platforms. Testing and evaluation of alternative energy systems included Ocean Thermal Energy Conversion (OTEC), development of several microgrid test projects, and wind energy generation.

Under Task 1, Program Management and Outreach, HNEI senior faculty provided overall program management and coordination, developed and monitored partner and subcontract agreements, and developed outreach materials for both technical and non-technical audiences.

Task 2 technologies included for RDT&E included fuel cells and associated air purification technology, Li-ion batteries, hydrogen refueling infrastructure, and the development of new techniques for printed photovoltaic materials. HNEI continued to develop and apply fuel cell diagnostics to advance the understanding of fuel cell contamination mechanisms and to develop mitigation strategies for critical air contaminants. These efforts also included the development of ex-situ regenerable filtration materials. Testing and analysis included the development of new tools to better understand the performance of battery packs and analysis was extended to different grid connected battery systems, as well as Hydrogen Refueling Support, including ongoing support for the commissioning of hydrogen production and compression equipment and Hydrogen Transport Trailers (HTT) at the Natural Energy Laboratory of Hawai‘i Authority (NELHA) fueling station site. Finally, Task 2 also included a modest effort to continue the development of a novel low-cost printing process for the fabrication of electronic materials for photovoltaics.

Efforts under Task 3, Biofuels, includes several subtasks focused on the development, testing, and evaluation of alternative fuels and technologies. These included work to assess the feasibility of Pongamia (*Millettia pinnata*); completion of the laboratory development of a process for high rate anaerobic digestion and initiation of efforts to identify a suitable commercial partner; efforts to develop new technology to produce high-grade liquid fuels from syngas (H₂, CO, and CO₂) via the formation of polyhydroxybutyrate (PHB) from the gas substrates by using a chemoautotrophic microorganism and subsequent conversion of the PHB into hydrocarbon oil; and continuation of the work to characterize the storage and oxidation stabilities of catalytic hydrothermal produced diesel (CHCD-76), synthesized isoparaffin (SIP-76), and hydroprocessed renewable diesel (HRD-76) and their blends with F-76.

The three objectives of Task 4, Methane Hydrates, included advancing our understanding of the environmental impacts of natural seeps and accidental releases of methane and other hydrocarbons in the deep ocean; exploring the feasibility of sequestering CO₂ in natural methane hydrate reservoirs; and continue to promote international research collaborations on methane hydrates. Specific technical initiatives that were pursued to attain the above goals included the initiation of a laboratory study of hydrate formation on natural gas bubbles and bubble dissolution in seawater using the new HNEI high pressure water tunnel; continuation of laboratory experiments to identify microbial metabolic pathways that break down methane and other hydrocarbons in the ocean; calorimetric experiments to investigate the energetics and rates of CO₂-CH₄ hydrate exchange; and support to organize the 10th International Workshop on Methane Hydrate R&D.

Secure Microgrids, Task 5, included a broad range of projects to develop, test, and integrate secure microgrid technologies. Projects conducted under Task 5 included the Moloka‘i Dynamic Load Bank; Conservation Voltage Reduction Demonstration; the Coconut Island DC Microgrid; a Bi-Directional EV Charging Demonstration Project; continued development of a Hawai‘i BESS + PV Virtual Power Plant Demonstration; development of advanced Power Grid Monitoring and Controls; new tools for Real-Time Health Assessment of Distribution Transformers; analysis of Automated Distribution Circuit PV Hosting Capacity Estimation; Load and PV Synthesis; continued progress and demonstration of a cost-effective Solar Forecasting methodology; and initiation of effort to develop a Marine Corps Base Hawai‘i Installation Energy Security Plan. Each of these are described in detail in the report below.

Task 6, Ocean Energy, supported two subawards: one to Makai Ocean Engineering to continue develop of thin foil heat exchangers (TFHX) and a second to the University of Alaska Fairbanks (UAF) to identify and evaluate techno-economic benefits or issues associated with integrating wave energy along with other variable renewable energy sources into small, isolated grid systems. Under APRISES15, Makai conducted performance testing of the TFHXs, expanding testing fluids to include air in the external channels and installed air-water testing apparatuses. Seawater-ammonia and seawater-seawater performance testing was also conducted at the 100 kW test station

and the first commercial TFHX unit was installed at Cyanotech. In their small grid analysis, UAF used a mix of tools including the Hybrid Optimization of Multiple Energy Resources (HOMER) model, the UAF-developed Micro Grid Renewable Integration Dispatch and Sizing (MiGRIDS) package, and a Mathworks Simulink-based model to explore the integration of wave energy into a small grid.

Under Energy Efficiency Task 7, HNEI completed its ongoing effort to characterize the performance/comfort of the second generation FROGs constructed at UH Mānoa. In the first subtask, HNEI conducted a study to measure energy performance and CO₂ concentrations in two Hawai‘i classrooms to determine the impact of user decision-making on adequacy of fresh air and on CO₂ concentration. In the second subtask, both subjective and objective data were collected over a period of two years to comprehensively describe fan performance, fan control preferences, and occupant responses to thermal conditions, with the objective to compare user perceptions with comfort model predictions using measured conditions.

This report describes the work that has been accomplished under each of these tasks, along with summaries of task efforts that are detailed in journal and other publications, including reports, conference proceedings, presentations, and patent applications. **Publications produced through these efforts are listed and available, or linked, on HNEI’s website at <https://www.hnei.hawaii.edu/publications/project-reports/aprises-15>.**

TASK 1: PROGRAM MANAGEMENT AND OUTREACH

This program-wide task provided management and coordination of all research, test, development, and evaluation efforts under APRISES15. Partner and subcontract agreements were developed and monitored, and outreach materials for both technical and non-technical audiences were developed. Additional detail for partner, subcontract, and outreach activities are included in the following task summaries.

TASK 2: FUEL CELL, BATTERY, FILTRATION AND HYDROGEN RESEARCH

Activities under Task 2 included the development and testing of membrane-based energy systems (primarily fuel cells), continued evaluation and modeling of commercial Li-ion battery systems, the development of regenerative air filtration materials, continued support of the development of hydrogen refueling infrastructure on the Big Island of Hawai‘i, and funded efforts to develop novel thin film materials (primarily Cu₂ZnSn(S,Se)₄: CZTSSe) for solar energy conversion using

inexpensive and scalable liquid-based processing. Details for each of these tasks are described in more detail below.

2.1 Development and Testing of Membrane-Based Energy Systems

Development and testing of membrane-based energy systems included activities in support of the Naval Research Laboratory's (NRL) efforts to develop fuel cells for unmanned aerial vehicles and transfer the technology to the licensee Northwest UAV; to secure intellectual property for a recovery method for fuel cells exposed to sulfur and halogen species present in air; and to continue the characterization of contaminant effects to support the development of mechanisms needed to devise mitigation strategies for fuel cells.

Key accomplishment and details of the work conducted in each of these areas are described below. Patents, publications and presentations are referenced at the end of this section.

Support to NRL

Under APRISES15, HNEI continued its collaboration with NRL's team to determine the potential of stamped metal bipolar plates to reduce volume and weight of fuel cell power systems to meet flight requirements and to improve the manufacturability of system components for unmanned aerial vehicles (UAV). This work included the development and testing of new materials for improving the performance of NRL UAV fuel cell and balance of plant subsystems as well as testing of COTS components. The main focus of this work was the evaluation of next generation fuel cells stacks built at NRL with metal bipolar plates to characterize design conformity and performance uniformity. Build issues were identified, and optimal operating conditions and stack orientation with respect to the aerial vehicle chassis and reactant configurations were also determined and reported to NRL. As the fuel cell stack testing and evaluation results are not approved for public release, no data or discussion of results is presented in this report. For more information on the fuel cell stack development program at NRL contact Karen Swider-Lyons at karen.lyons@nrl.navy.mil.

Prior fuel cell materials development work performed in collaboration with NRL under APRISES14 has now been published and/or presented and is listed below. In addition to the testing and evaluation conducted in support of NRL, in January of 2020, HNEI led a one week hands-on training course in Honolulu for two engineers from Northwest UAV, the licensee of NRL fuel cell stack designs. The training included dissemination of information on facility development, safety protocols, fuel cell stack handling and installation, test equipment development, and HNEI/NRL fuel cell testing protocols. Future work at HNEI will continue our collaboration with NRL, but

focus will be shifted from high-performance fuel cells to attritable, low cost fuel cell designs for both high temperature and low temperature PEMFCs for Navy applications.

Contaminant Mitigation

Under previous funding, a wide range of air contaminants in PEMFCs were investigated with both single cells and stacks. Most of the compounds tested were found to adsorb and react on the Pt catalyst surface and compete with the oxygen reduction reaction reducing cell performance. Fortunately, the effects of both unsaturated hydrocarbons and oxygen-containing hydrocarbon contaminants were found to be mitigated by neat air operation. However, for sulfur and halogen compounds, the cell performance suffers a significant loss and does not recover after neat air operation. Under long-term operation, the adsorption of anions on the catalyst surface also causes permanent damage to the membrane/electrode assembly, such as Pt dissolution and particle growth, and ionomer electrolyte decomposition. Techniques for restoration of performance in single cells such as potential scanning is not applicable to stacks because potential control at the cell level is required, which multiplies electrical connections and increases system volume. On the other hand, currently available chemical filters have a limited life requiring intermittent replacement.

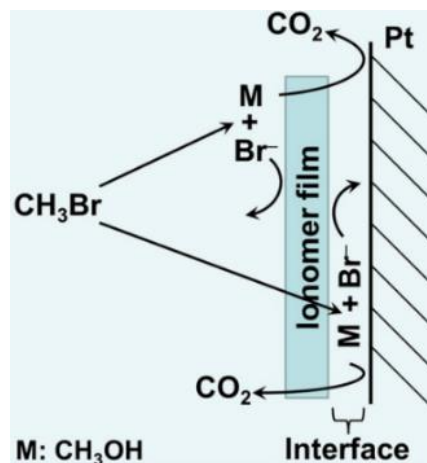


Figure 2.1.1. Contamination mechanisms of bromomethane in PEMFC cathode [1].

Under previous work, an in-situ recovery strategy using oxidant gases (such as nitrous oxide, N_2O and ozone O_3) was evaluated to restore PEMFCs poisoned by traces of sulfur dioxide, bromomethane, and hydrogen chloride in air. Unfortunately, experimental results indicated that pure N_2O is inefficient to oxidize adsorbates due to the low open circuit voltage (OCV) of ~0.75 V, which also corresponds to a cathode potential of ~0.75 V versus the hydrogen reference electrode. In contrast, O_3 is too potent (the OCV and cathode potential reach values of 1.51 V and 1.51 V versus the hydrogen reference electrode with 1000 ppm O_3 in air), which causes permanent damage to the catalyst layer and further increases cell voltage losses.

Building on work initiated under APRISES14, HNEI has developed a stack compatible performance recovery method that incorporates a combination of in-situ operations. Specific procedures are based on a comprehensive understanding of the contamination mechanisms illustrated in Figure 2.1.1. The method, validated using single cells, was shown to restore the performance losses and remove the adsorbates and anions after poisoning with bromomethane, sulfur dioxide, or hydrogen chloride. The cell performance was respectively restored to 100%, 99%, and 97% of the initial cell voltage value for those contaminants. A United States provisional patent was filed. Representative results of recovery experiments with PEMFCs poisoned by bromomethane and sulfur dioxide were reported in the APRISES14 final technical report. The results of hydrogen chloride contamination and recovery experiments are shown in Figure 2.1.2. Figures 2.1.2a, b, and c illustrate cell performance transients, cathode cyclic voltammetry profiles and polarization curves, before and after a temporary hydrogen chloride exposure and recovery. Figure 2.1.2a shows that the cell voltage that is initially constant at 0.65 V before the introduction of 50 ppm hydrogen chloride at approximately 5 h, is gradually reduced by approximately 35% over a period of 3 h. At approximately 11 h, neat air circulation is restored, which leads to a small cell voltage recovery after 12 h (from ~11 to ~23 h) of operation. The cell performance was increased to approximately 78% of its initial value. These cell performance responses to hydrogen chloride exposure are consistent with literature reports [1]. However, after the recovery operation (period marked as “recovery”), the cell voltage was further restored to 97% of its initial value. The cyclic voltammetry profiles in Figure 2.1.2b show similar features before contamination and after recovery with the exception of a reduced number of active platinum sites (reduced currents in the 0.1 to 0.4 V vs. HRE range). These results indicate that contaminants/adsorbates were almost completely removed from the catalyst layer. The irrecoverable electrochemical active area loss is attributed to Pt dissolution and the formation of soluble chloride complexes [2]. Figure 2.1.2c polarization curves also indicate that the cell performance was almost completely recovered. The lower performance at low current densities and slightly higher performance at high current densities is ascribed to a permanent catalyst nanoparticle reconstruction (dissolution and redeposition). Key recovery method details are avoided to protect the intellectual property.

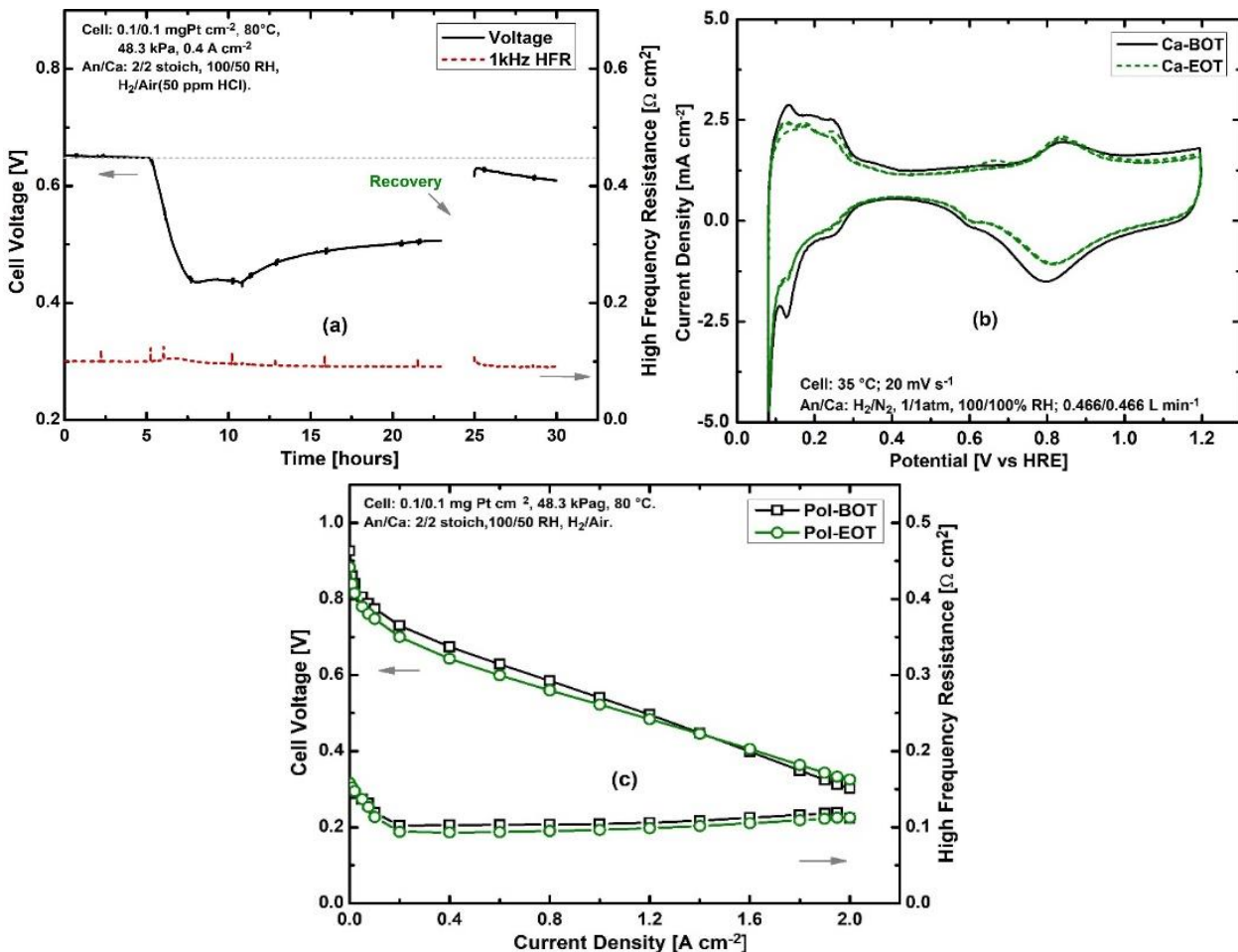


Figure 2.1.2. Cell voltage response (black curve) to a temporary hydrogen chloride exposure followed by recovery periods with neat air and changes in operating conditions (a). Cathode cyclic voltammetry profiles before contamination (Ca-BOT) and after recovery (Ca-EOT) (b). Polarization curves before contamination (Pol-BOT) and after recovery (Pol-EOT) (c). HFR: high frequency resistance, An/Ca: anode/cathode, stoich: stoichiometry, RH: relative humidity.

Under a future APRISES award, the method's effectiveness with commercially relevant fuel cell stacks will be evaluated. A collaboration with a PEMFC stack or system manufacturer involved in fuel cell vehicle demonstrations will be sought to further validate the efficiency of the recovery method for contaminated PEMFC stacks.

Testing conducted under previous funding indicated that oxygen mass transfer losses were systematically accompanied by oxygen reduction kinetic losses. It was originally hypothesized that contaminant adsorption on carbon materials (gas diffusion and microporous layers, catalyst support) would disrupt product water management by creating more hydrophilic surfaces and increasing the extent of flooding. Under APRISES11, neutron radiography at the National Institute of Standards and Technology (NIST) revealed subtle changes in cell water content. Under this subtask, two other methods that are sensitive to oxygen mass transfer losses were used at HNEI to clarify NIST results: polarization curves using different oxidants (oxygen, air, and a mixture of

oxygen in helium with the same 21% volume fraction as air), limiting currents obtained with low oxygen concentrations (1 to 7%) and oxygen diluents (helium, nitrogen, carbon dioxide). Results indicated that gas phase transport processes (molecular and Knudsen diffusion) were not affected by contaminants (Figure 2.1.3). Additionally, only the oxygen transport resistance through the ionomer covering the platinum catalyst was affected (Figure 2.1.3). This information was sufficient to formulate a mechanism. Contaminants adsorbed on the catalyst surface decrease the active surface area and increase both the real current density and the oxygen reduction kinetic overpotential, which is denoted as the charge transfer resistance in Figure 2.1.3. The smaller active surface area also brings the real current density closer to the limiting value, inducing an increase of the mass transfer overpotential connected with oxygen movement in the ionomer layer covering the catalyst. As mass transfer losses are intimately linked to kinetic losses, they are challenging to eliminate. Potential solutions include catalysts that do not adsorb contaminants of interest and ionomers that selectively transport oxygen.

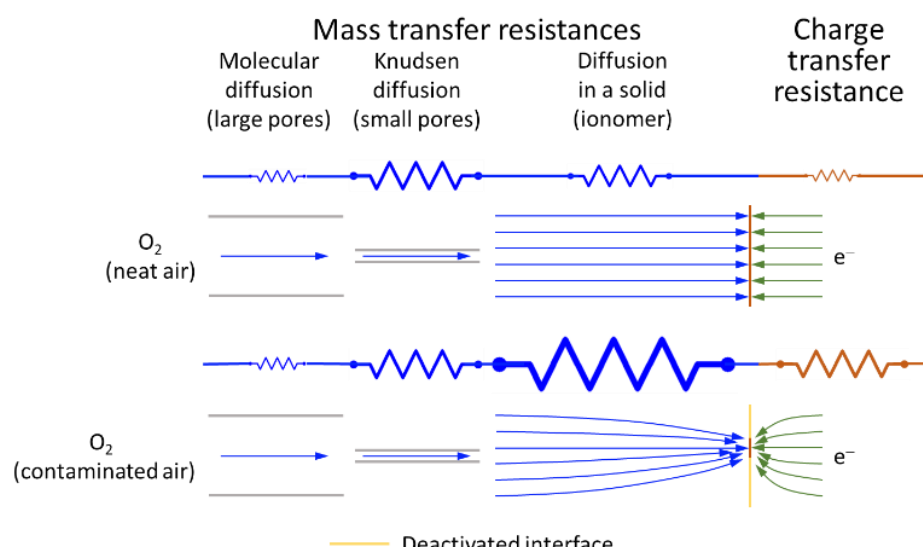


Figure 2.1.3. Oxygen mass transfer path from the flow field channel to the catalyst surface and associated resistances (in blue). The electron charge transfer path is also indicated (in green). The relative importance of the different mass and charge transfer processes is approximately indicated by the size of each resistance.

The proposed mechanism was supported by modeling focused on contaminant and oxygen processes occurring in parallel on the catalyst surface (adsorption, reaction, desorption). Additional details are contained in the publication listed at the end of this section.

Patents

1. Zhai, Y. and St-Pierre, J. Operation Method for Recovering Proton Exchange Membrane Fuel Cells Performance Losses due to Contamination, United States provisional patent 62/915,259, October 15, 2019.

Publications and Presentations

Peer-Reviewed Publications

1. Garsany, Y., Bancroft, C.H., Atkinson III, R.W., Bethune, K., Gould, B.D., and Swider-Lyons, K.E. (2020). Effect of GDM Pairing on PEMFC Performance in Flow-Through and Dead-Ended Anode Mode. *Molecules*, 25, 1469.
2. St-Pierre, J. and Zhai, Y. (2020). Impact of the Cathode Pt Loading on PEMFC Contamination by Several Airborne Contaminants. *Molecules*, 25, 1060.
3. Bethune, K., St-Pierre, J., LaManna, J.M., Hussey, D.S., and Jacobson, D.L. (2020). Contamination Mechanisms of Proton Exchange Membrane Fuel Cells - Mass Transfer Overpotential Origin. *Journal of Physical Chemistry C*, 124(44), 24052-24065.

Conference Proceedings and Presentations

1. Zhai, Y. and St-Pierre, J. (2020). Acetonitrile Contamination and Recovery of PEMFCs. 238th Electrochemical Society Meeting (PRiME 2020), Held virtually, October 4-9, 2020, Abstract 2194.
2. Bethune, K., St-Pierre, J., LaManna, J.M., Hussey, D.S., and Jacobson, D.L. Contamination Mechanisms of Proton Exchange Membrane Fuel Cells - Mass Transfer Overpotential Origin. 238th Electrochemical Society Meeting (PRiME 2020), Held virtually, October 4-9, 2020, Abstract 2195.
3. Atkinson, R.W., Garsany, Y., Bethune, K., St-Pierre, J., Gould, B.D., and Swider-Lyons, K. (2019). Pairing Asymmetric Gas Diffusion Media for High-Power Fuel Cell Operation. 236th Electrochemical Society Meeting, Atlanta, Georgia, October 13-17, 2019, Abstract 1428.
4. Garsany, Y., Atkinson, R.W., Bethune, K., St-Pierre, J., Gould, B.D., and Swider-Lyons, K. (2019). Cathode Catalyst Layer Design with Graded Porous Structure for Proton Exchange Membrane Fuel Cells. 236th Electrochemical Society Meeting, Atlanta, Georgia, October 13-17, 2019, Abstract 1423.
5. Zhai, Y. and St-Pierre, J. (2019). PEMFC Performance Recovery from Air Pollutants Contamination. 236th Electrochemical Society Meeting, Atlanta, Georgia, October 13-17, 2019, Abstract 1493.

References

- [1] Hawai‘i Natural Energy Institute. (2018). Asia Pacific Research Initiative for Sustainable Energy Systems (APRISES) 2013: Final Technical Report. Retrieved from <https://www.hnei.hawaii.edu/wp-content/uploads/APRISES-12-Final-Technical-Report.pdf>.

- [2] Baturina, O., Epshteyn, A., Northrup P., and Swider-Lyons, K. (2011). Insights into PEMFC Performance Degradation from HCl in Air. Journal of the Electrochemical Society, 158, B1198-B1205.

2.2 Evaluation and Modeling of Commercial Battery Systems

Under this subtask, battery testing and modeling focused on three topics: 1) the performance assessment of the lithium-ion titanate battery technology for grid power applications, 2) the modeling of battery packs, and 3) the durability and reliability of electric vehicle batteries (EV) under electric utility grid operations. Testing was conducted at HNEI's Hawai'i Sustainable Energy Research Facility (HiSERF). Cell performance was modeled using tools developed under previous APRISES funding, while a new approach for the modeling of battery packs was developed. Key accomplishment and details of the work conducted are described below. Associated publications and presentations are referenced at the end of this section.

Battery Durability under Power Systems Operation

Under this activity, analysis of data on Generation 1 Altairnano lithium titanate cells, collected under prior funding, was concluded. The impacts of calendar aging as well as current, depth of discharge and temperature on the state of health of the cells were studied using the design of experiment methodology. The primary objective of this subtask was to better understand battery degradation associated with the usage of a real battery energy storage system (BESS) in the field. From the analysis of three years of real usage, we studied the impact of different stress factors on battery degradation. It was found that temperature and current increase had a detrimental effect on capacity retention. It was also found that capacity faded faster on an exchanged capacity basis for smaller state of charge (SOC) swings. Finally, no compounding interactions were identified between the three stress factors. Regarding calendar aging, the cells did not degrade significantly when kept below 35°C, but deteriorated from exposure to temperatures above 45°C especially if left at low SOC.

Under APRISES15, the origin of the capacity loss and its sensibility to different stress factors was investigated using non-destructive methodologies that allowed remaining useful life determination. This work was unique because of the blended nature of the positive electrode (PE) in the Altairnano Generation 1 battery which consists of Lithium Cobalt Oxide (LCO) and Lithium Nickel Aluminum Cobalt Oxide (NCA) in a 45/55% ratio. Traditional analysis of battery degradation considers each electrode as a single unit. In this work, and for the first time in literature, we separated the contribution of each component of the blend to the overall degradation of the cell in order to forecast durability. We found that the degradation was highly dependent on usage and that the mix of loss of active material (LAM) on both components of the positive

electrode, on the negative electrode (NE), as well as the loss of lithium inventory (LLI) was unique for each of the condition tested (Figure 2.2.1). In all cases, the experimental capacity loss was induced by losses at the negative electrode, but our modeling of the degradation indicates that, in the long run, the degradation of the NCA part of the PE could become prominent and accelerate capacity fading, especially for high-usage cells. Some cells were forecasted to show acceleration in the degradation after less than three years of usage (Figure 2.2.2), significantly less than the anticipated lifespan of grid deployed batteries. This effort was published in the Journal of the Electrochemical Society (Baure, 2019). In future work, we intend to analyze data from the field deployed BESS to establish whether some of the modules are on a path where the degradation will be accelerated.

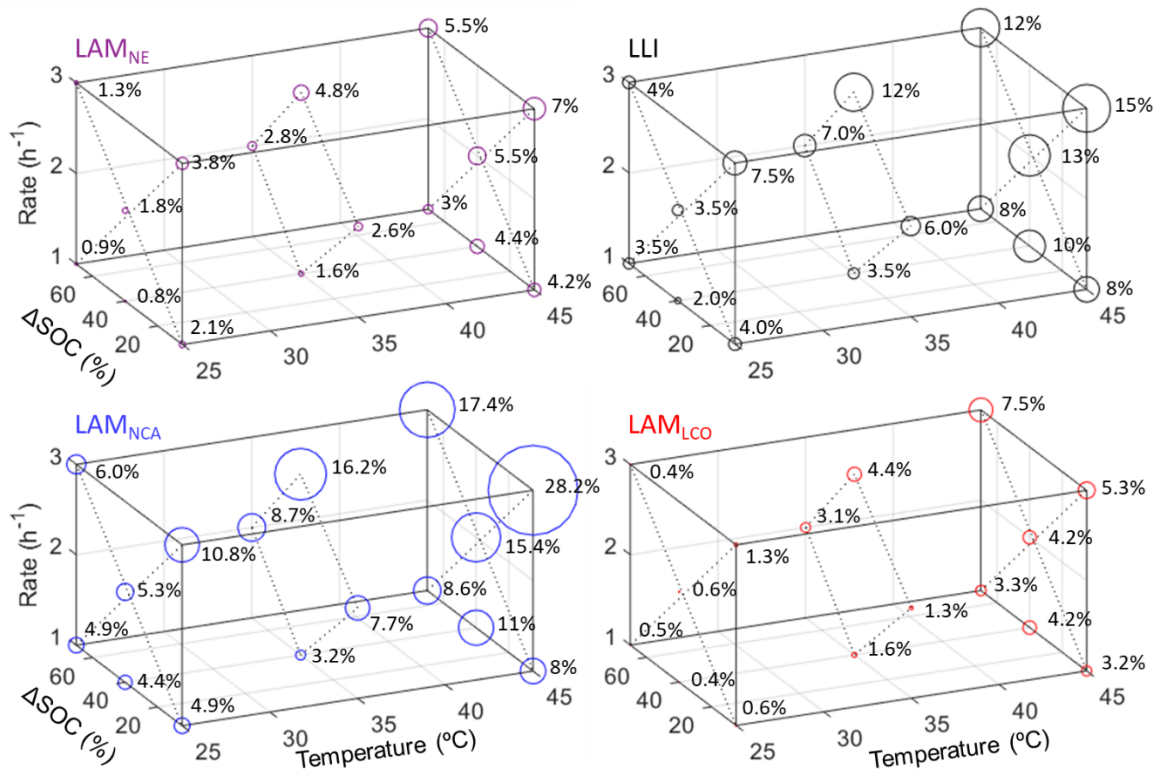


Figure 2.2.1. Degradation mechanisms vs. cycling conditions.

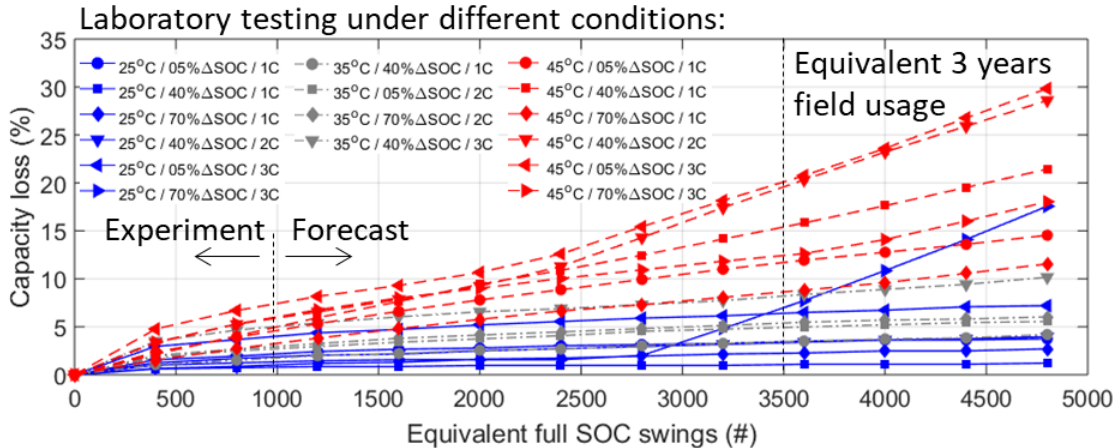


Figure 2.2.2. Evolution of forecasted capacity loss for all the tested conditions.

Battery Energy Storage System Modeling: A Combined Comprehensive Approach

Models for battery packs are essential to improve the understanding of BESS, whether for transportation or grid storage. It is an extremely complex task as BESS can be composed of thousands of cells that are not identical and do not degrade homogeneously. Most of the accurate single cell models use first principles electrochemical model or stochastic approaches. Although accurate, and despite recent work on reduced ordered models, these models are not convenient to scale up to the pack level because of calculation cost for modeling every single cell individually. To deal with the added complexity of handling multiple cells, most battery pack models are using multiple equivalent circuit models (ECM) connected in series or parallel. Such models are not accurate and lack the modularity necessary to investigate homogeneity issues and complex battery degradation.

In this work, a new modular methodology for battery pack modeling was defined. This BESS model was dubbed *hanalike* after the Hawaiian word for “all together” because it is unifying various models proposed and validated in recent years. It comprises an ECM with an add-on to handle cell-to-cell variations, a model that can link voltage response and degradation, a model that can handle paralleling, a model that can quantify imbalance, and a model for online SOC and SOH estimation (Figure 2.2.3). Details are available in the recent article in the Journal of Energy Storage (Dubarry, 2019).

Current work is focused on validating the modeling approach. The model output will be compared against real world data to predict performance of grid-scale energy storage systems. This is expected to provide valuable understanding for future BESS deployments.

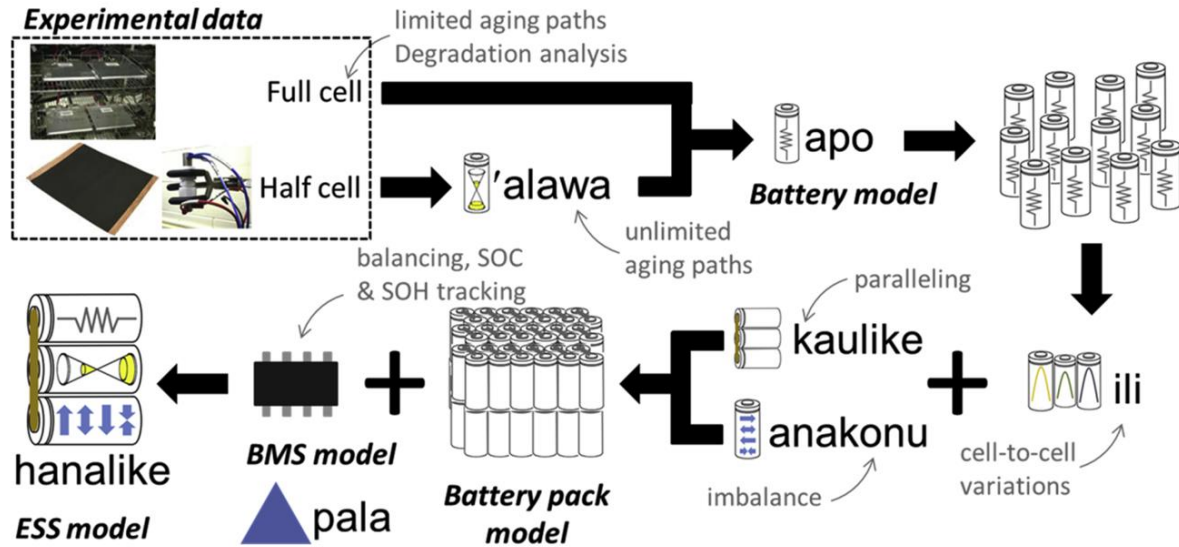


Figure 2.2.3. Evolution of forecasted capacity loss for all cells.

Durability of EV Batteries used for Grid Services

The use of EV batteries to assist the main electric grid for the storage of energy provided by intermittent sources has the potential to support the penetration of renewable energy into the electric grid. In APRISES12, we showed negative impact of using EV for energy shifting via vehicle to grid (V2G) usage because of the additional usage of the cells. Since battery degradation is path dependent, additional work was undertaken under APRISES15 to assess the impact of a different grid application, frequency regulation, on the same cells. Our investigation elucidated the impact of frequency regulation under several conditions, including a new approach of modulating the charge so that the vehicle can perform grid applications without any additional battery usage. Each cycle began a driving cycle equated to about three hours of driving per day or about 3-times the typical American roundtrip commute. After the discharge, the cells were subjected to six different scenarios (Figure 2.2.4) with or without frequency regulation (FR). The FR schedule was scaled down from real data extracted from the Hawi COASTAL1 BESS. In addition, different levels of FR were also investigated, and the FR was introduced during the rest or during the charge. Each cycle was repeated 2,000 times.

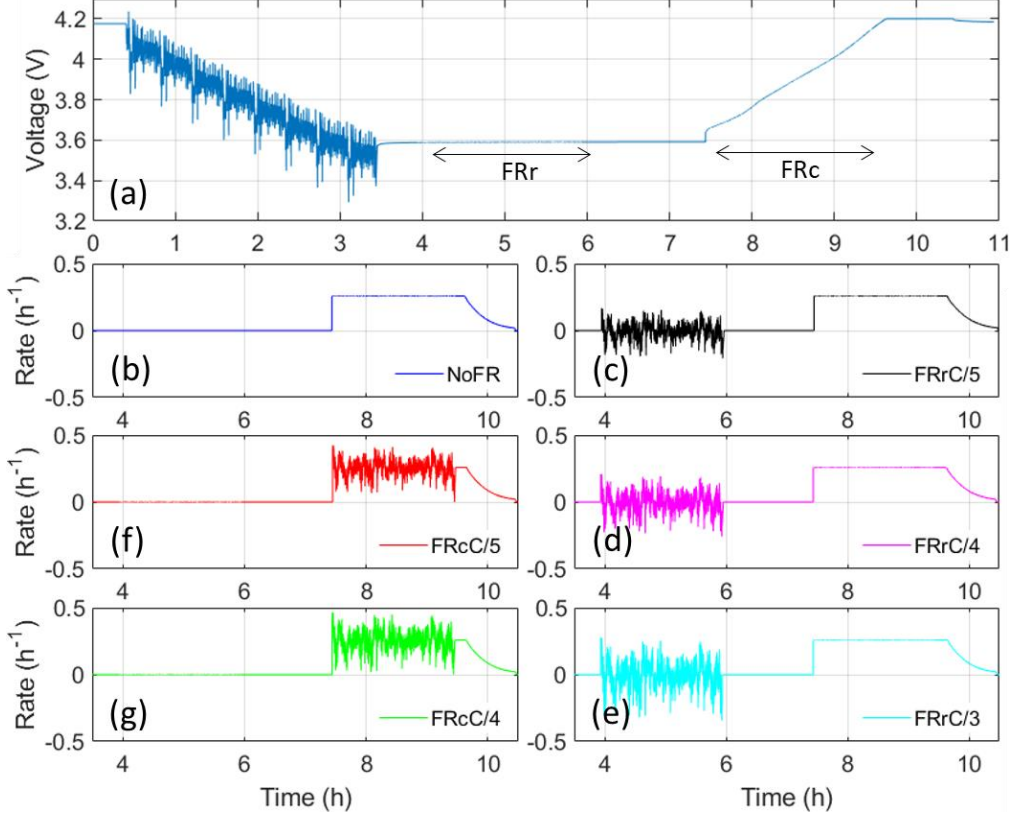


Figure 2.2.4. (a) Full duty cycle and (b-g) charge scenarios for each of the six duty cycles. noFR: no frequency regulation, FRc: frequency response during charge, and FRr: frequency regulation during rest.

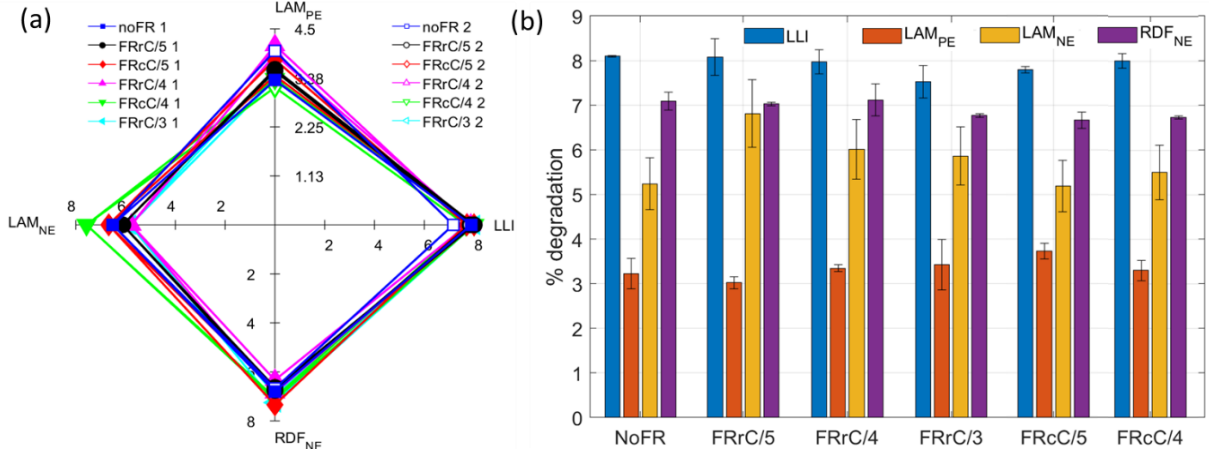


Figure 2.2.5. (a) Spider plots of the four prominent degradation modes for all the cells at 3,000 Ah (~8% capacity loss) and (b) bar plot showcasing the impact of the duty cycles. The error bar represents the spread between the two tested cells for each duty cycle, not a distribution of values.

The main takeaway from our study was that some frequency regulation V2G usage at moderate rates from C/3 to C/5 (full discharge in 3 to 5 hours) did not accelerate the cell degradation despite close to 15% additional usage (Figure 2.2.5). In addition, there was no noticeable difference between performing this ancillary service during rest or charge or at maximum current fluctuations

up to C/3 during rest and C/4 during charge. These results are extremely positive for the possible application of V2G/G2V strategies. However, it must be noted that our results hold for these specific cells and the duty cycle tested. More research is necessary to generalize the results.

Due to the similarity in the degradation between duty cycles, the benefits of modulating the charge to eliminate the additional usage on the cells could not be verified. Experiments on other chemistries with more aggressive usage will be planned. As for the diagnosis for the degradation, a new approach yielded four indicators for automatic diagnosis. This methodology will allow faster diagnosis and bolsters the value our approach for battery management system implementation. However, our study also showed that under some conditions, in our case the apparent kinetic limitations, some of the indicators may become ineffective with time. Therefore, proper validation using full fits and sensibility analysis to check for the range of efficacy of chosen FOI is still essential. Finally, some cells showcased accelerated aging and we were not able to predict it from the voltage variations. This suggested that it was not induced by a widespread degradation of the electrodes but was more likely because of localized effects. The cells that did not perform any frequency regulation seemed to be the most affected, but those results need to be moderated by the fact that the differences were probably within what to expect between cells performing the same duty cycles. This study was published as a feature article, invited by the editorial office in a special issue entitled “Electric Systems for Transportation” for the journal Energies (Baure, 2020).

Publications and Presentations

Peer-Reviewed Publications

1. Baure, G. and Dubarry, M. (2020). Durability and Reliability of EV Batteries under Electric Utility Grid Operations: Impact of Frequency Regulation Usage on Cell Degradation. *Energies*, 13(10), 2494.
2. Baure, G., Devie, A., and Dubarry, M. (2019). Battery durability and reliability under electric utility grid operations: Path dependence of Battery Degradation. *Journal of the Electrochemical Society*, 166(10), A1991-A2001.
3. Dubarry, M., Baure, G., Pastor-Fernández, C., Yu, T.F., Widanage, W.D., and Marco, J. (2019). Battery energy storage system modeling: A combined comprehensive approach, *Journal of Energy Storage*, 21, 172-185.

Conference Proceedings and Presentations

1. Dubarry, M. (2018). Battery Activities at the University of Hawai‘i. NELHA 2nd Conference on Energy Storage Trends and Opportunities, Kona, Hawai‘i, December 5-6, 2018.
2. Dubarry, M. (2018). Battery Activities at the University of Hawai‘i. 2nd Germany Hawai‘i Clean Energy Symposium, Honolulu, Hawai‘i, October 30, 2018.

3. Baure, G., Devie, A., and Dubarry, M. (2018). Battery Durability and Reliability Under Electric Utility Grid Operations: Representative Usage Aging. 234th Electrochemical Society Meeting, Cancun, Mexico, September 30 - October 4, 2018.

2.3 Purification Technology

The research under this subtask focused on the development of a novel method for the photocatalytic regeneration of activated carbon filtration materials saturated with sulfur dioxide. The ability to regenerate air filtration materials used in fuel cells on site (or ship), would reduce the quantity of materials needed for ship or forward operating base use and would reduce waste. Under this subtask, a novel surface treatment was developed to allow surface free radical generation under UV exposure. Titanium dioxide (TiO_2) was covalently bonded to the surface of granular activated carbon as a uniform nano-scale coating using nitric acid pretreatment and a hydrothermal reaction. The TiO_2 -functionalized active carbon was then tested for adsorption capabilities in low concentrations of sulfur dioxide and subsequently regenerated using the technique developed under this task. Once saturated with sulfur dioxide (SO_2), the media was regenerated using UV radiation while submerged in water to generate local free radicals which are theorized to attack the surface adsorbed SO_2 molecules. The regenerated material was then re-evaluated for adsorption capabilities and compared to its initial performance. The preliminary results showed that the nanoparticle coating resulted in an approximately 46% decrease in adsorption capacity, but regeneration for 20 hours was able to restore 87% of its initial capacity.

Major automobile manufacturers have been actively developing fuel cell vehicles to meet future transportation needs in a clean and sustainable way. A significant challenge to the application of fuel cells in vehicles is the performance degradation associated with air contamination from the environment. In particular, SO_2 concentrations as low as a few parts per million can result in severe performance losses in the cathode of a fuel cell [1]. Hence, effective air purification has the potential to extend fuel cell lifetime.

Granular activated carbon (AC), the most widely used sorbent material has exceptional adsorption abilities due to its high surface area and porosity. Moreover, the surface chemistry and porosity can be customized to specific adsorption processes. As the AC accumulates pollutant molecules, the adsorption capacity decreases, and the AC must either be disposed of as a hazardous waste or regenerated for reuse. Regeneration has the potential be more beneficial because of the lower waste production relative to single-use AC. In a techno-economic analysis on the role of sorbents in the adsorption of ambient carbon dioxide, the economics of the process was analyzed with respect to the carbon dioxide market price and the most critical sorbent characteristics (cycle time, loading capacity, and rate of degradation) [2]. The results showed that the sorbent must survive a

large number of adsorption-regeneration cycles in order to be economically viable, supporting the development of an effective regeneration process.

The conventional method of regenerating AC is through desorption at high temperatures ($\geq 900^{\circ}\text{C}$), a costly and often difficult to implement process. High temperature cycling can also cause carbon loss due to attrition and possible pore deformation, leading to limited adsorption cycles [3-5]. Another pathway for regeneration is decomposition regeneration, in which the surface-bound contaminants are degraded by either a chemical or physical reaction, which results in removal from the AC surface. Photocatalytic oxidation is attractive because of its simplicity, requiring only water and sunlight in the process.

The primary driver of photocatalytic systems is the photocatalyst, a semiconducting material capable of redox reactions when exposed to wavelengths of radiation specific to the catalyst properties. TiO_2 is an established photocatalyst because of its oxidative abilities and low cost. When exposed to wavelengths equal to or shorter than ultraviolet (UV) light, TiO_2 in aqueous solution forms electron-hole pairs that readily react with dissolved oxygen to form reactive oxygen species. This has been found to effectively degrade numerous pollutants, such as phenols, dyes, insecticides, and other organics [6-12].

Despite TiO_2 's remarkable oxidizing abilities, it has been shown to have low photocatalytic efficiencies due to the electron hole pairs recombining on the order of nanoseconds [13]. Many efforts have been made to enhance the efficiency of TiO_2 , including: coupling with metals and coupling with carbon materials [14-17]. When coupling TiO_2 with graphene oxide (GO), the recombination rate was observed to decrease [18]. Because of its high electron mobility, GO is able to function as an electron-sink and scavenge the generated free electrons in the conduction band of TiO_2 [19]. Coupling with graphene has also been shown to activate TiO_2 under longer wavelengths of visible light, though the precise explanations for this phenomenon are still unclear. Graphene oxide was utilized in this study to enhance the efficiency of TiO_2 [20,21].

Only a few studies have demonstrated the use of TiO_2 photocatalysis for SO_2 degradation [22-25]. In the work by Ao *et al.*, a TiO_2 -AC composite was simultaneously exposed to SO_2 and UV light, which resulted in an SO_2 removal of about 71%, which supports the feasibility of the proposed photocatalytic regeneration process [22].

Under this task, HNEI developed methods for synthesizing activated carbon coated with GO and TiO_2 (TGAC) and explored its technical feasibility in SO_2 adsorption and regeneration. Details of this synthesis are being withheld due to a pending patent application.

Surface morphology of particles was observed using SEM. Samples were mounted with conductive carbon tape on an aluminum stub, then viewed with a Hitachi S4800 Field Emission Scanning Electron Microscope at an accelerating voltage of 5.0kV.

Adsorption of SO₂

SO₂ adsorption was performed in a custom gas testbed, as shown in Figure 2.3.1. Purified air was mixed with SO₂ gas to produce a test concentration of 20 ppmv. Relative humidity (RH) was controlled with an upstream humidifier at 50% for all experiments. Adsorption isotherms were taken at 25°C. Samples were equilibrated with air (50% RH) overnight prior to and after SO₂ loading. SO₂ concentrations were measured with ENMET electrochemical sensors at the inlet and outlet of the sorbent bed. The breakthrough time was defined as the time it took for the outlet SO₂ concentration to reach 0.2 ppm. The breakthrough capacity was the amount of SO₂ adsorbed by the initial dry mass of the sorbent during the breakthrough period.

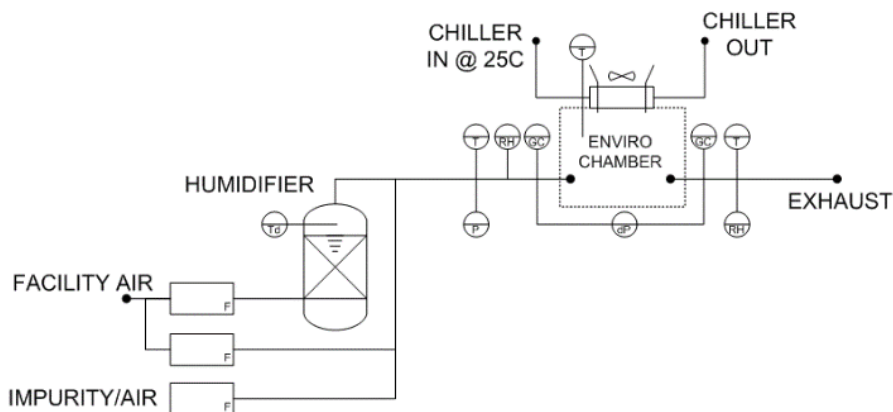


Figure 2.3.1. Schematic diagram of custom gas test bed used for SO₂ adsorption experiments.

The photocatalytic regeneration experiments were carried out in a simple apparatus that consisted of a glass tray (6.5 x 4.75 x 2 in) placed on a laboratory shaker exposed to two UVA lamps. Exhausted sorbents were regenerated immediately after removal from the test bed and transferred to the sample tray filled with 300 mL water. Before UV exposure, materials were stored in the dark for 30 minutes to attain adsorption equilibrium with the solution. The sample tray was exposed to UV light of 365 nm and 2100 μW/m² for 20 hours. The regenerated sorbents were rinsed until a stable pH was reached, then dried overnight. The regeneration efficiency (RE) was calculated using the equation below, where C_R and C₀ are the regenerated and initial breakthrough capacities.

$$RE = \frac{C_R}{C_0} \times 100\% \quad (\text{Eq. 2.3.1})$$

Results

The TiO₂ particles were found to be uniformly distributed on the AC granule (Figure 2.3.2a). Higher magnifications revealed slight TiO₂ (in white) agglomerations on the AC surface (in black) (Figures 2.3.2b and c). TiO₂ particle diameters were estimated in the SEM software where a small cluster and single particle was measured as 137 and 79 nm, respectively (Figure 2.3.2d). Since the

chemical properties of GO were similar to the bulk of the material (AC), it was unable to be detected in the SEM micrographs. The synthesis methods used were effective in uniformly distributing TiO₂ nanoparticles on the AC granules.

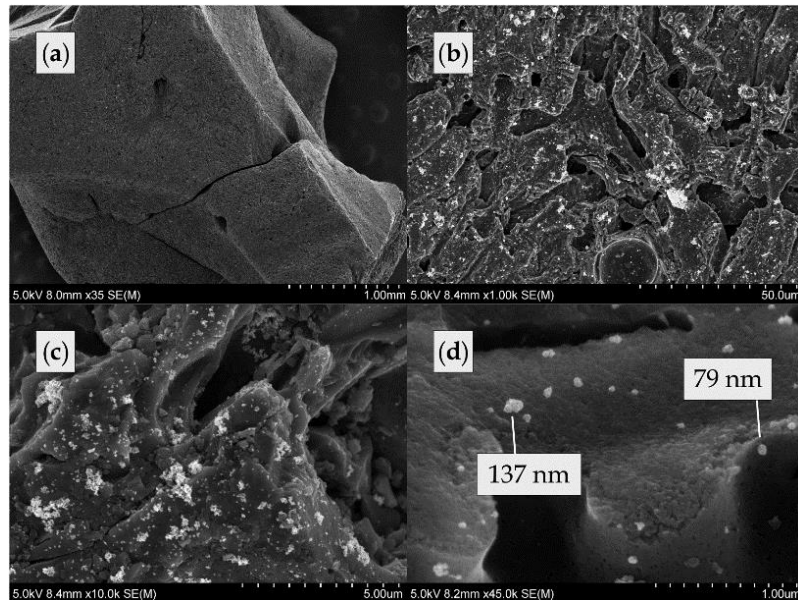


Figure 2.3.2. Scanning electron micrograph of TGAC: (a) single granule; (b,c) nano-scale TiO₂ coating with slight agglomerations; (d) TiO₂ particle size estimations.

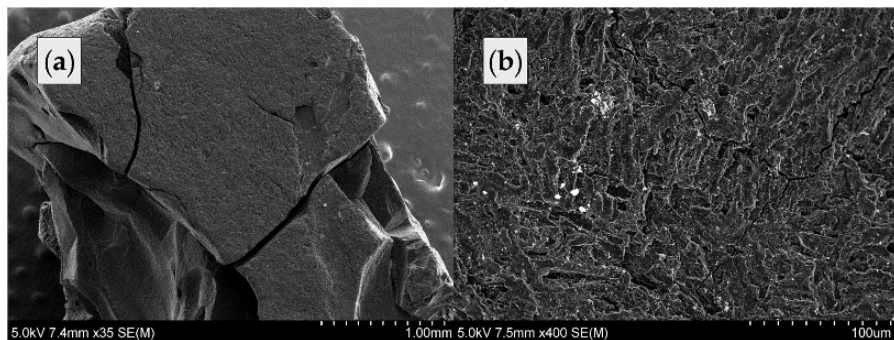


Figure 2.3.3. Scanning electron micrograph of preliminary TGAC: (a) single granule; (b) sparse TiO₂ agglomerations.

The breakthrough capacity of unaltered (pure) AC was measured as 0.139 g SO₂/g sorbent [g/g]. The initial and regenerated breakthrough capacities when regenerated with and without UV light are shown in Figure 2.3.4. The TiO₂ coating was found to reduce AC's adsorption abilities by about ~46%, exhibiting a breakthrough capacity of 0.075 g/g. The regeneration efficiency was calculated as 87%, where the regenerated capacity was 0.065 g/g. The experiment was repeated without UV exposure to identify the photocatalytic contributions. The regeneration efficiency of TGAC without UV exposure was 67%.

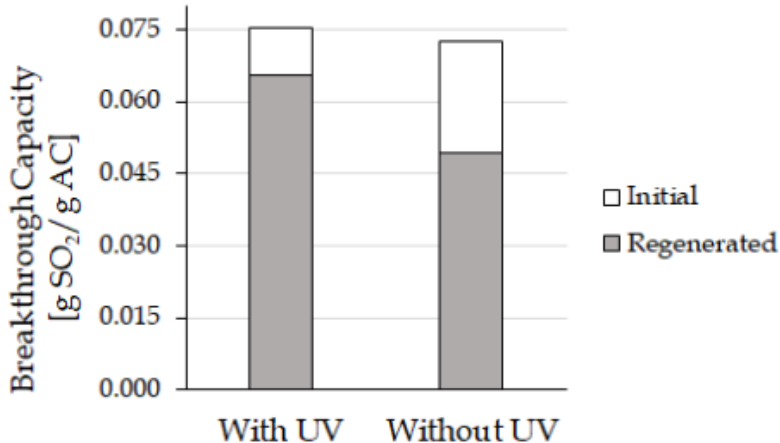


Figure 2.3.4. Initial and regenerated breakthrough capacity of TGAC with and without UV exposure.

In this work, hydrothermal synthesis of TGAC was shown effective in producing a nanoscale, uniform coating of TiO₂ onto the surface of oxidized AC. HNO₃ pretreatment was necessary to ensuring complete surface coverage by increasing the surface carboxyl groups on AC. Presence of TiO₂ decreased the adsorption capacity of AC from 0.139 to 0.075 g SO₂/g TGAC, corresponding to a 46% drop. Photocatalytic oxidation and water regeneration contributed to the overall regeneration of TGAC. Water regeneration provided a significant effect where a 67% RE was able to be obtained without any UV exposure. However, when exposed to UV light, an even higher RE of 87% was achieved and the respective photocatalytic mechanisms were speculated. The results from this study demonstrate the technical feasibility of photocatalytically regenerating SO₂ from AC.

References

- [1] Mohtadi, R., Lee, W-K., and Van Zee, J.W. (2004). Assessing durability of cathodes exposed to common air impurities. *Journal of Power Sources*, 138(1-2), 216-225.
- [2] Azarabadi, H. and Lackner, K.S. (2019). A sorbent-focused techno-economic analysis of direct air capture. *Applied Energy*, 250, 959-975.
- [3] Ledesma, B., Román, S., Álvarez-Murillo, A., Sabio, E., and González, J., (2014). Cyclic adsorption/thermal regeneration of activated carbons. *Journal of Analytical and Applied Pyrolysis*, 106, 112-117.
- [4] San Miguel, G., Lambert, S., and Graham, N. (2001). The regeneration of field-spent granular-activated carbons. *Water Research*, 35(11), 2740-2748.
- [5] Moreno-Castilla, C., Rivera-Utrilla, J., Joly, J.P., López-Ramón, M.V., Ferro-García, M.A., and Carrasco-Marín, F. (1995). Thermal regeneration of an activated carbon exhausted with different substituted phenols. *Carbon*, 33(10), 1417-1423.
- [6] Liu, S.X, Sun, C.L., and Zhang, S.R. (2004). Photocatalytic regeneration of exhausted activated carbon saturated with phenol. *Bulletin of environmental contamination and toxicology*, 73(6), 1017-1024.

- [7] Peiró, A.M., Ayllón, J.A., Peral, J., and Doménech, X. (2001). TiO₂-photocatalyzed degradation of phenol and ortho-substituted phenolic compounds. *Applied Catalysis B: Environmental*, 30(3-4), 359-373.
- [8] Le, H.A., Linh, L.T., Chin, S., and Jurng, J. (2012). Photocatalytic degradation of methylene blue by a combination of TiO₂-anatase and coconut shell activated carbon. *Powder Technology*, 225, 167-175.
- [9] Xing, B., Shi, C., Zhang, C., Yi, G., Chen, L., Guo, H., Huang, G., and Cao, J. (2016). Preparation of TiO₂/Activated Carbon Composites for Photocatalytic Degradation of RhB under UV Light Irradiation. *Journal of Nanomaterials*, 2016, 8393648.
- [10] Lu, M-C., Chen, J-N., and Chang, K-T. (1999). Effect of adsorbents coated with titanium dioxide on the photocatalytic degradation of propoxur. *Chemosphere*, 38(3), 617-627.
- [11] Matos, J., Laine, J., and Herrmann, J-M. (2001). Effect of the type of activated carbons on the photocatalytic degradation of aqueous organic pollutants by UV-irradiated titania. *Journal of Catalysis*, 200(1), 10-20.
- [12] Orha, C., Pode, R., Manea, F., Lazau, C., and Bandas, C. (2017). Titanium dioxide-modified activated carbon for advanced drinking water treatment. *Process Safety and Environmental Protection*, 108, 26-33.
- [13] Rothenberger, G., Moser, J., Graetzel, M., Serpone, N., and Sharma, D.K. (1985). Charge carrier trapping and recombination dynamics in small semiconductor particles. *Journal of the American Chemical Society*, 107(26), 8054-8059.
- [14] Moradi, S., Aberoomand-Azar, P., Raeis-Farshid, S., Abedini-Khorrami, S., Givianrad, M.H. (2016). The effect of different molar ratios of ZnO on characterization and photocatalytic activity of TiO₂/ZnO nanocomposite. *Journal of Saudi Chemical Society*, 20(4), 373-378.
- [15] Woo, S.H., Kim, W.W., Kim, S.J., and Rhee, C.K. (2007). Photocatalytic behaviors of transition metal ion doped TiO₂ powder synthesized by mechanical alloying. *Materials Science and Engineering: A*, 449-451, 1151-1154.
- [16] Yu, J., Ma, T., Liu, G., and Cheng, B. (2011). Enhanced photocatalytic activity of bimodal mesoporous titania powders by C₆₀ modification. *Dalton Transactions*, 40(25), 6635-6644.
- [17] Yu, J., Ma, T., and Liu, S. (2011). Enhanced photocatalytic activity of mesoporous TiO₂ aggregates by embedding carbon nanotubes as electron-transfer channel. *Physical Chemistry Chemical Physics*, 13(8), 3491-3501.
- [18] Liu, J., Bai, H., Wang, Y., Liu, Z., Zhang, X., and Sun, D.D. (2010). Self-assembling TiO₂ nanorods on large graphene oxide sheets at a two-phase interface and their anti-recombination in photocatalytic applications. *Advanced Functional Materials*, 20(23), 4175-4181.
- [19] Giovannetti, R., Rommozzi, E., Zannotti, M., and D'Amato, C.A. (2017). Recent advances in graphene based TiO₂ nanocomposites (GTiO₂Ns) for photocatalytic degradation of synthetic dyes. *Catalysts*, 7(10), 305.

- [20] Khalid, N., Ahmed, E., Hong, Z., Sana, L., and Ahmed, M. (2013). Enhanced photocatalytic activity of graphene–TiO₂ composite under visible light irradiation. *Current Applied Physics*, 13(4), 659-663.
- [21] Liu, S., Sun, H., Liu, S., and Wang, S. (2013). Graphene facilitated visible light photodegradation of methylene blue over titanium dioxide photocatalysts. *Chemical Engineering Journal*, 214, 298-303.
- [22] Ao, C. and Lee, S. (2004). Combination effect of activated carbon with TiO₂ for the photodegradation of binary pollutants at typical indoor air level. *Journal of Photochemistry and Photobiology A: Chemistry*, 161(2-3), 131-140.
- [23] Baltrusaitis, J., Jayaweera, P.M., and Grassian, V.H. (2011). Sulfur dioxide adsorption on TiO₂ nanoparticles: influence of particle size, coadsorbates, sample pretreatment, and light on surface speciation and surface coverage. *The Journal of Physical Chemistry C*, 115(2), 492-500.
- [24] Wang, H. and You, C. (2016). Photocatalytic removal of low concentration SO₂ by titanium dioxide. *Chemical Engineering Journal*, 292, 199-206.
- [25] Yuan, Y., Zhang, J., Li, H., Li, Y., Zhao, Y., and Zheng, C. (2012). Simultaneous removal of SO₂, NO and mercury using TiO₂-aluminum silicate fiber by photocatalysis. *Chemical Engineering Journal*, 192, 21-28.
- [26] Zhang, H., Lv, X., Li, Y., Wang, Y., and Li, J. (2010). P25-graphene composite as a high performance photocatalyst. *ACS Nano*, 4(1), 380-386.
- [27] Chen, J.P. and Wu, S. (2004). Acid/base-treated activated carbons: characterization of functional groups and metal adsorptive properties. *Langmuir*, 20(6), 2233-2242.
- [28] Figueiredo, J.L., Pereira, M., Freitas, M., and Orfao, J. (1999). Modification of the surface chemistry of activated carbons. *Carbon*, 37(9), 1379-1389.
- [29] Lu, X., Jiang, J., Sun, K., Xie, X., and Hu, Y. (2012). Surface modification, characterization and adsorptive properties of a coconut activated carbon. *Applied Surface Science*, 258(20), 8247-8252.
- [30] Ternero-Hidalgo, J.J., Rosas, J.M., Palomo, J., Valero-Romero, M.J., Rodríguez-Mirasol, J., and Cordero, T. (2016). Functionalization of activated carbons by HNO₃ treatment: Influence of phosphorus surface groups. *Carbon*, 101, 409-419.
- [31] Lisovskii, A., Semiat, R., and Aharoni, C. (1997). Adsorption of sulfur dioxide by active carbon treated by nitric acid: I. Effect of the treatment on adsorption of SO₂ and extractability of the acid formed. *Carbon*, 35(10-11), 1639-1643.
- [32] Lizzio, A.A. and DeBarr, J.A. (1997). Mechanism of SO₂ removal by carbon. *Energy Fuels*, 11(2), 284-291.
- [33] Raymundo-Pinero, E., Cazorla-Amorós, D., Salinas-Martínez de Lecea, C., and Linares-Solano, A. (2000). Factors controlling the SO₂ removal by porous carbons: relevance of the SO₂ oxidation step. *Carbon*, 38(3), 335-344.
- [34] Zhang, P., Wanko, H., and Ulrich, J. (2007). Adsorption of SO₂ on activated carbon for low gas concentrations. *Chemical Engineering & Technology*, 30(5), 635-641.

- [35] Bielski, B.H., Cabelli, D.E., Arudi, R.L., and Ross, A.B. (1985). Reactivity of HO₂/O⁻₂ radicals in aqueous solution. *Journal of Physical and Chemical Reference Data*, 14(4), 1041-1100.
- [36] Buxton, G.V., Greenstock, C.L., Helman, W.P., and Ross, A.B. (1988). Critical review of rate constants for reactions of hydrated electrons, hydrogen atoms and hydroxyl radicals (·OH/·O⁻) in aqueous solution. *Journal of Physical and Chemical Reference Data*, 17(2), 513-886.

2.4 Hydrogen Refueling Support

Under previous funding, including prior APRISES awards, HNEI developed hydrogen infrastructure to produce, compress, store, and deliver the hydrogen to support a fleet of three hydrogen Fuel Cell Electric Buses (FCEB) operated by the County of Hawai‘i Mass Transit Agency (MTA). Under the current award, funding supported completing the commissioning of the hydrogen production, compression, and Hydrogen Transport Trailer (HTT) storage equipment located at the Natural Energy Laboratory Hawai‘i Authority (NELHA) in Kailua-Kona (Figure 2.4.1).



Figure 2.4.1. HNEI NELHA hydrogen station.



Figure 2.4.2. Central site production/distributed dispensing.

As illustrated in Figure 2.4.2, the overall hydrogen fueling concept is to deliver hydrogen from the hydrogen production facility in Kona to Hilo to support the operation of the two Fuel Cell Electric Buses (FCEBs) (Figure 2.4.3). The HTTs (Figure 2.4.4) filled with 105 kg of hydrogen at 450 bar, would be dropped off and used to fuel the buses. The empty HTT would be delivered back to the Kona site to be refilled.



Figure 2.4.3. MTA fuel cell electric bus.



Figure 2.4.4. Hydrogen transport trailers.

The HNEI hydrogen station is highly automated for unattended operation requiring a data acquisition and control system consisting of many sensors monitored by a PLC both on site and remotely by PowerTech in Canada. Commissioning this system required a considerable coordination effort to establish the software and hardware protocols, internet communications, and remote support from Powertech.

We originally planned on Powertech conducting a 10-day site visit to complete the final commissioning. Due to the COVID-19 pandemic, however, all travel with Canada was cancelled and we had to improvise. We worked with PowerTech to develop a commission plan and conduct the commissioning remotely and were able accomplish this due to HNEI's previous experience with the hydrogen station Powertech control system located at the Marine Corps Base Hawai'i. Walkthroughs and testing were performed remotely using laptop Zoom video links with excellent results.

Crash Bar Installation on Emergency Gates posed a challenge due the difficulty in contracting qualified personnel to do the work. With the help of NELHA, we were able to successfully complete the installation.

Designing, permitting, and installing the fire alarm system was a major effort. HNEI designed the system with the help of a fire protection engineer and a local architect firm. HNEI procured the equipment and obtained the necessary certifications to program the fire alarm monitoring equipment. After receiving a permit to install the system, HNEI engaged a certified fire alarm electrician to install the wiring and connect the sensors.

The majority of the electrical conduits at the facility run underneath a concrete slab including the fire alarm system conduits. The fire alarm code requirement is that all conduits carrying electrical wiring must be sealed and once sealed, it is permanent. Therefore, it is critical that all the circuits and sensors are working before the conduits are sealed. This required considerable time and effort

working with Powertech to validate their correct installation and operation. The fire alarm system successfully passed its inspection by the Fire Marshall on August 15, 2020.

A successful fire inspection then allowed us to operate the electrolyzer and commence producing hydrogen. The HTTs were shipped with the tanks purged with nitrogen. The HTTs were then purged with low pressure hydrogen to remove the nitrogen. In order to ensure that the hydrogen meets the SAE standards for fuel cells, there is a requirement to take samples and have them tested by an independent third-party test lab on the mainland as there are no laboratories in Hawai‘i. We therefore completed a Dangerous Goods Transport Certification course on August 28, 2020. This certification allows us to ship samples in accordance with the regulations.

The County of Hawai‘i Building and Permitting Department completed a successful final permit inspection on November 23, 2020 (Figure 2.4.5). The HNEI hydrogen station is the first hydrogen station permitted in the County of Hawai‘i and the second in Hawai‘i on non-federal land.

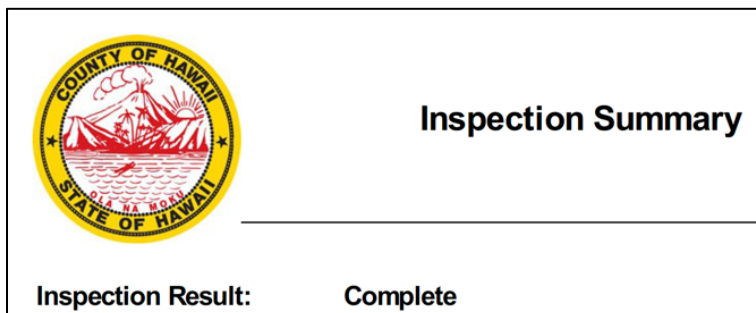


Figure 2.4.5. Permitting Inspection Certificate

Publications and Presentations

Peer-Reviewed Publications

1. Headley, A., Randolph, G., Virji, M., and Ewan, M. (2020). Valuation and cost reduction of behind-the-meter hydrogen production in Hawai‘i. *MRS Energy & Sustainability*, Vol. 7, E26.
2. Virji, M., Randolph, G., Ewan, M., and Rocheleau, R. (2020). Analyses of hydrogen energy system as a grid management tool for the Hawaiian Isles. *International Journal of Hydrogen Energy*, 45(15), 8052-8066.

Conference Proceedings and Presentations

1. Ewan, J.M. (2019). Hawai‘i: The State of Hydrogen. Fuel Cell Seminar, Long Beach, California, November 7, 2019.

Briefings

1. Ewan, J.M. (2019). HNEI Big Island Hydrogen Projects – HECO R&D. Hawaiian Electric Company Headquarters, O‘ahu, Hawai‘i, August 13, 2019.
2. Ewan, J.M. (2019). HNEI Big Island Hydrogen Projects – Stanford University Students, Briefing and Tour of NELHA Hydrogen Station. Natural Energy Laboratory Hawai‘i Authority, Kailua-Kona, Hawai‘i, September 16, 2019.
3. Ewan, J.M. (2019). HNEI Big Island Hydrogen Projects – Sandia National Laboratory, Briefing and Tour of NELHA Hydrogen Station. Natural Energy Laboratory Hawai‘i Authority, Kailua-Kona, Hawai‘i, December 4, 2019.
4. Ewan, J.M. (2019). HNEI Big Island Hydrogen Projects – University of Tasmania Center for Renewable Energy and Power Systems, Briefing and Tour of NELHA Hydrogen Station. Natural Energy Laboratory Hawai‘i Authority, Kailua-Kona, Hawai‘i, December 5, 2019.
5. Ewan, J.M. (2020). HNEI Big Island Hydrogen Projects – County of Hawai‘i R&D and Seadragon Inc, Briefing and Tour of NELHA Hydrogen Station. Natural Energy Laboratory Hawai‘i Authority, Kailua-Kona, Hawai‘i, January 16, 2020.
6. Ewan, J.M. (2020). HNEI Hydrogen Projects. Interview on the Solution News Podcast, January 17, 2020.

2.5 Printable Photovoltaics

The objective of this subtask is to develop novel thin film materials for low-cost photovoltaic applications using scalable “printing” processing. The task continues previous ONR-funded efforts to develop novel thin film materials (primarily Cu₂ZnSn(S,Se)₄: CZTSSe) for solar energy conversion using cheap and scalable liquid-based processing. With this approach, printable inks containing all the necessary components to form the solar absorber can be easily coated using high-throughput techniques, including spin coating and inkjet printing.

Under APRISES12 funding, HNEI developed a technology to form CZTSSe thin films using nano-crystalline “inks” made of CZTS (sulfide) nanoparticles with controlled composition, size and morphology. First, printable CZTS nano-crystalline inks were synthesized via so-called “hot injection technique.” With this technique, we have achieved mono-dispersed CZTS nanocrystals approximately 10 nm in diameter. Then, inks containing the CZTS nanocrystal “building blocks” were deposited onto conductive substrates (molybdenum coated glass) using spray pyrolysis techniques. Finally, CZTS-coated substrates were placed into a furnace with few milligrams of elemental selenium and heated at 500°C for 30 minutes. During this step, the selenium reacted with the CZTS nanoparticles to form large CZTSSe crystals. Eventually, the entire spray-deposited CZTS film was converted into a dense polycrystalline thin film materials, comparable to what one would achieve with conventional vacuum-based processes. Newly formed CZTSSe

materials were integrated as solar cells with short-circuit photocurrent density, open circuit voltage and efficiency were 19 mA/cm^2 , 375 mV and 2.3% , respectively. Although promising, this technique was not reproducible, as nanoparticles tend to agglomerate quickly after initial dispersion, making the printing step difficult.

Under APRISES15, the team explored several methods to physically separate particles and prevent agglomeration (Figure 2.5.1a). One technique consisted of decorating the particles surface with long-chain dodecanethiol (DDT) via so-called ligand exchange (Figure 2.5.1b). In this process, 5mL of CZTS nanocrystal ink was dispersed in isopropanol (15 mL). Then, 5 mL of DDT was added and the solution was finally sonicated with an ultrasonic horn at 20 kHz for 30 minutes. As a result of this treatment, particles were effectively dispersed, as evidenced in Figure 2.5.1c. However, the amount of DDT required for proper separation led to thin films with excessive amounts of organic residuals after the annealing process, leading to CZTSSe absorbers with poor optoelectronic properties.

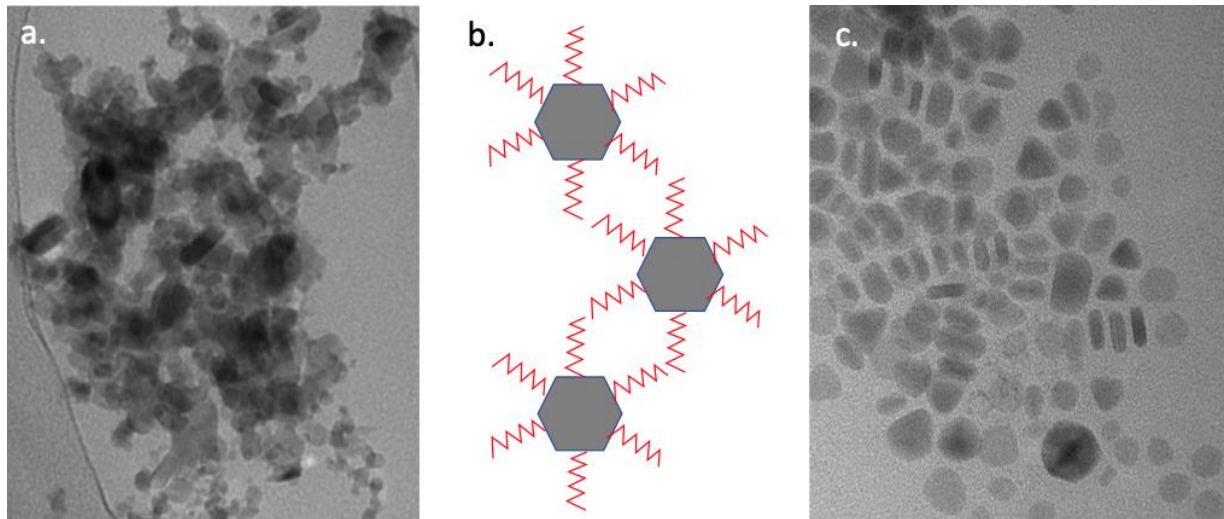


Figure 2.5.1. Transmission electron micrographs of CZTS nanoparticles (a) without and (c) with addition of dodecanethiol (DDT). (b) Schematic representing nanoparticles “coated” with long-chain DDT organic molecules physically separating them and preventing agglomeration.

After this setback, our team wanted to know if CZTS nanocrystal inks could be beneficial to other applications beyond photovoltaics. Under APRISES 15, we decided to evaluate if a CZTS particle could be transformed into a quantum dots (QD), a key structure for lighting technologies (LED), pharmacology (drug delivery) or chemical sensing. Here we used a cation exchange process (CEP) to incorporate zinc at particles surface, forming core/shell CZTSSe/ZnS QD nanostructures (Figure 2.5.2a). In a typical CEP, CZTS nanocrystal ink (5 mL) was dispersed in hexane (20 mL) containing zinc acetate (5 mmol). This mixture was then heated at 200°C for 60 minutes. Under such conditions, copper and tin in CZTS are replaced with zinc. The longer the CEP, the deeper Zn^{2+} diffuses into the QDs, and the smaller the QD cores become. Eventually, quantum

confinement occurs: energy states spread apart and the bandgap of QDs increases (Figure 2.5.2b). With this approach, the optical absorption and surface energetics of QDs can be tuned.

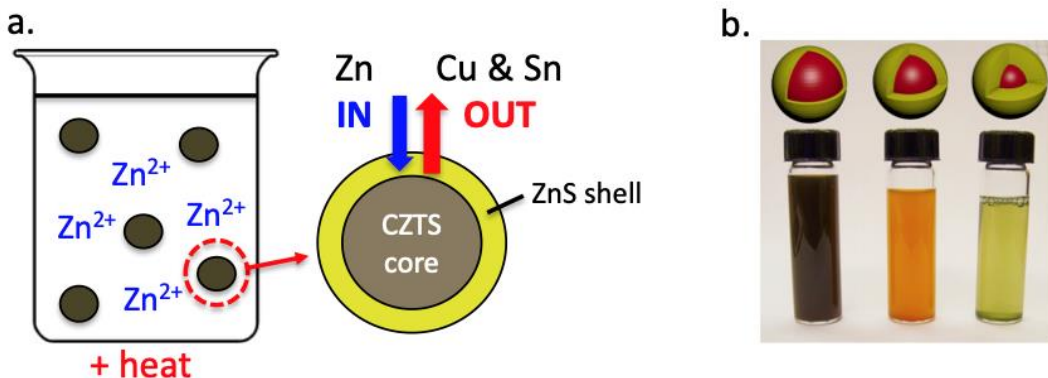


Figure 2.5.2. (a) Schematic of the cation exchange process used to create CZTSe-ZnS core-shell nanoparticles. (b) Pictures of inks containing CZTSe/ZnS core/shell particles obtained after different reaction time, highlighting the effect of quantum confinement (black: 10 minutes, orange: 30 minutes, and green: 50 minutes).

Based on our results obtained with nanoparticle-based (APRISES12 and APRISES15) and molecular inks (APRISES14), we concludes that the latter is by far the most promising approach for low-cost printable photovoltaic manufacturing. Molecular inks are far more stable, easier of processing and the resulting solar absorber have higher chemical purity and photoconversion efficiency compared to those fabricated with nanoparticle-based inks. Nonetheless, nanocrystal-based inks could be beneficial for applications where discrete particles (e.g. quantum dots) are required.

A second activity under this subtask focused on the development of room temperature processes for the preparation of transparent conductive oxides. In a standard solar cell integration, a thin transparent conductive oxide (TCO) top layer is required to transport the photogenerated charge carriers from the solar absorber to the top metallic grid. Degenerate n⁺-type indium tin oxide semiconductor exhibits excellent optical and electrical properties, making it an ideal candidate to be used as top TCO. However, the reported ITO films with excellent conductivity and high optical transmission are for deposition at elevated temperatures of 200°C or higher, which can cause solar cell degradation. Thus, a room temperature ITO deposition was investigated during APRISES15. The ITO films were deposited by a radio frequency magnetron sputtering system onto a soda lime glass (1 in x 1 in) at room temperature with different O₂ fluxes. Sputtering was conducted using an ITO target with 10 wt% SnO₂ and 90 wt% In₂O₃, fixed at a distance of 11 in between the target and the substrate. Prior to the deposition, the sputtering chamber was pumped down overnight to a base pressure of approximately 0.2×10^{-6} Torr. Ar flow of 20 standard cubic centimeter per minute (scfm) and an O₂ flow in the range of 0.14-0.25 scfm was introduced prior to sputtering and pre-sputtered for 10 minutes at 20W power. The deposition rate was approximately 0.5 nm/s, resulting in a sputtering time of approximately 30 minutes for an ITO layer of 100 nm thickness.

The resistances of the ITO layer was measured using a four-point probe and the thickness using a profilometer. Thus far, the best room temperature ITO deposition exhibited ~80% transmittance from 300-2000nm range (Figure 2.5.3, compared to 905 for standard ITO@200°C) as well as a sheet resistance as low as 92 Ω/square (compared to 50 Ω/square for standard ITO@200°C) at an O₂ flowrate of 0.2 sccm. Continued investigations includes the change of room temperature ITO layer properties with varying RF power, film thickness and O₂ flowrate.

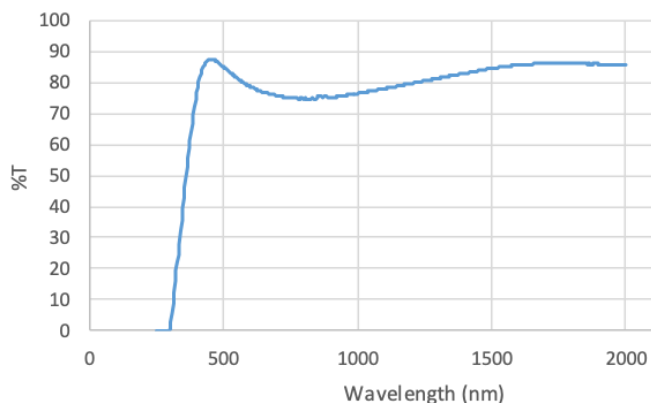


Figure 2.5.3. Transmission vs. wavelength measured on a 100 nm thick ITO layer deposited at room temperature.

TASK 3: BIOFUELS

Task 3 continued research supporting the development of technologies for the production and use of synthetic fuels. Under Subtask 3.1, a thermochemical pretreatment of pongamia seeds to improve subsequent torrefaction was explored. Under Subtask 3.2, labscale work on novel methods to enhance anaerobic digestion efforts were completed and efforts to identify commercial partners were undertaken. Efforts to develop new technology to produce high-grade liquid fuels from syngas (H₂, CO, and CO₂) were continued under Subtask 3.3. Under Subtask 3.4, the storage and oxidation stabilities of DSH-76, CHCD-76, and their blends with F-76 were investigated. Additional detail for each of these subtasks follows.

3.1 Bioenergy Systems

Torrefaction can be used to reduce the oxygen content of biomass and improve the feedstock properties for thermochemical conversion. Pongamia (*Millettia pinnata*), a leguminous, oil-seed bearing tree, is a potential resource for sustainable aviation fuel production due to the high oil content of its seeds. The present work investigates thermochemical pretreatment of pongamia

processing residues, i.e. pods. Torrefaction tests were performed with both a fixed bed reactor and a macro thermogravimetric analyzer (TGA) under nitrogen atmospheres. The effects of process conditions on feedstock properties relevant to thermochemical conversion technologies, proximate and ultimate composition, heating value, and Hardgrove grindability index (HGI), were measured. The chemical structure, reactivity, and changes in elemental composition of the torrefied materials were also investigated. The mass and energy yields decreased 43% and 25%, respectively, from the mildest (165°C) to the most severe (281°C) torrefaction conditions, while the energy densification index increased from 1.15 to 1.68. The HGIs of pods torrefied at temperatures >215°C were found to equal or exceed the HGI of a reference bituminous coal sample. A LECO model TGA801 macro-TGA with a sample loading capacity of ~95 g was also used to torrefy pongamia pods. Products from the LECO and the fixed bed reactor were comparable, and the macro-TGA was demonstrated to be a useful fast screening tool to study effects of process parameters. Complete details can be found in the publication listed below.

Publications and Presentations

Peer-Reviewed Publications

1. Fu, J., Summers, S., Turn, S.Q., and Kusch, W. (2021). Upgraded pongamia pod via torrefaction for the production of bioenergy. Fuel. 291, 120260.

Conference Proceedings and Presentations

1. Fu, J., Summers, S., and Turn, S.Q. (2020). Torrefied pongamia pod: A coproduct of sustainable aviation fuel. Thermal & Catalytic Sciences Symposium, Held virtually and in Kennewick, Washington, October 5-7, 2020.

3.2 High-Rate Anaerobic Digestion

Under this subtask, the lab-scale evaluation of deacylated chitosan-biochar biofilm support material was completed. The results of this analysis were used to initiate design of a mature manufacturing protocol and in support of efforts to conduct demonstration-scale evaluation targeting septic waste and using the reactor system in place at the East Honolulu wastewater treatment facility.

Efforts were made to collaborate and license on scale up use of the reactors. Negotiations were conducted with Real Green Power, but we were not able to reach agreement on both accounts over intellectual property issues. In an effort to support future licensing potential, efforts continued that included developing cost models for reactors based on biochar supports. Specifically, a master

design was developed, inclusive of PID diagrams, costing, manufacturing, and shipping to build and install a wastewater treatment system designed from past research and commercial demonstration projects. PID diagrams were also constructed that considered targeted organic loading rates and hydraulic retention times. These designs accounted for modular fabrication of reactor units, dimensions of reactors and pipes, piping size, recycle lines, details of how to install and connect modules, utilities and electrical, materials of construction, sources of manufacturing, packing materials, shipping and installation issues, among others.

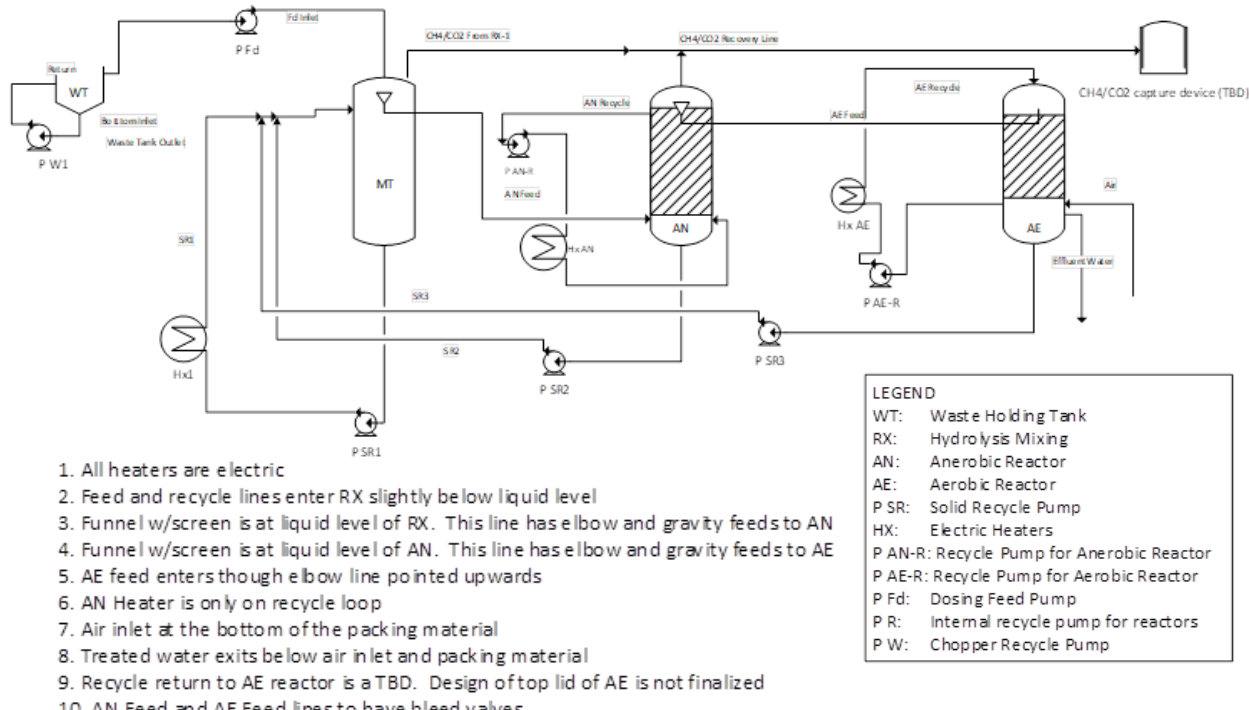


Figure 3.2.1. PID diagram of an anaerobic-aerobic digestion reactor system.

Finally, cost estimates for fabrication, shipping, and installation were estimated and three-dimensional renderings were generated.

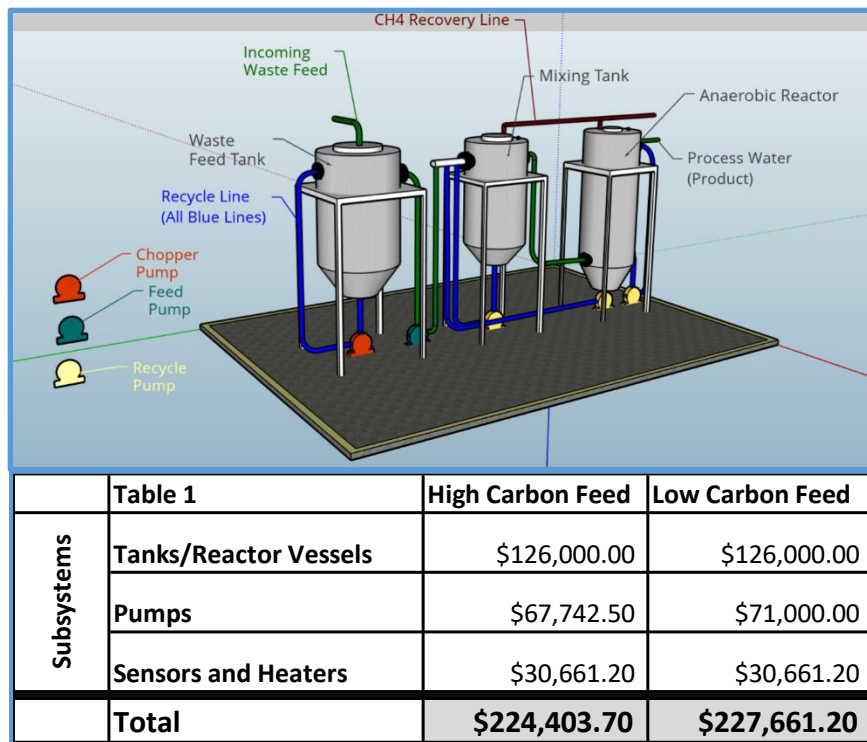


Figure 3.2.2. Rendering and cost estimates for a reactor system.

The sum total of detailed method and results that support this design are published in the journal articles listed below.

Publications and Presentations

Peer-Reviewed Publications

- Lin, S., Rong, K., Lamichhane, K.M., Babcock, R.W., Kirs, M., and Cooney, M.J. (2020). Anaerobic-Aerobic Biofilm-Based Digestion of Chemical Contaminants of Emerging Concern (CEC) and Pathogen Indicator Organisms in Synthetic Wastewater. *Bioresource Technology*, 299, 122554.
- Cooney, M.J., Lamichhane, K., and Rong, K. (2019). Cross comparative analysis of liquid phase anaerobic digesters. *Journal of Water Process Engineering*, 29, 100765.
- Lamichhane, K.M., Lewis, K., Rong, K., Babcock Jr., R.W., and Cooney, M.J. (2017). Treatment of high strength acidic wastewater using passive pH control. *Journal of Water Process Engineering*, 18, 198-201.
- Lamichhane, K., Furukawa, D., and Cooney, M.J. (2017). Co-digestion of glycerol with municipal wastewater. *Journal of Chemical Engineering & Process Techniques*, 3(1), 1034.
- Cooney, M. J., Lewis, K., Harris, K., Zhang, Q., and Yan, T. (2016). Start up performance of biochar packed bed anaerobic digesters. *Journal of Water Process Engineering*, 9, e7-e13.

6. Postacchini, L., Lamichhane, K.M., Furukawa, D., Babcock, R.W., Ciarapica F.E., and Cooney, M.J. (2016). Life Cycle Analysis of three methods to treat primary clarifier effluent. *Water Science and Technology*, 73(10), 2353-2360.
7. He, X., Zhang, Q., Cooney, M.J., and Yan, T. (2015). Biodegradation of Fat, Oil and Grease (FOG) Deposits under Various Redox Conditions Relevant to Sewer Environment. *Applied Microbiology and Biotechnology*, 99(14), 6059-6068.
8. Lopez, R., Higgins, S., Pagaling, E., Yan, T., and Cooney, M.J. (2014). High rate anaerobic digestion of wastewater separated from grease trap waste. *Renewable Energy*, 62, 234-242.

3.3 Liquid Fuels from Syngas

This subtask aimed at a new technology to produce high-grade liquid fuels from syngas (H_2 , CO , and CO_2). The technology consisted of: (1) formation of polyhydroxybutyrate (PHB) from the gas substrates by using a chemoautotrophic microorganism and (2) conversion of the PHB into hydrocarbon oil. In previous work, a gasoline-grade liquid fuel was made from PHB through a one-pot catalytic refining. It was also found that PHB formation from the gas was the process bottleneck due to the low solubility of the gas molecules in an aqueous mineral solution. In this work, we examined the liquid-side gas mass transfer resistance and evaluated the gas mass transfer in a packed bed bioreactor. The research revealed the effects of different packing materials, the liquid velocity and distributor on the volumetric mass transfer coefficients (k_{LA}) of oxygen and hydrogen. We also investigated the nutrient control strategy for PHB formation from the gas substrates and the enhancement of gas fermentation under a raised operation pressure. The details have been reported in three peer-reviewed papers listed at the end of this section and the major results and discoveries are summarized as follows.

Liquid-Side Gas Mass Transfer Resistance

In a quiescent gas-liquid bioreactor, the gas consumption depended on the molecular diffusion of the gas substrates from the gas phase to the microbial cells in the aqueous solution. According to the two-film mass transfer theory [1], the liquid side mass transfer resistance plays a predominant role in the absorption of poorly soluble gases such as H_2 , O_2 and CO_2 . Our research provided the experimental evidence. Table 3.3.1 compares the gas uptake rates by the microbes that were suspended in an aqueous solution or kept on a solid agar surface of the same solution. The cells in the liquid solution relied on the molecular diffusion in both gas and liquid phases, while the cells on the agar surface relied primarily on the molecular diffusion in the gas phase.

Table 3.3.1. Gas uptake rates by microbial cells suspended in liquid solution versus on solid surface.

Microbial growth under a gas phase	In Liquid Solution ^a	On Solid Surface ^b	
Gas mass transfer distance in liquid (mm)	4.4	1	1
Gas-liquid contact area (cm ²)	57	57	114
Maximum gas uptake rate (mmol h ⁻¹) ^c	0.55	1.1	2.2
Specific maximum gas uptake rate (mmol m ⁻² h ⁻¹)	96	193	190

- a. Microbes were suspended in the mineral solution.
- b. Microbes were kept on the agar surface of the mineral solution.
- c. The maximum gas consumption rate during a batch culture.

In the liquid solution, the distance of molecular diffusion was up to 4.4 mm and the maximum gas consumption rate per gas-liquid contact area was 96 mmol m⁻² h⁻¹. With the molecular diffusion distance being reduced to 1 mm on the agar solid surface, the gas uptake rate was doubled, reaching 193 mmol m⁻² h⁻¹. This significant rate difference is the evidence of the liquid-side mass transfer resistance. With the gas-liquid contact area being doubled, the overall gas uptake rate on the same agar solid surface was also doubled to 2.2 mmol h⁻¹ from 1.1 mmol h⁻¹ while the specific rate per surface area was kept at the same level (~190 mmol m⁻² h⁻¹). The results revealed two important engineering factors that can enhance the gas mass transfer in a bioreactor by: (a) keeping a thin liquid film to reduce the liquid-side mass transfer resistance and (b) increasing the gas-liquid contact area per reactor volume.

The surface area per volume of a packed bed bioreactor depends on the packing materials. In this work, the *volumetric oxygen mass transfer coefficient* in packed beds of five packing materials were evaluated, including three random packings of glass Raschig ring, ceramic Berl saddles and protruded stainless steel (PSS), and two structured packings of Styrofoam pad and aluminum mesh pad (Table 3.3.2). Their geometry, surface area, wettability, and bed structure were quite different, giving different effective interfacial areas (A_e) of gas-liquid contact.

Table 3.3.2. The characteristics of packing materials in packed bed bioreactors.

Pack type	Random				Structured	
Bed type	Raschig ring	Berl saddle ^a	Berl saddle ^b	PSS mesh ^c	Foam pad	Mesh pad
Material	Glass	Ceramic	Ceramic	SS	Styrofoam	Aluminum
Size (cm)	Ø0.5	Ø0.6	Ø0.8	Ø0.6	Ø6 x 22	Ø6 x 22
Shape	Cylinder	Saddle	Saddle	Cylinder	Roll	Roll
Volumetric surface area (m ² m ⁻³)	710	1150	750	1222	338	1015
Void space (%)	60	60	44	96	53	60

- a. Small Berl saddles used in a small column (6 cm in diameter).
- b. Large Berl saddles used in a large column (20 cm in diameter) for geometry comparison (see Table 3.3.3).
- c. Protruded stainless steel mesh.

In a quasi-quiescent gas phase at a low gassing rate, the liquid flew downward through the packed beds and the velocity was a major operational parameter that affected the gas-liquid contact and gas mass transfer. Figure 3.3.1 shows the effect of liquid velocity on the volumetric oxygen mass transfer coefficient $(k_{LA})_{O_2}$ in the random packed beds and the structured beds. In the random packed beds, the value of $(k_{LA})_{O_2}$ increased almost linearly with the liquid velocity up to 17 m h^{-1} , above which it behaved differently depending the packing materials. It either approached a plateau in the bed of PSS or dropped in the beds of ceramic saddles and glass rings at the high liquid velocities (22 m h^{-1} or above). In the structured beds, however, the value of $(k_{LA})_{O_2}$ increased almost linearly with the liquid velocity up to 26 m h^{-1} . This was attributed to a phenomenon of bed flooding at the high liquid flow rates. In a flooded bed, the packing materials were immersed in the liquid while the gas bubbles moved slowly though the bed. As a result, the gas-liquid contact occurred primarily at the interfacial area of gas bubbles, not on the surface of packing materials. The bed of PSS had a large void space (96%) for high liquid flow rates as well as a high specific interfacial surface area ($1222 \text{ m}^2 \text{ m}^{-3}$) for excellent gas-liquid contact. The highest $(k_{LA})_{O_2}$ in PSS bed was 240 h^{-1} at a liquid velocity of 25.7 m h^{-1} , which was about 41% higher than that of saddle bed, the second high-performance bed with a $(k_{LA})_O$ of 170 h^{-1} at a liquid velocity of 22 m h^{-1} . Other packed beds exhibited a moderate $(k_{LA})_{O_2}$ ($<160 \text{ h}^{-1}$) under the experimental conditions, which was in the range of industrial gas scrubbers [2]. The results indicate that the materials of the packed beds had a little effect on the gas mass transfer rate.

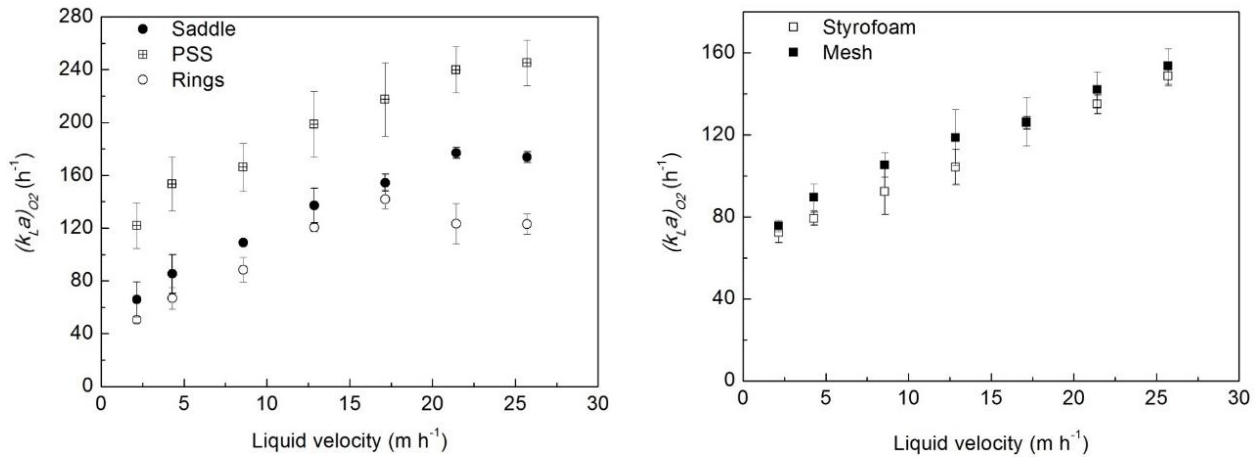


Figure 3.3.1. Effect of liquid velocity on O_2 mass transfer coefficient $(k_{LA})_{O_2}$ in different packed beds: (Left) random packings of protruded stainless steel (PSS), small Berl saddles and Raschig rings, and (Right) structured packings of Styrofoam pad and aluminum mesh.

The oxygen uptake rate (OUR) of the microbes can also enhance the overall gas mass transfer in the liquid solution. Figure 3.3.2 shows the time courses of the OUR and the dry cell mass (DCM) concentration in the PSS bed at two liquid velocities. The high velocity (53 m h^{-1}) raised both OUR and cell density during the culture. With cell density increase, the OUR increased to a maximum level and then declined. It implies that the OUR depended on the rates of two sequential events: the O_2 mass transfer followed by microbial consumption. In the early time (0-8 hours), the

OUR was determined by the low cell density and microbial consumption rate. When the microbes entered the exponential growth phase, both cell density and OUR increased and the dissolved oxygen concentration (DO_2) declined quickly. When the DO_2 concentration dropped to zero, a maximum OUR (OUR_{\max}) was observed, which was determined by the maximum O_2 mass transfer rate of the packed bed bioreactor and expressed with Eq. 3.3.1.

$$\text{OUR}_{\max} = (k_L a)_{O_2} \left(\frac{P_{O_2}}{H_{O_2}} \right) \quad (\text{Eq. 3.3.1})$$

Where P_{O_2} and H_{O_2} are the partial pressure and the Henry's constant of oxygen gas. After the peak level of OUR, the obligate aerobic strain was exposed to near zero DO_2 , below the critical O_2 level. The microbial activity deteriorated even though the cell density was increasing. The OUR declined gradually to approximately 70 % of the peak value. This phenomenon should be considered when the value of $(k_L a)_{O_2}$ is determined by measuring the OUR. Ideally, the OUR_{\max} should be measured to determine the real $(k_L a)_{O_2}$ value of a bioreactor under the operation conditions.

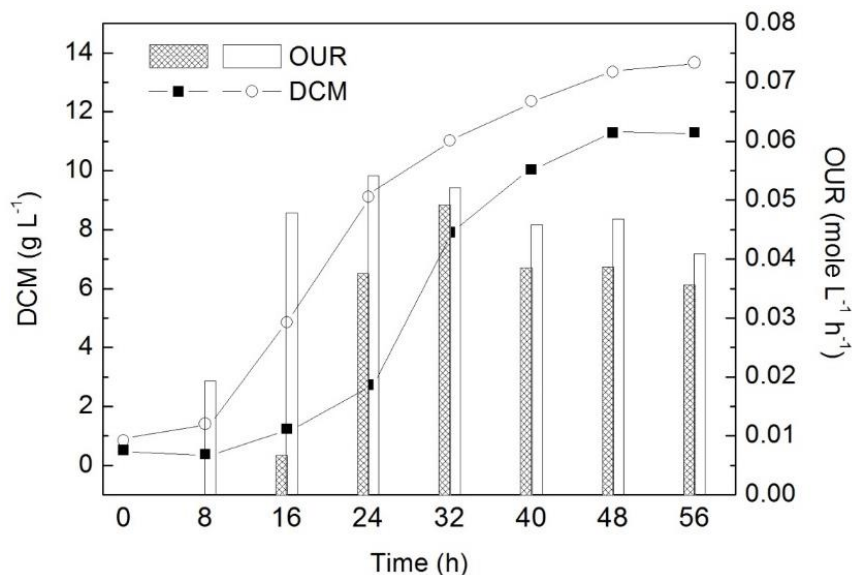


Figure 3.3.2. The time courses of dry cell mass (DCM) concentration and O_2 uptake rate (OUR) at liquid velocity of 26 m h^{-1} (filled) and 53 m h^{-1} (blank).

Hydrogen

Methods similar to that for determining the OUR were also used to determine the *maximum hydrogen uptake rate (HUR_{\max})*. In the same bioreactor under the same operation conditions, the values of $(k_L a)_{O_2}$ and $(k_L a)_{H_2}$ were 357 h^{-1} and 525 h^{-1} , respectively. The ratio of $(k_L a)_{H_2}$ to $(k_L a)_{O_2}$ was 1.47. According to the surface renewal model [3], the liquid-side mass transfer coefficient (k_L) of poorly soluble gas is proportional to the square root of its molecular diffusion coefficient (D_L). The diffusion coefficients of H_2 (D_{LH_2}) and O_2 (D_{LO_2}) in water at 30°C are 5.11×10^{-5} and

$2.42 \times 10^{-5} \text{ cm}^2 \text{ s}^{-1}$, respectively [4]. The ratio of the mass transfer coefficients of H₂ to O₂ is equal to the square root of their molecular diffusion coefficients ratio (Eq. 3.3.2) [5].

$$\frac{(k_{La})_{H_2}}{(k_{La})_{O_2}} = \left(\frac{D_{LH_2}}{D_{LO_2}}\right)^{1/2} = \left(\frac{5.11}{2.42}\right)^{1/2} = 1.45 \quad (\text{Eq. 3.3.2})$$

Our research indicates that the surface renewal model is suitable for the gas mass transfer in the packed bed bioreactor. Therefore, the mass transfer coefficient of other insoluble gases such as CO₂ can be conveniently calculated from their molecular diffusion coefficients.

In addition to the packing materials, the *bed geometry and liquid distributor* were also evaluated. At the constant low gassing rate and liquid velocity of 25 m h⁻¹, two packed beds of ceramic Berl saddles (see Table 3.3.1) and two types of liquid distributers were evaluated and compared with the blank columns as shown in Table 3.3.3. The bed of small saddles (Φ 0.6 cm) had a $(k_{La})_{O_2}$ of 180 h⁻¹, which was 52% higher than that of the blank column with the same shower liquid distributer. The final cell density was 9.5 g L⁻¹, almost doubled in comparison with the blank column. To evaluate a nozzle liquid distributor, a large column (Φ 20 cm) was packed with large saddles (Φ 0.8 cm) with a bed height of 4 cm and 8 cm, respectively. The nozzle (90° full cone) was an excellent liquid distributor that spread tiny liquid droplets into the gas phase. In the blank column, the $(k_{La})_{O_2}$ was 256 h⁻¹ and the cell density 14.0 g L⁻¹, much higher than those with a shower liquid distributor. With the shallow packed beds, the $(k_{La})_{O_2}$ was increased by 19% to 57%, while the cell density 11% to 25%. The liquid distributer exhibited a great effect on the gas mass transfer rat as shown by two blank columns. The nozzle liquid distributor increased the value of $(k_{La})_{O_2}$ by 217%. The packing materials could further increase the gas mass transfer rate by up to 50%, regardless of the bed volume and geometry.

Table 3.3.3. Overall performance of gas fermentation in the packed bed bioreactors.

Distributer	Shower ^a	Shower ^a	Nozzle ^b	Nozzle ^b	Nozzle ^b
Column size (cm x cm)	Ø6 x 20	Ø6 x 20	Ø20 x 20	Ø20 x 20	Ø20 x 20
Bed volume (L)	0	0.65	0	1.3	2.6
Bed height (cm)	0	23	0	4	8
Saddle size (cm)	-	0.6	-	0.8	0.8
Distributer pressure drop (psi) ^c	5	5	13.5	13.5	13.5
$(k_{La})_{O_2}$ (h ⁻¹) ^d	118	180	256	305	402
Cell growth rate μ_{max} (h ⁻¹) ^e	0.1	0.12	0.12	0.20	0.21
Maximum cell density (g L ⁻¹)	5.0	9.5	14.0	15.6	17.5

- a. A shower liquid distributer with 20 holes (1mm hole diameter).
- b. A 90° full cone spray nozzle with an orifice diameter of 1.65 mm.
- c. The pressure drop through the distributers at a liquid flow rate of 1.2 L min⁻¹.
- d. The oxygen mass transfer coefficient measured at the maximum oxygen uptake rate.
- e. The maximum specific cell growth rate in a batch operation.

The substantial improvement of $(k_{La})_{O_2}$ with nozzle liquid distributor was attributed to the tiny liquid droplets, which dramatically reduced the liquid-side mass transfer resistance as indicated above. In comparing with the shower distributor, the nozzle spray required some pump energy against a pressure drop of 13.5 psi across the nozzle. Due to an even distribution of the liquid droplets by the nozzle, the saddles (1.3 L and 2.6 L) could be packed in flat shallow beds. The $(k_{La})_{O_2}$ were increased to 305 h⁻¹ and 402 h⁻¹, or 11% to 57% because of the packed beds. This improvement could also be achieved in a deep bed (23 cm) with a shower distributor. With the nozzle spray and packed beds, the maximum specific growth rates (μ_{max}) of the microbes reached as high as 0.21 h⁻¹, similar to the heterotrophic growth on glucose and glycerol [6,7]. This fact indicates that the gas can be effectively utilized under the conditions of high gas mass transfer rate.

According to a previous study, PHB formation from organic carbon source such as glycerol can be intensified by *limiting the nutrients* such as ammonium nitrogen [7]. It was not clear if the same control strategy could be applied to the autotrophic growth on CO₂. A two-phase gas fermentation was conducted in this work, consisting of an initial cell growth phase with a nitrogen concentration of 0.25 g L⁻¹ NH₃-N, followed by a PHB formation phase under nitrogen limitation. Figure 3.3.3 shows that the microbes grew exponentially at a maximum specific rate μ_{max} of 0.18 h⁻¹ after a lag phase (about 8 hours). With a rapid increase in DCM concentration from approximately 0.7 to 4.0 g L⁻¹, the concentration of NH₃-N dropped to zero, which triggered a significant increase of PHB content from about 10 wt% to 42 wt%. As the PHB content further increased to 67 wt% the DCM concentration slowly increased to 5.0 g L⁻¹. Meanwhile the residual cell mass (RCM) declined from the maximum level of 2.7 g L⁻¹ to 1.7 g L⁻¹, and then maintained at a constant level of 1.7 to 1.8 g L⁻¹ thereafter.

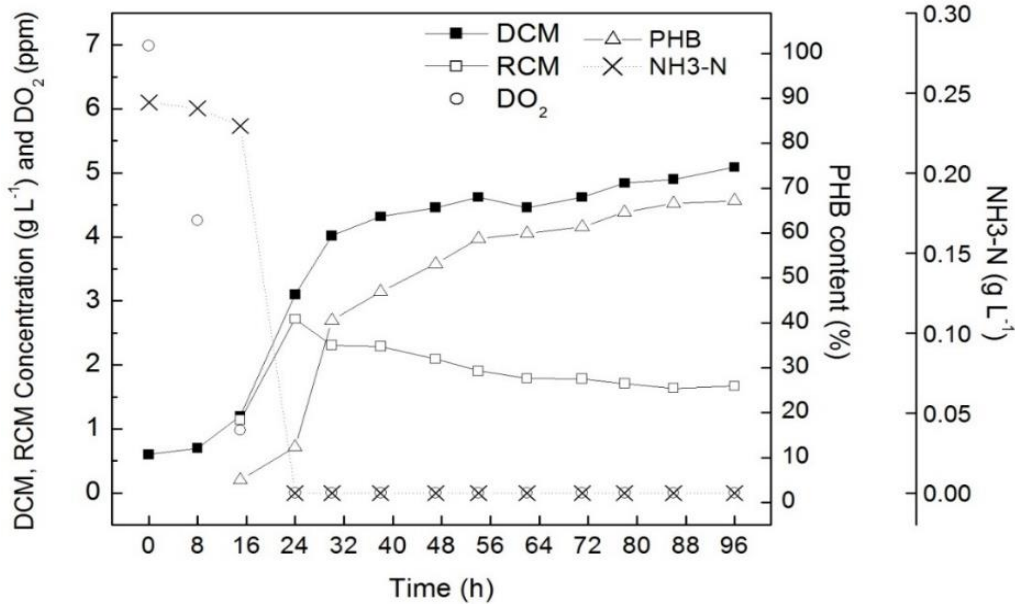


Figure 3.3.3. Time courses of the concentrations of dry cell mass (DCM), residual cell mass (RCM), dissolved O₂ (DO₂) and ammonium nitrogen (NH₃-N).

With the PHB content being significantly increased following the nitrogen limitation, the DO₂ concentration also dropped to zero. It raised a question whether or not nitrogen limitation was the true or only factor for PHB formation. In a separate gas fermentation (data not shown here), the ammonia-nitrogen was maintained at 0.25 g L⁻¹ or above to provide sufficient nitrogen nutrient. When the cell density reached 8 g L⁻¹ or so in 24 hours, the dissolved oxygen concentration dropped to zero and then maintained at near zero for 32 hours. During that period of time, little PHB was formed. Similar phenomenon was also observed with hydrogen limitation under sufficient nitrogen nutrient. The results revealed that the PHB formation was triggered by nitrogen limitation. Neither oxygen nor hydrogen limitation could trigger the PHB formation. Previous studies reported that O₂ limitation alone could trigger PHB accumulation [8], but it was not observed in this work. It is concluded that the nutrient control strategy for PHB formation on organic carbons can also be applied to the autotrophic culture on CO₂.

In addition to the volumetric mass transfer coefficient k_{LA} , the *gas partial pressure* or bioreactor's operation pressure may also affect the gas uptake rate (Eq. 3.3.1). Figure 3.3.4 shows the overall gas uptake rate per liter of mineral solution under two operation pressures. The gas uptake rate is expressed as the standard cubic centimeters per min (sccm) under the standard conditions (273°K, 1 atm). One sccm is equal to 0.0446 mmole gas min⁻¹.

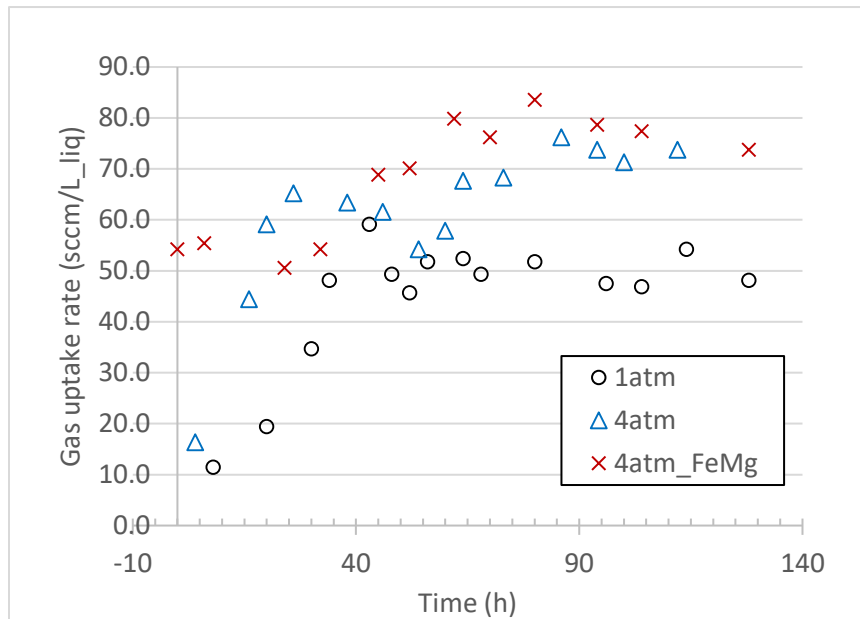


Figure 3.3.4. Overall gas uptake rates under total gas pressures of 1atm or 4 atm. The amounts of minerals (Fe and Mg) were doubled in one fermentation (4atm_FeMg).

Under an ambient pressure (1 atm), the gas uptake rate increased with time (cell density), and reached a plateau around 50 sccm L⁻¹. About 54 vol% of the inlet gas was absorbed and utilized in the bioreactor. Under a high pressure (4 atm), the gas uptake rate increased with time much faster, approaching a higher plateau around 70 sccm L⁻¹. About 75 vol% of the inlet gas was

absorbed and utilized in the bioreactor. With an inoculum of very high cell density, the gas uptake rate under 4 atm reached ca. 55 sccm L⁻¹ at the beginning and increased to a plateau ca. 80 sccm L⁻¹. About 86 vol% of the inlet gas was absorbed and utilized in the bioreactor.

Obviously, a high operation pressure of the bioreactor could enhance the gas fermentation by increasing the driving force of gas mass transfer (Eq. 3.3.1). The enhancement, however, was not linearly proportional to the pressure increase as predicted by the Henry's law. This might be attributed to the limitation of one gas substrate. Two growth stages and rates were observed during the gas fermentation, which was characterized by a critical cell density (X_{cr}). As shown in Table 3.3.4, under the ambient pressure (Run A), the critical cell density was 4.5 g L⁻¹, above which the specific growth rate dropped from 0.062 h⁻¹ to 0.011 h⁻¹. Under the high pressure (Run B), the critical cell density reached 6.3 g L⁻¹, above which the specific growth rate declined from 0.12 h⁻¹ to 0.01 h⁻¹. With a very high initial cell density (Run C), the growth was almost immediately under gas limitation. As a result, no fast growth stage was observed and the cell density increased linearly with time from 11.7 g L⁻¹ at the beginning to 28.5 g L⁻¹.

Table 3.3.4. Effect of gas pressure on cell growth rate.

Run	Pressure ^a (atm)	FeMg ^b	X_0 ^c (g L ⁻¹)	X_{cr} ^d (g L ⁻¹)	X_{max} ^e (g L ⁻¹)	Fast growth		Slow growth	
						μ (h ⁻¹) ^f	R ²	μ (h ⁻¹) ^f	R ²
A	1	1	0.5	4.5	15	0.062	0.977	0.011	0.981
B	4	1	0.45	6.3	17.5	0.12	0.976	0.010	0.954
C	4	2	11.7	None	28.5	-	-	0.0074	0.969

- a. The absolute gas pressure in bioreactor.
- b. Concentrations of Fe and Mg: (1) ferric ammonium citrate 0.1 g L⁻¹, MgSO₄·7H₂O 0.5 g L⁻¹, and (2) ferric ammonium citrate 0.2 g L⁻¹ and MgSO₄·7H₂O 1 g L⁻¹.
- c. The initial cell density or inoculum.
- d. A critical cell density for a high growth stage.
- e. The maximum cell density or dry cell mass concentration.
- f. The specific growth rates. R² value is a statistical measure of data regression closeness.

Publications and Presentations

Peer-Reviewed Publications

1. Yu, J. and Lu, Y. (2019). Carbon dioxide fixation by a hydrogen-oxidizing bacterium: biomass yield, reversal respiratory quotient, stoichiometric equations and bioenergetics. Biochemical Engineering Journal, 152, 107369.
2. Yu, J. and Munasinghe, P. (2018). Gas Fermentation Enhancement for Chemolithotrophic Growth of Cupriavidus necator on Carbon Dioxide. Fermentation, 4(3), 63.
3. Lu, Y. and Yu, J. (2017). Gas mass transfer with microbial CO₂ fixation and poly(3-hydroxybutyrate) synthesis in a packed bed bioreactor. Biochemical Engineering Journal, 122, 13-21.

Conference Proceedings and Presentations

1. Yu, J. (2019). Drop-in transportation fuels from renewable hydrogen and carbon dioxide. World Hydrogen Technologies Convention, Tokyo, Japan, June 2-7, 2019.
2. Yu, J. (2018). A green plastic and drop-in transportation fuels from carbon dioxide and renewable energy. TechConnect World Innovation Conference, Anaheim, California, May 13-16, 2018.
3. Yu, J. (2017). Bioplastics and drop-in transportation fuels from carbon dioxide and solar hydrogen. Environmental and Energy Resource Management Summit, Washington, D.C., November 9-11, 2017.

References

- [1] Whitman, W.G. (1962). The two-film theory of gas absorption. International Journal of Heat & Mass Transfer, 5, 429-433.
- [2] Treybal, R.E. (1980). Mass-transfer operations, New York.
- [3] Asher, W.E. and Pankow, J.F. (1991). Prediction of gas/water mass transport coefficients by a surface renewal model, Environmental Science & Technology, 25, 1294-1300.
- [4] Speight, J.G. (2005). Lange's handbook of chemistry, McGraw-Hill New York.
- [5] Gianetto, A. and Specchia, V. (1992). Trickle-bed reactors: state of art and perspectives. Chemical Engineering Science, 47, 3197-3213.
- [6] Jaremko, M. and Yu, J. (2011). The initial metabolic conversion of levulinic acid in Cupriavidus necator. Journal of biotechnology, 155, 293-298.
- [7] Tanadchangsaeng, N. and Yu, J. (2012). Microbial synthesis of polyhydroxybutyrate from glycerol: gluconeogenesis, molecular weight and material properties of biopolyester. Biotechnology and bioengineering, 109, 2808-2818.
- [8] Tanaka, K., Ishizaki, A., Kanamaru, T., and Kawano, T. (1995). Production of poly (D-3-hydroxybutyrate) from CO₂, H₂, and O₂ by high cell density autotrophic cultivation of Alcaligenes eutrophus, Biotechnology and bioengineering, 45, 268-275.

3.4 Marine Fuels

Catalytic hydrothermal conversion diesel (CHCD-76), synthesized isoparaffin (SIP-76), and hydroprocessed renewable diesel (HRD-76) have been produced in sufficient quantity and supplied to the U.S. Navy for blending with traditional marine diesel NATO F-76. The present work investigates the storage and oxidation stabilities of DSH-76, CHCD-76, and their blends with F-76. Chemical composition and physicochemical properties of these two biofuels, including viscosity, density, peroxide value, heat of combustion, acid number, and phase behavior, were determined using required ASTM methods. ASTM D4625 and D5304 methods were employed

to investigate the long-term storage stability of these two biofuels and theirs blends with F-76. ASTM D5304 method was also modified to investigate the oxidation process of these fuel samples. In addition, ASTM D2274 tests were conducted to investigate oxidation stability of the neat and blended fuel samples. The influence of long-term storage and oxidation on fuel physicochemical properties was investigated based on ASTM methods. SIP-76 and CHCD-76 were found have superior storage and oxidation stability in comparison with petroleum F-76. This is also the first report on storage and oxidation stability of SIP-76 and CHCD-76. Complete details can be found in the publication listed below.

Publications and Presentations

Peer-Reviewed Publications

1. Fu, J. and Turn, S.Q. (2019). Characteristics and stability of biofuels used as drop-in replacement for NATO marine diesel. Fuel, 236, 516-524.

Conference Proceedings and Presentations

1. Fu, J. and Turn, S.Q. (2016). Long-term storage and oxidation stabilities of second generation biofuels used as drop-in replacement for marine diesel. 254th American Chemical Society National Meeting & Exposition, Washington, DC, August 22, 2016.

TASK 4: METHANE HYDRATES

The APRICES15 Methane Hydrates activities comprised three areas of focus: 1) hydrate energy, 2) environmental impacts of methane release from hydrates, and 3) international collaborative R&D.

National R&D programs on methane hydrates were initiated in Japan and India in the mid-1990's with the goal of commercial gas production within a 20-year time horizon [1]. The U.S. established its own program in May 2000. The Methane Hydrate Research and Development Act of 2000 (Public Law 106-193) included seven technical areas of focus: 1) identification, exploration, assessment, and development of methane hydrate as a source of energy; 2) technology development for efficient and environmentally sound recovery of methane from hydrates; 3) transport and storage of methane produced from methane hydrates; 4) education and training related to methane hydrate resource R&D; 5) assessment and mitigation of environmental impacts of natural and purposeful hydrate degassing; 6) development of technologies to reduce the risks of drilling through methane hydrates; and 7) support of exploratory drilling projects.

The objectives of the Methane Hydrates task of the APRISES initiative align closely with the priorities of P.L. 106-193, but emphasize those areas of particular relevance to the ONR and which are consistent with the overall goals of APRISES. Specifically, the development of hydrates and related sources of seafloor methane as logistical fuels for Naval applications, and related marine environmental issues, have been the principal areas of interest; exploratory drilling projects and seafloor stability/safety to date have received limited attention.

For APRISES15, the goals of the Methane Hydrates task were to:

- Advance our understanding of the environmental impacts of natural seeps and accidental releases of methane and other hydrocarbons in the deep ocean;
- Explore the feasibility of sequestering CO₂ in natural methane hydrate reservoirs; and
- Promote international research collaborations on methane hydrates.

Specific technical initiatives that were pursued to attain the above goals included:

- Initiate a laboratory study of hydrate formation on natural gas bubbles and bubble dissolution in seawater using the new HNEI high pressure water tunnel;
- Continue laboratory experiments to identify microbial metabolic pathways that break down methane and other hydrocarbons in the ocean;
- Perform calorimetric experiments to investigate the energetics and rates of CO₂-CH₄ hydrate exchange; and
- Organize the 10th International Workshop on Methane Hydrate R&D.

Technical accomplishments of the APRISE15 Methane Hydrates task are described below.

Hydrate Formation on Natural Gas Bubbles

When methane (CH₄) and other gaseous hydrocarbons are released accidentally into the ocean or from natural bottom seeps, they can lead to significant environmental consequences. These hydrocarbons can dissolve or may escape through the air-ocean interface. Microbial metabolism is recognized as a major sink of hydrocarbon contaminants in the ocean, but the mechanisms and rates of biological degradation and sedimentation are not well understood.

Methane is a potent greenhouse gas that has a global warming potential about 30 times larger than that of carbon dioxide (CO₂) [2]. The release of CH₄ during the aforementioned scenarios could increase its atmospheric inventory which may exacerbate climate change [3,4]. Investigations of the dissolution rate of buoyant natural gas bubbles rising through the oceanic water column are important in assessing environmental impacts since it will affect the resulting concentrations and spatial extent of the contamination zone. Bubbles that dissolve slowly relative to their vertical rise speed will distribute CH₄ and other natural gases over a wider area, resulting in lower concentrations. Furthermore, natural gas bubble plumes entrain ambient seawater as they rise

through the density stratified deep ocean. During this ascent, volumes of cold, dense seawater drawn upward by a plume along with small gas bubbles dispersed in this water may detrain from the plume and form subsurface intrusion layers which are spread laterally by isopycnal transport [5]. Larger bubbles with strong buoyancy can resist this detrainment and continue to ascend toward the surface. Insight acquired from buoyant natural gas simulations is essential for environmental impact assessments.

To develop effective mitigation strategies for methane leakage in the deep ocean, investigations have been conducted to observe bubbles or plumes in the field and to measure bubble dissolution rates in the laboratory. Maini and Bishnoi established a method to hold and observe rising bubbles in a fixed location for an extended period by utilizing a counter flow of water in a high-pressure vessel [6]. They reported that a hydrate film formed on the rising CH₄ bubble. Masutani and Adams used a large pressure vessel to observe pure CH₄ bubbles and oil covered CH₄ bubbles as part of a private-public risk assessment of deep offshore oil and gas production in the Gulf of Mexico [7]. The dissolution process of CH₄ bubbles with and without hydrate films has also been studied previously [8,9]. Warzinski *et al.* and Chen *et al.* performed detailed observations of the hydrate film formation on a CH₄ bubble to elucidate the dissolution process of the bubble [10,11]. These investigations have revealed that, besides impeding dissolution, hydrate formation may also alter gas transport by changing the drag characteristics of the bubbles.

Several *in situ* experiments have examined rising bubbles and natural gas plumes. Topham studied the behavior of natural gas bubbles released into the water column at depths of 650 and 325 m in the Beaufort Sea [12]. Rehder *et al.* released CH₄ and argon or CO₂ at the ocean floor in Monterey Bay and observed rising bubble behavior with a remotely operated vehicle (ROV) [13-15]. As part of the DeepSpill project, a field test was conducted to simulate a deep undersea well blowout in which significant quantities of oil and gas were discharged at a depth of 844 m at the Helland Hansen site in the Norwegian Sea, and the behavior of these plumes was studied [16]. Furthermore, natural gas bubbles released from the seabed were observed via acoustic sounder imaging at the Sakhalin slope in the Sea of Okhotsk, at the mud volcano in the Black Sea, and at Blake Ridge [17-19]. Recently, detailed observations of rising bubbles were performed via tracking with an ROV in the Gulf of Mexico [20,21].

Applying results of these earlier studies, models have been developed to simulate dissolution and dispersion of CH₄ bubbles rising through the oceanic water column. Johansen proposed the Lagrangian DEEPBLOW model to assess oil and gas blowout accidents [22]. Incorporating the results of laboratory and field experiments, Yapa and his colleagues modified Johansen's model, and developed the Clarkson Deepwater Oil and Gas (CDOG) model to predict dissolution and transport of oil and gases in seawater [23-27]. McGinnis *et al.* also proposed a model to simulate the behavior of CH₄ gas rising from the seafloor to the ocean surface [28].

Recently, as part of offshore CH₄-hydrate research and development activities, the Methane Gases from Deepwater (MEGADEEP) model and MEGADEEP-Eco model were created to simulate the diffusion behavior of CH₄ gas released from the seabed [29,30]. These models were applied to CH₄-hydrate activities in the Nankai trough by the MH21 project in Japan [31]. They were also used to simulate CH₄ emission from offshore CH₄-hydrate reservoirs in the East China Sea and in the Japan Sea [32,33].

Previous research has provided significant insight into the dissolution process of CH₄ bubbles in seawater; however, the majority of laboratory experiments have been performed using pure water and field studies have been conducted in seawater. The effect of salts on the dissolution rate of CH₄ bubbles is estimated only indirectly, and studies that made direct comparisons are limited. Furthermore, laboratory experiments mainly focused on the effects of the hydrate film formation on the dissolving bubbles, and only a very small number of measurements have been made of the bubble dissolution rate under non-hydrate forming conditions. In consideration of these deficiencies, we developed a facility and methods to measure the dissolution rate of CH₄ bubbles outside of the hydrate film forming regime. A description of the facility and a sample of preliminary data on the dissolution rate of single CH₄ bubbles are provided below.

Experiments were performed in a facility that can simulate conditions in the ocean from the surface down to 1000 m depth. The HNEI Deep Ocean Simulator (DOS) facility allows continuous monitoring of buoyant gas bubbles for extended periods. A downward flow of water over the rising bubble generates a downward drag force. The flow rate of water over the bubble can be adjusted so that buoyancy and drag forces are balanced and the bubble is held stationary in space. In the frame of reference of the bubble, this simulates buoyant rise through the water column. In this study, dissolution rates of single CH₄ bubbles under dynamic (i.e., advective), non-hydrate-forming conditions were inferred from data on bubble shrinkage over time.

The DOS has an internal volume of about 100 L and can operate safely at internal hydrostatic pressures up to 10.4 MPa. The DOS consists of a pressure vessel equipped with observation windows, a high-pressure water circulation system, a temperature controller, a gas supply system, and an imaging system. Previous studies have confirmed that this system is capable of monitoring the behavior of single and multiple buoyant droplets and bubbles over long time periods [6,7].

Figure 4.1 presents a schematic diagram of the DOS facility. The cylindrical pressure chamber comprises two sections, each approximately 1 m in height. The upper section (146 mm inner diameter) serves as a low-velocity, run-in plenum that supplies the enclosed water tunnel. The plastic water tunnel shown in the inset is mounted inside the 298 mm inner diameter lower section that is equipped with a pair of high-pressure viewports (J.M. Carty Fuseview Sightglass; approximately 100 mm clear aperture; 10.44 MPa maximum operating pressure) positioned opposite one another to allow observation of the bubbles in the water tunnel. Both sections are

fabricated from 316 stainless steel in compliance with all applicable ASME pressure vessel codes. Inner surfaces of the chamber are coated with PTFE.

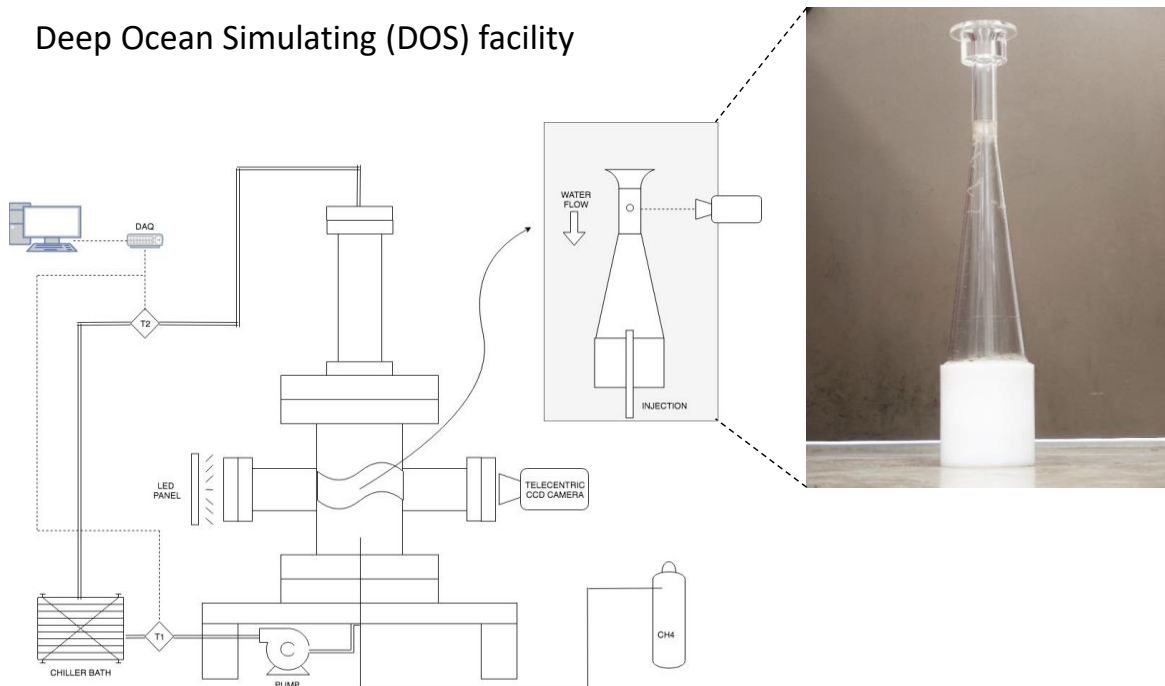


Figure 4.1. Schematic diagram of the Deep Ocean Simulator (DOS) facility.

The system is filled with about 100 L of either tap water or synthetic seawater. While natural seawater was available for the present experiments, complications associated with variability of its properties were encountered in earlier investigations. To minimize this problem, and to ensure that results could be replicated by others, we elected to use artificial seawater with known composition and minimal biological loading.

Synthetic seawater is prepared by mixing Instant Ocean with tap water to obtain a salinity of 3.5 ± 0.2 wt% NaCl. The Instant Ocean aquarium mix contains naturally occurring salts including sodium chloride, magnesium chloride, sodium sulfate, calcium chloride, and potassium chloride [36]. The pressurized liquid in the system is circulated with a variable speed, magnetically coupled gear pump (Micropump model 223/56 C; Leeson Micro Series AC Inverter, maximum discharge rate: 12 L/min). Two bath chillers (Thermo Scientific model ThermoChill III and model IsoTemp 6200) are employed to maintain water temperature in the range extending from 278 to 308 K, with an accuracy of ± 1 K. Water flow rate in the water tunnel can be adjusted between 5 and 50 cm/s. For a dissolving CH₄ bubble with a diameter between 10 and 1 mm, the flow rate in the water tunnel test section was adjusted over a range of approximately 20 to 16 cm/s.

The water tunnel consists of a clear acrylic inlet contraction and constant area viewing section cemented to a polycarbonate diffuser. The diffuser downstream of the viewing section ensures

that gas bubbles under observation are not swept out of the water tunnel as they dissolve, since the downward fluid velocity decreases rapidly by a factor of about 20 from inlet to exit in the diffuser. This allows us periodically to adjust (i.e., reduce) the fluid flow rate and reposition the dissolving bubbles back in the viewing section for continued observation. The inlet contraction of the plastic water tunnel is employed to minimize boundary layers and reduce turbulence levels in the 25.4 mm inner diameter x 102 mm length, cylindrical test (viewing) section.

CH₄ gas prepared by Airgas, Inc. that was used in the experiments had 99.99% purity. The gas was injected into the water from a needle positioned at the base of the pressure vessel.

The clear, constant area viewing section of the water tunnel was aligned horizontally with the two large viewports. Gas bubbles stabilized with the downward flow of water were illuminated with an LED panel (Metaphase Technologies model FR-BL) mounted in front of one viewport and were monitored with a telecentric CCD camera (Prosilica GT1920 with Thorlabs 0.128 Bi-telecentric lens) through the opposite viewport. The telecentric camera lens provided constant magnification across the span of the 25.4 mm inner diameter viewing section, to avoid errors in estimating changes in size over time of the dissolving bubbles as they wandered laterally toward and away from the camera.

Images were recorded at intervals of up to 0.5 s. Images were analyzed every 3 to 30 s depending on the size change rate. Image analysis was done post-experiment with LabView's Vision software. Due to minor bubble movement during image capture, the spatial resolution of the image measurements was estimated to be 0.05 mm.

The shape of the bubble was assumed to be an oblate spheroid, and the major axis (*a*) and the minor axis (*b*) were estimated from the 2D image data. The time change of the spherical diameter (*d_e*) of the equivalent volume (*v*), calculated by Equation 4.1, was investigated.

$$v = \pi (a^2 b) / 6 = \pi d_e^3 / 6 \quad (\text{Eq. 4.1})$$

The Heywood circularity factor (*H*) also was calculated to assess the bubble-shape change. *H* is determined by dividing the observed perimeter of the bubble by the circumference of a circle with the same projected area. Deviations from circularity result in values of *H* > 1. Three or more replicates typically are performed at each test condition.

Figure 4.2 shows a typical image of a CH₄ bubble observed in the high-pressure vessel. The 1.5 mm diameter buoyant bubble is stabilized with a downward flow of water at 288 K, at a pressure of 6.9 MPa.

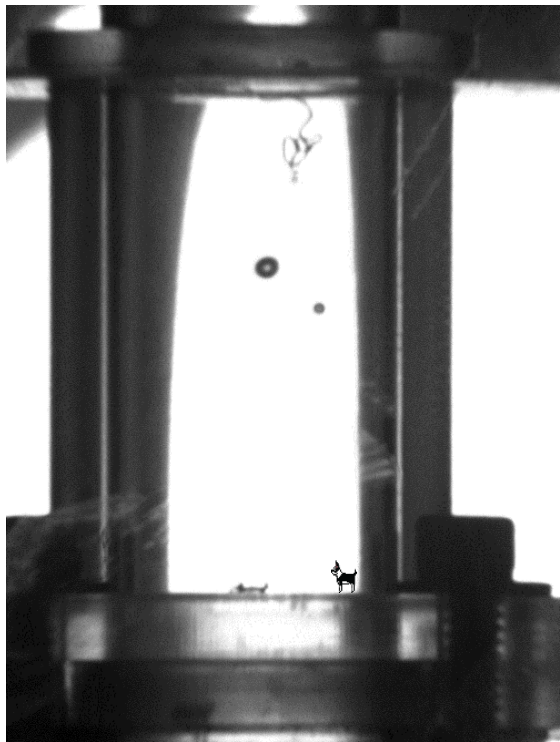


Figure 4.2. CH₄ bubble (~1.5 mm in diameter) in pure water at temperature of 288 K.

Table 4.1 presents a representative data set on the observed shrinkage of the methane bubble over time. The table includes results collected during a test performed at 288 K and 6.9 MPa in pure water over an observation period of 22 minutes. This data is plotted in Figure 4.3.

Bubble dissolution data in the DOS collected over a range of operating temperatures in both tap water and sea water have been analyzed and a manuscript was submitted for review to the peer review journal *Energies*. That manuscript has been accepted for publication and those results will be included in the final report for APRISES16.

Table 4.1. Observed Methane Droplet Shrinkage over Time.

Time [min]	Heywood Number	Equiv. Dia. [in]	Equiv. Dia. [cm]	Volume [in^3]	Volume [cm^3]
1	1.663	0.3423	0.8695	0.0210	0.3443
2	1.634	0.3408	0.8657	0.0207	0.3397
3	1.64	0.3322	0.8438	0.0192	0.3146
4	1.637	0.3250	0.8254	0.0180	0.2945
5	1.65	0.3155	0.8014	0.0164	0.2695
6	1.647	0.3072	0.7802	0.0152	0.2486
7	1.623	0.3033	0.7704	0.0146	0.2394
8	1.687	0.2915	0.7404	0.0130	0.2125
9	1.669	0.2856	0.7255	0.0122	0.1999
10	1.643	0.2775	0.7048	0.0112	0.1833
11	1.649	0.2660	0.6755	0.0098	0.1614
12	1.662	0.2591	0.6581	0.0091	0.1492
13	1.664	0.2472	0.6278	0.0079	0.1296
14	1.681	0.2374	0.6031	0.0070	0.1148
15	1.698	0.2277	0.5783	0.0062	0.1012
16	1.683	0.2225	0.5652	0.0058	0.0945
17	1.677	0.2129	0.5409	0.0051	0.0828
18	1.683	0.2042	0.5187	0.0045	0.0731
19	1.67	0.1974	0.5013	0.0040	0.0660
20	1.67	0.1787	0.4538	0.0030	0.0489
21	1.672	0.1639	0.4164	0.0023	0.0378
22	1.676	0.1625	0.4127	0.0022	0.0368

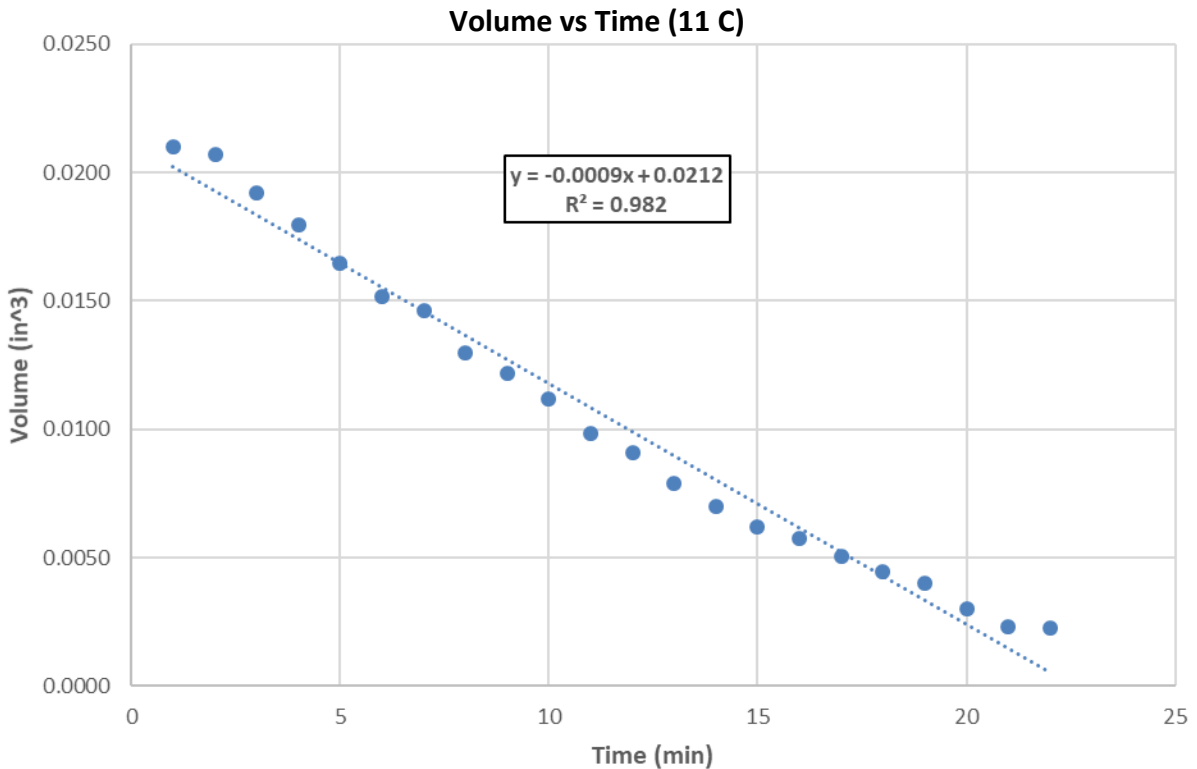


Figure 4.3. Shrinkage of CH₄ bubble in pure water at T = 288 K and P = 6.9 MPa.

Microbial Response to Methane Release in the Ocean

The presence of hydrocarbons, including methane, are known to stimulate biological activity within the ocean water column [35-37].

Sequencing of microbial community DNA using Next-Generation Sequencing techniques (NGS) allow for rapid assessments of biodiversity. These metagenomic studies increase the sensitivity of detection and allow for the identification of species that would be overlooked using traditional methods. Moreover, NGS can be utilized to detect the presence of functional genes. The combination of functional genomics along with community information provide insight into biogeochemical processes.

The use of methane in the experiments performed with the DOS provides a source of carbon source that can support a biological community. Within 24 hours, a visual increase in seawater turbidity is consistently observed after the introduction of methane. The establishment of a significant biological community have implications on the current experiments being performed. While the source of biological contamination is unknown, the artificial seawater mix is probable. The buoyancy and drag forces in the water column are balanced by water counter flow keeping the bubble stationary. Metabolic consumption impact methane dissolution rates and elevated methane contents result in the stimulation of methanotrophic communities [37]. As part of our ongoing

investigations the microbiological community has been estimated to determine if metabolic consumption is an experimental consideration. A description of the methods and key results of this investigation follows.

Microbial communities were examined by collecting two liters of artificial seawater from the DOS after experimental bubbles dissolution experiments were completed (48 hours). In order to concentrate the cells, the 2 liters of artificial seawater was filtered through a Sterile GF/C filter. DNA was extracted from the collected cells using a Qiagen DNeasy Powersoil kit (Cat #12888-100). Successful DNA extraction was confirmed by PCR using 16S rDNA primers, 1492R-27F [38]. Polymerase chain reaction (PCR) was performed using; 0.1 μ M of each primer, 200 μ M dNTP (Cat #4025), 0.625 U Roche Taq Polymerase (Cat #10966-026) and 2.5 μ l of 10x buffer containing 1.5 mM MgCl₂ in a total volume of 25 μ l with distilled water. The thermal program used for this amplification was an initial 2 minutes at 94°C; followed by 30°C cycles of 15s at 94°C, 1 minute at 50°C and 1 minute at 72°C; and finished by a 7 minute final extension at 72°C. The PCR products were then run on a 1% agarose gel with SYBR green in TBE buffer which is a stain that quantifies double stranded DNA. The extracted DNA samples were then sent to the University of Hawai‘i Advanced Studies in Genomics, Proteomics and Bioinformatics (ASGPB) facility for Illumina MiSeq analysis, using short 16S rDNA primer pairs [39].

Metagenomic analysis was performed using Geneious™ and the NCBI Basic Local Alignment Search Tool (BLAST) [40]. The general results from this analysis are presented in Figure 4.4. Of the Alphaproteobacteria, the methylobacteriaceae and methylocystaceae comprised three percent of its total, and for the Gammaproteobacteria, methylococcales comprised 1 percent of its total. These results indicate that with high concentrations of methane, the methanotrophic community remained insignificant and did not influence the experimental results that are reported here.

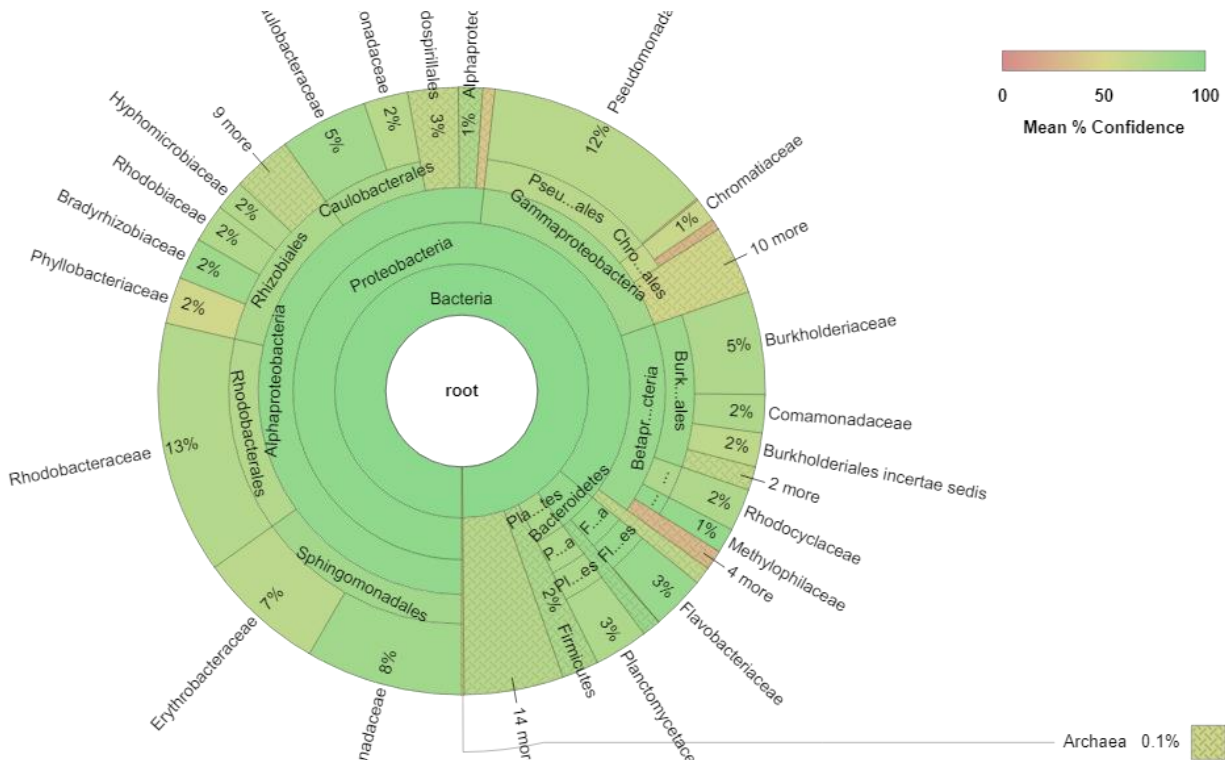


Figure 4.4. 16S rDNA phylogeny for bacteria found growing in the DOS during methane experiments.

CO₂-CH₄ Hydrate Exchange

Injection of CO₂ into methane hydrate reservoirs in sediment has been proposed as a means to destabilize the hydrate to release methane gas for energy, and to sequester CO₂ from the atmosphere. A limited number of laboratory experiments [41,42] suggest that the exchange proceeds too slowly to be viable at a commercial-scale. Recently, however, new theoretical thermodynamic analyses have indicated that gas mixtures of N₂ and CO₂ may improve the kinetics of replacement of CH₄ with CO₂ in hydrate deposits [43]. In order to assess the feasibility of CO₂-CH₄ hydrate exchange for simultaneous methane production and carbon sequestration, experiments were performed employing our Setaram BT2.15 calorimeter to explore the energetics and kinetics of this process. Methods used to conduct this analysis are described below. Data is currently being analyzed and will be reported in the final report for APRISES16.

During these experiments, methane hydrate is formed in the sample cell of a Setaram BT2.15 calorimeter. Figure 4.5 presents a schematic diagram of the CO₂-CH₄ hydrate exchange facility. The calorimeter first is purged of atmospheric air using a vacuum pump and dry nitrogen gas. After purging, it is cooled to -10°C using liquid N₂. Following the protocol for methane hydrate synthesis developed previously and described in earlier HNEI reports, distilled deionized water is sprayed into a liquid N₂ bath to generate fine ice crystals. Crystals smaller than about 200 µm are collected, weighed, and loaded into a sample cell. The assembled cell is then inserted into the cold

calorimeter test well, purged with N₂, and pressurized slowly with pure (99.99%) CH₄ gas prepared by Airgas, Inc.

When the pressure in the cell reached 7.0 MPa (1000 psig), the temperature of the calorimeter was increased from -10°C to -5°C and allowed to equilibrate. Once the calorimeter reached steady-state, the sample temperature was increased from -5°C to 4°C at a rate of 0.1 °C /min. The calorimeter was then held for 12 hours at 4°C, which is above the melting point of ice but below the freezing point of methane hydrate. The calorimeter then was cooled to -10°C. This forced any remaining liquid water, which did not form hydrate, to freeze back to ice.

Following the hydrate formation process the sample cell was depressurized to 0.1 MPa (ambient pressure) and CO₂ gas at room temperature (~25°C) was injected into the cell until the pressure reached 7.00 MPa. The sample was held at 7.00 MPa and -10°C for different lengths of time and the thermogram was recorded over this period. Thereafter, pressure was reduced to 3.6 MPa (500 psig) and temperature was increased to 3°C in order to melt the ice phase.

The CH₄ hydrate next was dissociated by slowly increasing temperature of the sample from 3°C to 5°C and holding the sample at 5°C. The corresponding thermograms exhibited an endothermic signature characteristic of dissociation. Finally, temperature was slowly increased from 5°C to 10°C to melt any CO₂ hydrate that had formed.

If one assumes that the dissociation of CH₄ and CO₂ hydrate do not overlap in the above process, then analysis of the thermograms can provide estimates of the relative amount of these two hydrates in the sample. This is done by dividing the energy absorbed during the two individual hydrate decomposition steps (i.e., the integrated areas under the power vs. time thermograms for the two processes) by the respective hydrate heats of dissociation which are available in the literature.

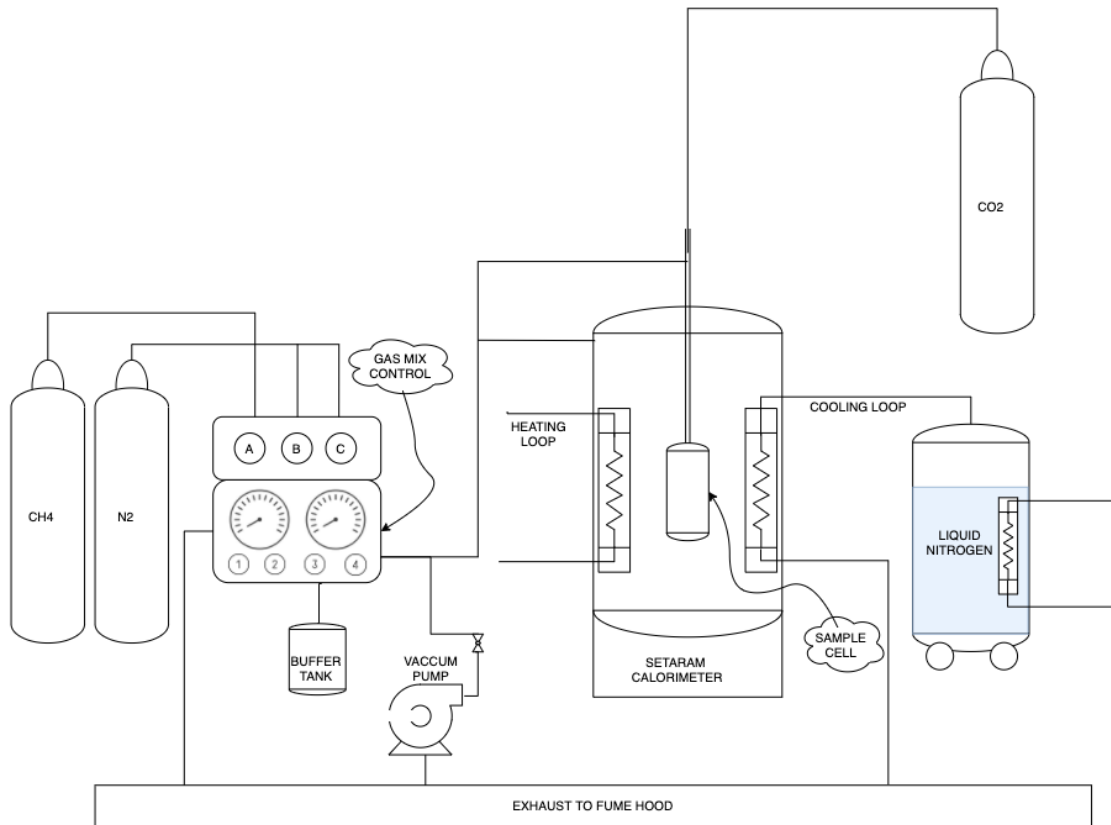


Figure 4.5. Schematic diagram of the CO₂-CH₄ hydrate exchange experimental facility.

Pursuant to the goal of promoting international R&D cooperation on methane hydrates, that was a cornerstone of the Methane Hydrates task of the previous HEET program proposal, HNEI organized the 10th International Fiery Ice Workshop on methane hydrates in 2016. Fiery Ice 2016: The 10th International Workshop on Methane Hydrate Research and Development was held in Honolulu, Hawai‘i, on June 15th to 17th, 2016 at the Imin Conference Center. A total of 60 registrants from the United States, Japan, China, Germany, India, New Zealand, Norway, and the Republic of Korea attended the workshop. The 2.5-day workshop included 7 national reports, 5 breakout sessions, and 20 oral and 25 poster presentations. The key theme of the workshop was “15 Years of Progress and Future Directions.” It highlighted accomplishments and changes in hydrate science and engineering since the first workshop in 2001, and identified directions for the future. The national reports described the present status of gas hydrate research in the United States, China, Korea, Japan, Norway, New Zealand, and Germany. Five breakout sessions were organized around five topics including: 1) fundamental laboratory and modeling studies; 2) exploration and resource assessment; 3) reservoir and production modeling; 4) the path forward: key areas for future R&D; and 5) the impact of cheap fossil fuels on methane hydrate R&D.

The conclusions and recommendations of a subset of breakout sessions held during the 10th and earlier Workshops have been reported in a peer reviewed, open access publication listed below (Uchida, 2017).

When the first Fiery Ice Workshop was held in 2001, projects to produce methane gas from natural gas hydrates had just begun. Since that time, those gas production projects have progressed to field production tests. Fundamental studies of the properties of gas hydrates have undoubtedly played an important role in moving those projects forward. In the paper cited below (Uchida, 2017), we reviewed the discussions that took place in breakout sessions on topics related to fundamental hydrate properties, with the objective of reflecting on challenges over the years, changing priorities, and the progress that has been made in the area.

As is the case in almost all scientific areas of endeavor, studies of hydrate fundamental properties suffer, to a degree, from a lack of access to data collected by various groups in different countries, and variations in the results from supposedly similar experiments due to differences in materials and methods. Discrepancies between the results of bench and field tests reflect not only scale issues, but also the sensitivity of the hydrate system to numerous and complicated factors such as structural inhomogeneities, impurities, and history. During the breakout sessions, a number of collaborative efforts were proposed that could help mitigate these problems, but success to date has been limited.

It was the consensus of workshop participants that gas hydrate R&D will continue to progress quickly in the near term, and that models should soon be able to provide reliable estimates of the production rates of natural gas from the gas hydrate reservoirs and that a host of practical hydrate applications will emerge, such as the storage and transportation of natural gas.

Publications and Presentations

Peer-Reviewed Publications

1. Uchida, T., Kvamme, B., Coffin, R.B., Tenma, N., Oyama, A., and Masutani, S.M. (2017). Review of fundamental properties of gas hydrates: breakout sessions of the International Workshop on Methane Hydrate Research and Development. *Energies*, 10(10), 747.

References

- [1] Oyama, A. and Masutani, S.M. (2017). A review of the methane hydrate program in Japan. *Energies*, 10(10), 1447.
- [2] U.S. Environmental Protection Agency. (n.d). Understanding Global Warming Potentials. Retrieved from <https://www.epa.gov/ghgemissions/understanding-global-warming-potentials>.
- [3] Schmidt, G.A. and Shindell, D.T. (2003). Atmospheric composition, radiative forcing, and climate change as a consequence of a massive methane release from gas hydrates. *Paleoceanography*, 18(1), 1004.

- [4] Carozza, D.A., Mysak, L.A., and Schmidt, G.A. (2011). Methane and environmental change during the Paleocene-Eocene thermal maximum (PETM): Modeling the PETM onset as a two-stage event. *Geophysical Research Letters*, 38, L05702.
- [5] Socolofsky, S.A., Adams, E.E., and Sherwood, C.R. (2011). Formation dynamics of subsurface hydrocarbon intrusions following the Deepwater Horizon blowout. *Geophysical Research Letters* 38, L09602.
- [6] Maini, B.B. and Bishnoi, P.R. (1981). Experimental investigation of hydrate formation behaviour of a natural gas bubble in a simulated deep sea environment. *Chemical Engineering Science*, 36(1), 183-189.
- [7] Masutani, S.M. and Adams, E.E. (2000). Experimental study of multi-phase plumes with application to deep ocean oil spills, Final Report for Contract 1435-01-98-CT-30964, U.S. Department of the Interior.
- [8] Bigalke, N.K., Rehder, G., and Gust, G. (2009). Methane hydrate dissolution rates in undersaturated seawater under controlled hydrodynamic forcing. *Marine Chemistry*, 115(3-4), 226-234.
- [9] Bigalke, N.K., Enstad, L.I., Rehder, G., and Alendal, G. (2010). Terminal velocities of pure and hydrate coated CO₂ droplets and CH₄ bubbles rising in a simulated oceanic environment. *Deep Sea Research Part I: Oceanographic Research Papers*, 57(9), 1102-1110.
- [10] Warzinski, R.P., Lynn, R., Haljasmaa, I., Leifer, I., Shaffer, F., Anderson, B.J., and Levine, J.S. (2014). Dynamic morphology of gas hydrate on a methane bubble in water: Observations and new insights for hydrate film models. *Geophysical Research Letters*, 41(19), 6841-6847.
- [11] Chen, L., Levine, J.S., Gilmer, M.W., Sloan, E.D., Koh, C.A., and Sum, A.K. (2014). Methane hydrate formation and dissociation on suspended gas bubbles in water. *Journal of Chemical & Engineering Data*, 59(4), 1045-1051.
- [12] Topham, D.R. (1978). Observations of the formation of hydrocarbon gas hydrates at depth in seawater. Catalogue No. IOS Note-4, 8.
- [13] Rehder, G., Brewer, P.W., Peltzer, E.T., and Friederich, G. (2002). Enhanced lifetime of methane bubble streams within the deep ocean. *Geophysical Research Letters*, 29(15), 21-1.
- [14] Rehder, G., Kirby, S.H., Durham, W.B., Stern, L.A., Peltzer, E.T., Pinkston, J., and Brewer, P.G. (2004). Dissolution rates of pure methane hydrate and carbon-dioxide hydrate in undersaturated seawater at 1000-m depth. *Geochimica et Cosmochimica Acta*, 68(2), 285-292.
- [15] Rehder, G., Leifer, I., Brewer, P.G., Friederich, G., and Peltzer, E.T. (2009). Controls on methane bubble dissolution inside and outside the hydrate stability field from open ocean field experiments and numerical modeling. *Marine Chemistry*, 114(1-2), 19-30.
- [16] Johansen, Ø., Rye, H. and Cooper, C. (2003). DeepSpill—Field Study of a Simulated Oil and Gas Blowout in Deep Water. *Spill Science & Technology Bulletin*, 8(5-6), 433-443.
- [17] Maksimov, A.O. and Sosedko, E.V. (2005). Dynamics of sea bubbles covered by a hydrate skin. XVI Session of the Russian Acoustical Society, 459-462.

- [18] Greinert, J., Artemov, Y., Egorov, V., De Batist, M., and McGinnis, D. (2006). 1300-m-high rising bubbles from mud volcanoes at 2080m in the Black Sea: Hydroacoustic characteristics and temporal variability. *Earth and Planetary Science Letters*, 244(1-2), 1-15.
- [19] Juanes, R. (2018). Fate of Methane Emitted from Dissociating Marine Hydrates: Modeling, Laboratory, and Field Constraints. U.S. Department of Energy Project No. DOE-MIT-0013999.
- [20] Wang, B., Socolofsky, S.A., Breier, J.A., and Seewald, J.S. (2014). Observations of bubbles in natural seep flares at MC 118 and GC 600 using in situ quantitative imaging. *Journal of Geophysical Research: Oceans*, 121(4), 2203-2230.
- [21] Johansen, C., Todd, A.C., and MacDonald, I.R. (2017). Time series video analysis of bubble release processes at natural hydrocarbon seeps in the Northern Gulf of Mexico. *Marine and Petroleum Geology*, 82, 21-34.
- [22] Johansen, Ø. (2000). DeepBlow – a Lagrangian Plume Model for Deep Water Blowouts. *Spill Science & Technology Bulletin*, 6, 103-111.
- [23] Yapa, P.D., Zheng, L., and Chen, F. (2001). A Model for Deepwater Oil/Gas Blowouts. *Marine Pollution Bulletin*, 43(7-12), 234-241.
- [24] Zheng, L., Yapa, P.D., and Chen, F. (2002). A model for simulating deepwater oil and gas blowouts – Part I: Theory and model formulation. *Journal of Hydraulic Research*, 41(4), 339-351.
- [25] Zheng, L. and Yapa, P.D. (2002). Modeling gas dissolution in deepwater oil/gas spills. *Geophysical Research Letters*, 29(15), 21-1.
- [26] Chen, F. and Yapa, P.D. (2003). A model for simulating deep water oil and gas blowouts - Part II: Comparison of numerical simulations with “Deepspill” field experiments. *Journal of Hydraulic Research*, 41(4), 353-365.
- [27] Yapa, P.D. and Chen, F. (2004). Behavior of oil and gas from deepwater blowouts. *Journal of Hydraulic Engineering*, 130(6), 540-553.
- [28] McGinnis, D.F., Greinert, J., Artemov, Y., Beaubien, S.E., and Wüest, A. (2006). Fate of rising methane bubbles in stratified waters: How much methane reaches the atmosphere?. *Journal of Geophysical Research: Oceans*, 111(C9).
- [29] Yapa, P.D., Dasanayaka, L.K., Bandara, U.C., and Nakata, K. (2010). A model to simulate the transport and fate of gas and hydrates released in deepwater. *Journal of Hydraulic Research*, 48(5), 559-572.
- [30] Wimalaratne, M.R., Yapa, P.D., Nakata, K., and Premathilak, L.T. (2015). Transport of dissolved gas and its ecological impact after a gas release from deepwater. *Marine Pollution Bulletin*, 100(1), 279-288.
- [31] Nakata, K., Arata, N., and Yapa, P.D. (2015). Development of a model to simulate methane gas and methane hydrates plumes in deepwater. *Journal of Advanced Marine Science and Technology Society*, 21(2), 37-57 (in Japanese with English abstract).
- [32] Premathilake, L.T., Yapa, P.D., Nissanka, I.D., and Kumarage, P. (2016). Impact on water surface due to deepwater gas blowouts. *Marine Pollution Bulletin*, 112(1-2), 365-374.

- [33] Takagi, Y., Kawahara, S., Okano, Y., and Kato, N. (2017). Numerical Simulation of Methane Seeping from the Seabed in the Japan Sea. *Journal of Chemical Engineering of Japan*, 50(4), 244-253.
- [34] Hazen, T.C., Dubinsky, E.A., DeSantis, T.Z., Andersen, G.L., Piceno, Y.M., Singh, N., et al. (2010). Deep-sea oil plume enriches indigenous oil-degrading bacteria. *Science*, 330, 204-208.
- [35] Hazen, T.C., Prince, R.C., and Mahmoudi, N. (2016). Marine oil biodegradation. *Environmental Science Technology*, 50, 2121–2129.
- [36] Steinle L., Graves C.A., Treude T., Ferre B., Biastoch A., Bussman I., Berndt C., Krastel S., James R.H., Behrens E., Boning C.W., Greinert J., Sapart C.J., Scheinert M., Sommer S., Lehmann M.F., and Niemann H. (2015). Water column methanotrophy controlled by a rapid oceanographic switch. *Nature Geoscience*, 8, 378-382.
- [37] Bornemann, M., Bussman, I., Tichy, L., Deutzmann, J., Schink, B., and Pester, M. (2016). Methane release from sediment seeps to the atmosphere is counteracted by highly active Methylococcaceae in the water column of deep oligotrophic Lake Constance. *FEMS Microbiology Ecology*, 92(8), fiw123.
- [38] Dorsch, M., Lane, D., and Stackebrandt, E. (1992) Towards a phylogeny of the genus *Vibrio* based on 16S rRNA sequences. *International Journal of Systematic and Evolutionary Microbiology*, 42(1), 58-63.
- [39] Klindworth, A., Pruesse, E., Schweer, T., Peplies, J., Quast, C., Horn, M., and Glöckner, F.O. (2013). Evaluation of general 16S ribosomal RNA gene PCR primers for classical and next-generation sequencing-based diversity studies. *Nucleic Acids Research*, 41(1), e1.
- [40] Altschul, S.F., Gish, W., Miller, W., Myers, E.W., and Lipman, D.J. (1990). Basic local alignment search tool. *Journal of Molecular Biology*, 215(3), 403-410.
- [41] Deusner, C., Bigalke, N., Kossel, E., and Haeckel, M. (2012). Methane production from gas hydrate deposits through injection of supercritical CO₂. *Energies*, 5(7), 2112-2140.
- [42] Boswell, R., Schoderbek, D., Collett, T.S., Ohtsuki, S., White, M., and Anderson, B.J. (2017). The Igñik Sikumi Field Experiment, Alaska North Slope: design, operations, and implications for CO₂-CH₄ exchange in gas hydrate reservoirs. *Energy Fuels*, 31(1), 140–153.
- [43] Kvamme, B., Kuznetsova, T., Sapate, A., and Qorbani, K. (2016). Thermodynamic implications of adding N₂ to CO₂ for production of CH₄ from hydrates. *Journal of Natural Gas Science Engineering*, 35(B), 1594-1608.

TASK 5: SECURE MICROGRIDS

“Microgrids and Grid Integration” tasks initiated under previous APRISES awards have continued with expansion of secure microgrid research efforts at multiple sites including the islands of O‘ahu, Moloka‘i, and Maui, Coconut Island (near-shore O‘ahu), the University of Hawai‘i at Mānoa

campus, U.S. Marine Corps Camp Foster in Okinawa, Japan, U.S. Marine Corps Base Hawai‘i in Kāne‘ohe, Hawai‘i, and elsewhere.

Under this task, HNEI has not only continued testing of distributed energy technologies and research supporting the integration of advanced technologies into smart, secure, resilient microgrids, but also analyzed and evaluated data from distributed energy resource production and grid performance collected across multiple projects and varied demonstration environments. In addition to renewable energy generation and active management and control of the energy systems, this effort includes the development and performance assessment of innovative technologies and methodologies aimed to improve or ensure the operability and resiliency of the electricity grid during natural disasters and intentional acts of disruption. The work described in the following sections was conducted primarily by HNEI’s **GridSTART** (Grid System Technologies Advanced Research Team).

HNEI GridSTART is continuing efforts to complete a new facility called the **GridSTART** Laboratory at the University of Hawai‘i Marine Center (UHMC), located at Pier 35 in Honolulu Harbor. This new lab enables HNEI’s ongoing research across several active projects described below and also directly supported HNEI’s enhanced capabilities on grid integration, smart grids, microgrids, DC systems, and other advanced grid related research topics. The lab is highly flexible and is the first of its kind in Hawai‘i — able to test AC and DC equipment, systems, and microgrids technologies within a representative and tightly controlled electrical environment. Additional information on this lab can be found on HNEI’s website.

5.1 Moloka‘i Dynamic Load Bank

The island of Moloka‘i is one of the smaller Hawaiian Islands in the central Pacific Ocean. Its isolated power system has a peak demand of 5.7 MW, a minimum evening demand of 2.2 MW and serves a rural population of approximately 7,300 residents. At the start of 2019, the island had approximately 2.3 MW of distributed solar photovoltaic (PV) generation installed and approved for installation, which is predominantly behind-the-meter rooftop systems, and a 100 kW grid-tied hydro project.

Among the challenges faced by utilities to integrate very high levels of rooftop solar PV on isolated island grids is maintaining a minimum reliable operating level of diesel generators during times of high PV production. High PV production can force generators below their required minimum operating point and the uncontrolled “excess energy” produced by the PV systems can cause degrading grid reliability and operating risk to unacceptable levels.

In March 2015, Maui Electric Company, Ltd. (MECO) informed customers that the Moloka‘i grid had reached its system-level PV hosting capacity limit. Since that time, customer applications for an additional 665 kW of distributed PV systems were held in a queue pending interconnection approval by the utility. In total, there was in excess of 3 MW of distributed generation installed, approved, or in the queue on the Moloka‘i system, which has a minimum daytime gross load of only 3.7 MW. The system-level PV hosting constraint is a function of the daytime load on the island, the uncontrolled power production from the existing and proposed new grid-tied PV systems in the queue, and the minimum reliable operating level of the must-run diesel generation on the island. The diesel generation on the island has a minimum reliable operating point of 1.3 MW; therefore, with a minimum daytime load of 3.7 MW, the utility determined that there is only room to accommodate a maximum of 2.4 MW of uncontrolled PV capacity on the system. Further, the high penetration of PV on the grid can exacerbate system stability challenges during foreseeable contingency events, such as a sudden loss of a generating unit or a power line fault, causing the system frequency to drop below 57 Hz within a few cycles. These sudden drops in frequency in turn cause distributed PV systems to trip offline, and this cascade effect can lead to an increase in load shedding or a system-wide blackout.

This project, a joint HNEI and MECO initiative, deployed a custom controlled Dynamic Load Bank (DLB) to deliver a practical, reliable, and inexpensive means to prevent the baseload diesel generators from operating below their minimum dispatch level while enabling the grid connection of significantly more rooftop PV on Moloka‘i island. Lessons from this project will support enabling high penetration of distributed PV systems on microgrids and island power systems.

Specifically, this project analyzes the performance and effectiveness of a DLB as an “energy safety valve” to provide a near-term solution for increased solar interconnections and longer-term grid management asset for small island grid and microgrid applications. In this application, the DLB rapidly adds load to the Moloka‘i system using secure communications within the power plant when needed to balance the grid during infrequent periods of excess solar energy production. Analysis in Figure 5.1.1 illustrates that the potential for excess energy production by proposed rooftop PV systems held in the queue would occur very infrequently. By absorbing a mere 3.9 MWh of excess solar energy with the DLB, annual production of a significant 1.1 GWh of clean solar energy is enabled (with a commensurate reduction in fossil energy use) through the interconnection of all 665 kW of distributed PV in the queue. In contrast, investment in a battery energy storage system to capture the 3.9 MWh of excess solar energy production annually is not economically justified.

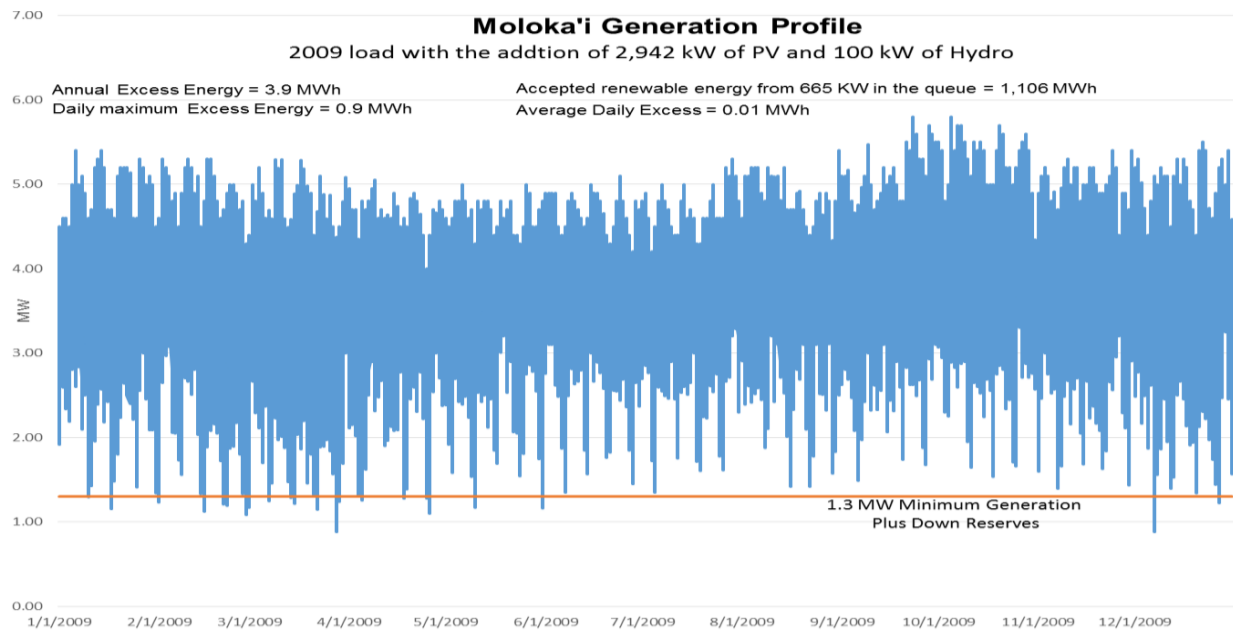


Figure 5.1.1. Prospective Moloka‘i net load profile with added PV.

Under APRISES14, control algorithms for the primary use case of excess energy management were tested and verified. In November 2018, upon the load bank commissioning and implementation of these automated controls, the utility was able to add an additional 725 kW of distributed PV capacity to the system (even more than the 665 kW earlier held in queue by the utility). Extended research in DLB controls development were proposed and planned to deliver additional grid value from this asset, such as fast frequency response to system dynamic events.

Under APRISES15, HNEI and MECO have conducted field tests to determine if the DLB is capable of meeting the demands of fast frequency response. The tests included: (1) measuring the accuracy of the frequency readings from the DLB and (2) measuring the latency between the Real-Time Automated Controller (RTAC) and the DLB. If the DLB was able to accurately read the grid frequency, it would eliminate the need for an external sensor. If the DLB could be controlled with a minimal time delay from the RTAC, it could be used for fast frequency response and lessen the severity of load shedding and over frequency events.

A PQube power meter with GPS time synchronization was installed at the DLB as a reference meter to verify the DLB readings. Data recorded simultaneously from the DLB and the PQube were compared to verify the accuracy of the DLB frequency readings and to measure the communication latency between the RTAC and the DLB. As shown in Figure 5.1.2, the RTAC was physically installed close to the DLB to minimize communication latency. The RTAC and DLB communicate over Ethernet cables using Modbus TCP/IP as shown in Figure 5.1.3.

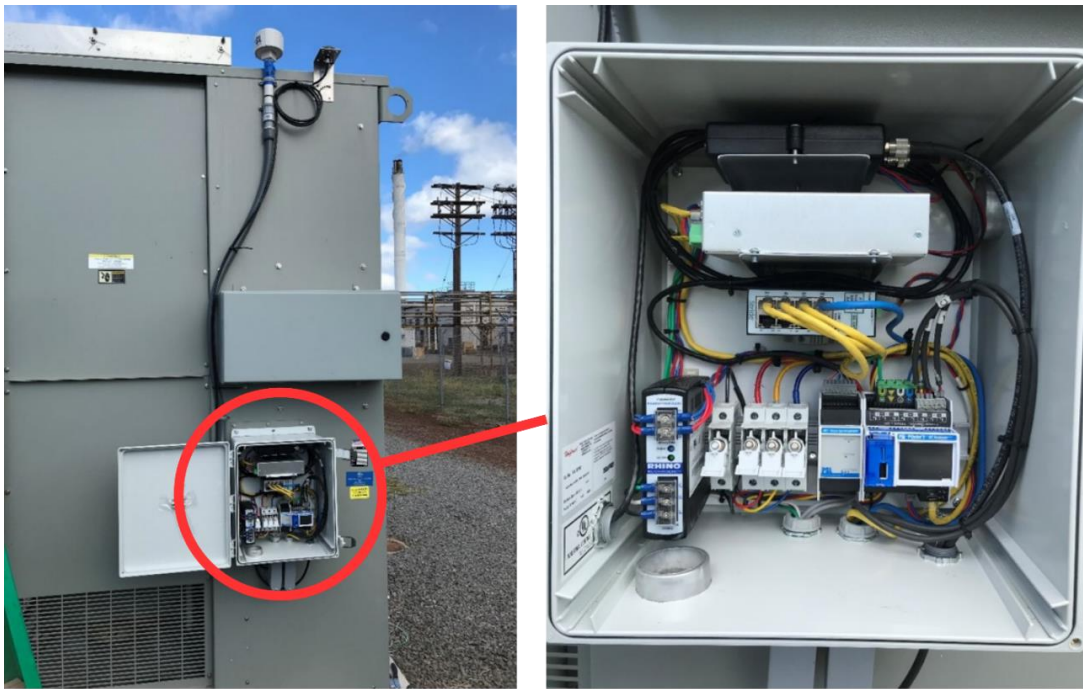


Figure 5.1.2. New control box containing the RTAC and reference PQube meter physically located near the DLB.

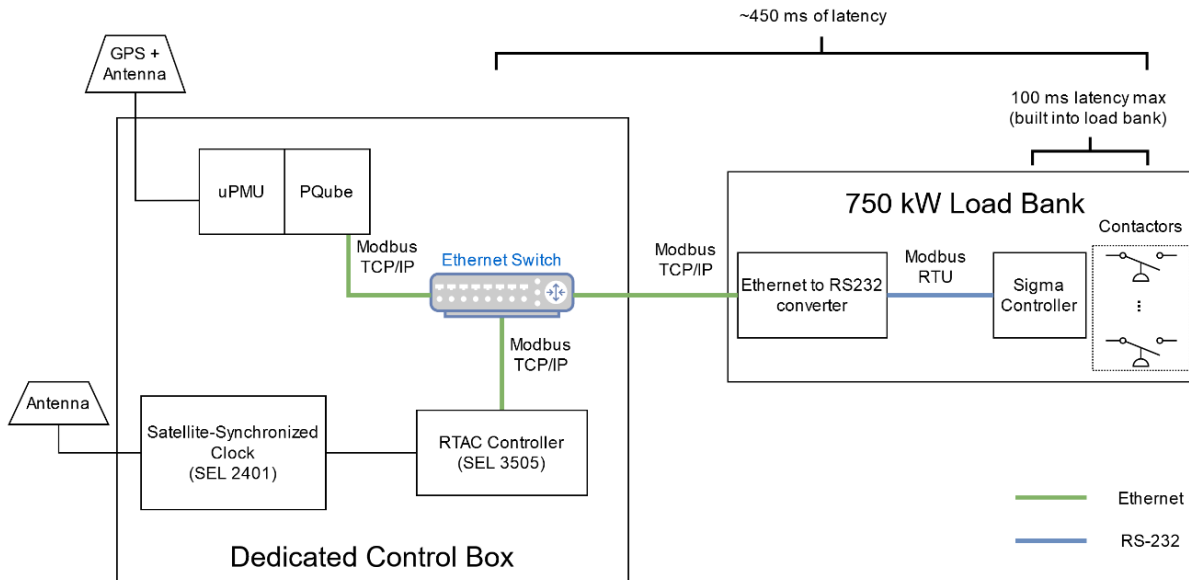


Figure 5.1.3. Block diagram of the DLB latency test.

Figure 5.1.4 shows relative frequency error measured by the DLB compared with the reference PQube power meter. As seen in the figure, the frequency measurements from the DLB are read every 200 ms (5 Hz) and can vary about ± 0.1 Hz from the reference. The PQube power meter used as a reference has an accuracy of $\pm 0.01\%$ with a resolution of 0.0001 Hz, while the DLB has an accuracy of only $\pm 0.2\%$ with a resolution of 0.01 Hz.

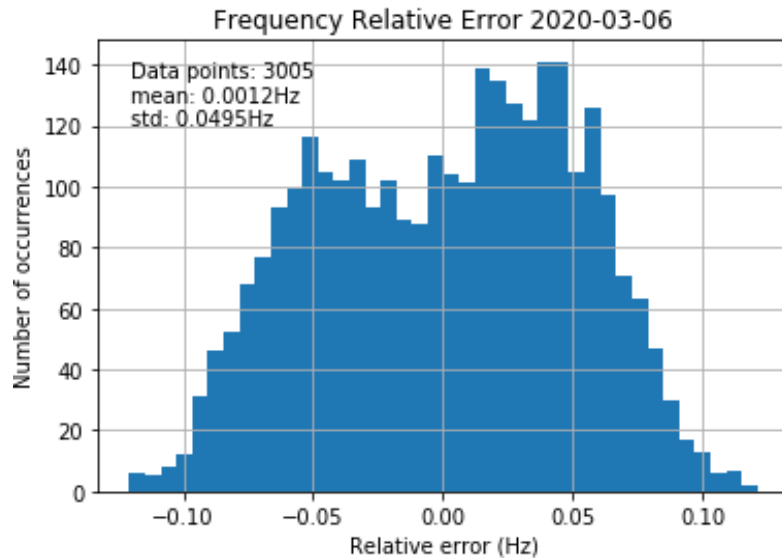


Figure 5.1.4. Relative frequency error of the DLB compared with the reference PQube power meter.

The latency test results shown in Figure 5.1.5 demonstrate that there is a mean latency of approximately 450 ms from the time when the RTAC sends a load change command to the time when the contactors in the DLB switch and change the load. Of the 450 ms of mean latency, a maximum of 100 ms of “built-in delay” comes from the time the DLB’s Sigma Controller receives the command to the time the contactors change (see Figure 5.1.3). This means the theoretical lowest total latency for the system is about 100 ms.

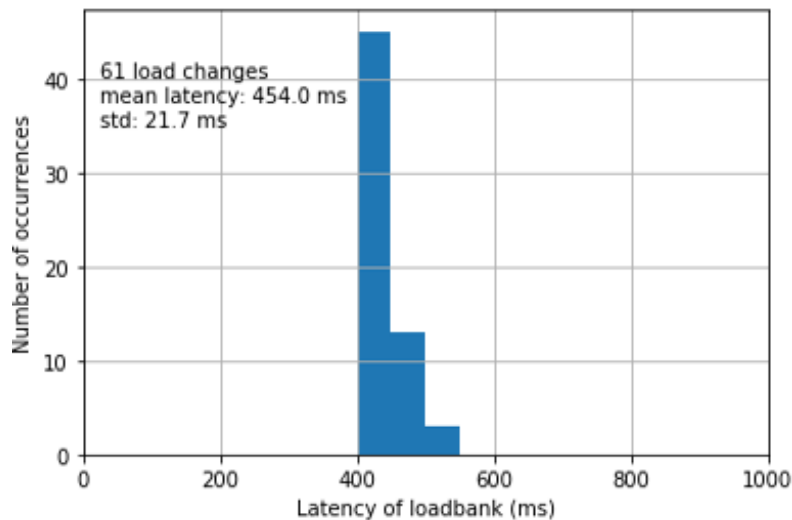


Figure 5.1.5. Latency test results.

As Figure 5.1.6 shows, a possible solution to minimize latency is to use Modbus RTU directly from the RTAC to the DLB. Protocol overhead and translation steps used in Modbus TCP/IP may be adding significant delays in the communication between the RTAC and the DLB.

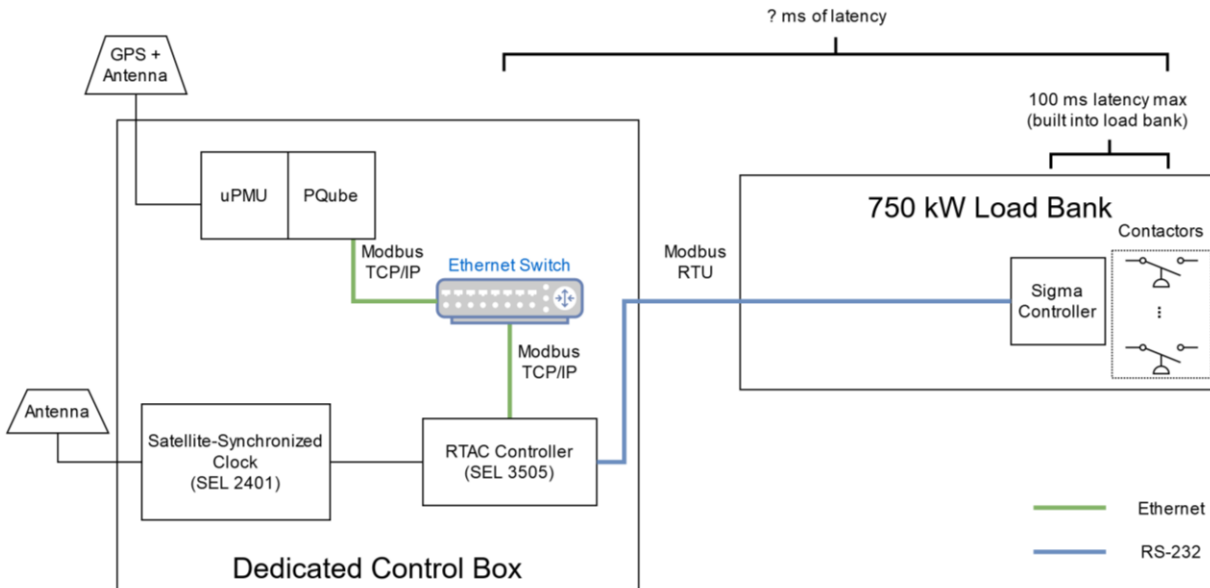


Figure 5.1.6. Proposed block diagram for minimizing latency by using Modbus RTU directly from the RTAC to the DLB.

This information was presented to MECO, and a decision has yet to be made if the capabilities of the DLB are adequate to help mitigate over-frequency and under-frequency events. HNEI GridSTART is continuing its valued partnership with MECO in evaluating the potential to develop additional grid stabilizing control algorithms that can rapidly react to system disruptions. Stacking added functionality such as automatic frequency response will increase both utility and customer value return on the very modest investment in DLB technology.

5.2 Conservation Voltage Reduction Demonstration

The primary goal of the project is to demonstrate energy efficiency through advanced Conservation Voltage Reduction (CVR) on a section of the distribution circuit supplying the Plaza Housing complex at U.S. Marine Corps (USMC) Camp Foster in Okinawa, Japan. This project involves technology development, field implementation, test, and evaluation of grid improvement technologies.

Working in close collaboration with USMC Facilities personnel in Okinawa, a 13.8 kV distribution circuit called “Feeder F6A” was selected for the CVR demonstration. This single feeder has approximately 56 distribution service transformers and is fed by a large substation transformer providing power to a total of ten feeders. To achieve the project’s objectives while keeping within its research scope, budget, and implementation scale, a section of Feeder F6A serving the Plaza Housing complex was identified for the CVR control. The CVR controlled feeder section was isolated with a voltage regulator (VR) to manage and control the voltage at “downstream” service

transformers, essentially behaving as a substation transformer load tap changer for the limited section of the feeder under test.

Specifically, seven distribution service transformers located on a branch end of Feeder F6A were identified for the CVR demonstration. Five out of the seven distribution service transformers had existing advanced metering infrastructure (AMI) meters and communications already installed. A new distribution pad mounted VR in conjunction with near real-time voltage recordings taken at the transformers and communicated back to the VR controller will regulate the primary voltage of these seven transformers. In turn, the VR will manage the customer service voltages to the lower limit of the $\pm 5\%$ acceptable ANSI voltage range. A reduction in energy consumption in the range of 0.7% to 0.9% for every 1% reduction in voltage is expected. This is the primary value proposition of effective CVR implementation – reduced energy use by more effective management of customer service voltage.

Figure 5.2.1 is an electrical one-line schematic of the project area. The existing electrical infrastructure integrated with new technology deployed under this project include the new VR and controls (with associated by-pass switch) located at GS 32, seven distribution service transformers powering an array of loads representative of those normally found on a military base (e.g., Officer's club commercial load, troop barracks, and residential housing), metering at service transformers and AMI radio network communications, an HNEI GridSTART developed reactive power voltage management source and controller installed at TH 415, and a 5 kW rooftop PV system located on a building served from TH 415.

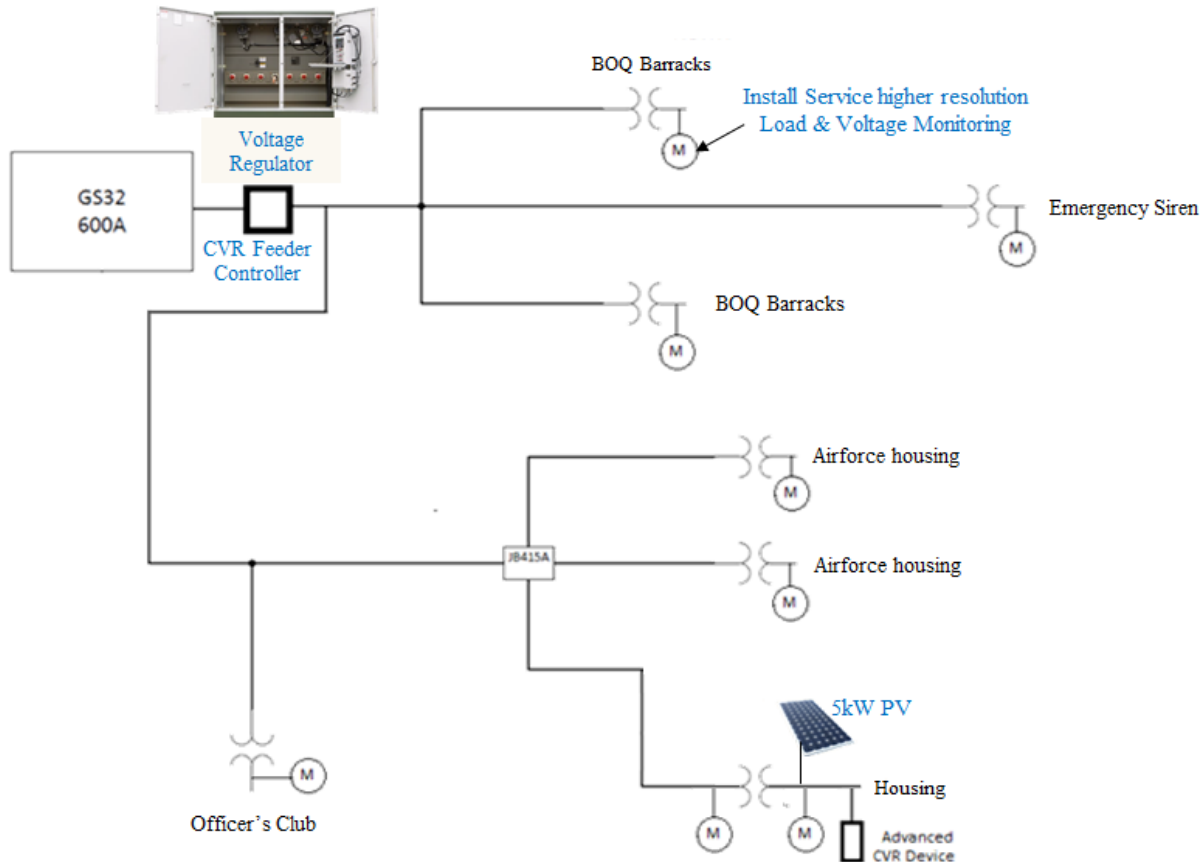


Figure 5.2.1. Project demonstration area electrical one-line schematic.

Under APRISES14 funding, the proposed CVR control algorithm and the associated communications between the field meters and the CVR controller were validated utilizing the hardware-in-the-loop (HIL) test platform in HNEI's GridSTART Laboratory. In addition, a user-interface was developed to provide USMC Okinawa personnel with information regarding the status of the VR and HNEI-controller. Webpages hosted on the HNEI-controller allow for remote monitoring of the system. The HIL testing and user interface were discussed in more detail in the APRISES14 Final Technical Report, available on the HNEI website.

Working closely with USMC Okinawa base personnel, HNEI also completed the electrical installation drawings and developed the bid package for the final construction and field installation work for the VR and by-pass switch installation, and all associated electrical ties. The bid package was issued, and a construction contract was awarded. To ensure that the VR installation, site acceptance testing, and equipment commissioning would be performed properly, HNEI GridSTART carefully defined the scope of work for this element of project execution in close collaboration with Eaton, the manufacturer of the VR and by-pass switch.

The construction services that were initially scoped and procured under APRISES14 were essentially completed under APRISES15, except for the final commissioning work due to COVID-

19 travel restriction delays, as discussed further below. Fortunately, with the strong support of USMC GF Facilities Engineering Division of Camp Butler, HNEI was able to obtain the services of Seabees companies deployed to Okinawa. Field construction work on our project was utilized as part of their training on building electrical infrastructure. HNEI obtained all of the required building materials and Seabees provided the labor to install the underground electrical conduits and concrete pad required for the installation of the VR and bypass switch as shown in Figure 5.2.2. The installation required the coordination of multiple system power outages, with each outage required to be on a Monday unless it conflicted with a holiday or an Officer's Club event. Further, consecutive outages had to be scheduled at least two weeks apart. These limitations along with a rotation of Seabees companies during the work resulted in some scheduling challenges; notwithstanding, the infrastructure work was completed by the Seabees in February 2020.



Figure 5.2.2. Seabees working to install the conduits and concrete pad.

Once the electrical infrastructure was installed, HNEI's electrical contractor was able to reconfigure the distribution circuits coming from GS 32 to incorporate the VR and bypass switch into the distribution system serving the seven transformers as shown in Figure 5.2.3.



Figure 5.2.3. HNEI's electrical contractor installing the electrical cables and terminations.

The work of the electrical contractor, coordinated to slightly overlap in February 2020 with Seabees' field work, was completed in March 2020 with the installation of the VR and bypass switch shown in Figure 5.2.4. Unfortunately, as the electrical work was being completed, the global COVID-19 pandemic was accelerating, resulting in international travel being severely restricted or prohibited. Due to the travel restrictions, HNEI Grid**START** has been unable to travel to Okinawa to commission the VR and place it into service. Full project field commissioning and start of the operational research phase of the project will be done under future APRISES funding once travel restrictions are lifted.



Figure 5.2.4. Installed VR and bypass switch.

During and after the installation of the VR, HNEI continued its research partnership with USMC GF Facilities Engineering Division, addressing issues related to the USMC's existing AMI mesh communication system that will be used for data transfer and control by the CVR system. The communication issues were suspected to stem from salt air corrosion of the antennas at some of the existing AMI meter sites. HNEI GridSTART contracted with another important partner on this project, Okinawa Enetech, to replace and weatherize the problematic antennas. These repairs, shown in Figure 5.2.5, were successful in fixing the communication issues.

TS 4029

- ✓ Replacement of Antenna and Coax Cable
- ✓ Weatherproofing



Figure 5.2.5. Example of the antenna replacement work.

The project was also challenged by several failures of the pQube meters that were installed to measure the voltage at each transformer. The pQube manufacturer suspected that the failures were due to condensation induced moisture build-up in the meter enclosure (a function of the humid tropical environment in Okinawa) which then caused super capacitors in the pQube meter to corrode and fail. Accordingly, the pQube meters were tested to see if they could operate without super capacitors to eliminate the mode of failure. It was determined that the pQubes would operate sufficiently without the super capacitors, and the pQube manufacturer agreed to remove the super capacitor from spare meters that HNEI had in its inventory. HNEI will replace the pQubes in the field with pQubes that have had the super capacitor removed. In addition, a small adhesive strip heater will be installed in the meter enclosures to drive out condensate in the box and reduce the likelihood of further pQube failures.

Under future APRISES funding, HNEI intends to engage Okinawa Enetech to implement the pQube meter exchange and heater installation. Once the COVID-19 travel restrictions are lifted, HNEI will travel to Okinawa with an engineer from VR manufacturer Eaton to commission the VR and place it into service. HNEI personnel will also field install and operationalize the CVR system controls, enable all system communications, and initiate full operation, test and initial evaluation of the CVR system.

5.3 Coconut Island DC Microgrid

Coconut Island (Moku o Lo‘e) is a 28-acre (113,000 m²) island in Kāne‘ohe Bay off the island of O‘ahu and is home to the Hawai‘i Institute of Marine Biology (HIMB) of the University of Hawai‘i. One of HIMB’s goals is to make the island and its research facilities a model for sustainable systems. As such, it is an ideal site for a renewable energy technology-based test bed, particularly representative of an isolated location vulnerable to energy disruption, yet serving critical power needs essential to the research and educational mission of HIMB. This island is an inherent microgrid served via an undersea electrical connection tied to a single distribution circuit owned and operated by the local utility on O‘ahu. The tropical marine features of the island further its attractiveness as a unique microgrid test bed. Its exposure to persistent on-shore winds and highly corrosive salt spray allows for material and technology testing in a micro-climate representative of those potentially encountered in coastal installations of Navy’s interest.

The Coconut Island DC Microgrid Project was initiated under previous APRISES funding with the project objective of demonstrating the performance and resilience of a DC microgrid designed to serve loads within two buildings on Coconut Island, including reliable power to critical loads during interruptions of grid supplied power, and providing the island with clean electrified transportation options powered primarily by the sun. The project has the following goals:

- Demonstrate innovative new clean energy technologies;
- Reduce island energy dependence upon the local utility and the existing aged undersea electrical service tie, enhancing energy resilience for the selected critical loads;
- Provide a research platform to study DC microgrid resources and loads; e.g., energy storage and supporting technology and DC power appliances, in a tropical coastal environment;
- Increase island energy sustainability; and
- Provide solar electric powered land and sea based transportation options for HIMB.

The project integrates a DC distribution system into two existing buildings on the island, the Marine Mammal Research Project (MMRP) building and the adjacent Boat House, both depicted in Figure 5.3.1. The energy needs of the two buildings are currently served by AC power through one of the utility owned electric service transformers located on the island.



Figure 5.3.1. Location of Coconut Island and the DC Microgrid Project site.

Major project activities completed through the support of prior APRISES funding include:

- Project planning and permitting;
- Baseline energy use data metering and collection;
- Developing a conceptual design of the DC microgrid architecture to be integrated with the existing AC building infrastructure;
- Energy use and economic modeling to appropriately size a new rooftop PV system for installation on the MMRP building and a stationary battery energy storage system (BESS);
- In collaboration with the Okinawa Institute of Science and Technology and the PUES Corporation (PUES), Japan, specifying, designing, and procuring an electric E-car and E-boat and emergency power source powered by swappable BESS units charged via a swap battery charging station to be fed by the DC microgrid;

- Developing and installing two PV systems on the E-boat, one system to charge the swappable batteries on the boat and the other system to power auxiliary loads such as an onboard radio;
- Performing a due diligence assessment for potential partnering with Sion Electric Co., Ltd. (Sion Electric), a Japanese corporation with innovative DC microgrid controller technology that has been integrated with stationary BESS and DC powered lighting and air conditioning loads in the course of prior technology development work in Japan. Unfortunately, the collaboration with Sion Electric did not prove to be a feasible option for this project;
- Initiating competitive procurement of the materials and services for the MMRP building 6.2 kW rooftop PV system to serve as the primary source of renewable energy for the DC microgrid; and
- Testing and commissioning the E-Boat, including operational sea trials.

As previously noted, HNEI Grid*START* worked closely with PUES, a key collaborative research partner on this project, to adapt, improve upon, and install their swap battery charging station and associated E-car and E-boat. Figures 5.3.2 and 5.3.3 depict the installed battery charging station, portable swappable BESS units, and the commissioned E-Boat in sea trials.



Figure 5.3.2. Swap battery charging station and portable BESS units.



Figure 5.3.3. E-Boat in operation in Kāne'ohe Bay, Hawai'i.

While exploring potential partnerships in Indonesia under the ONR-funded Asia Pacific Regional Energy System Assessment (APRESA) award, HNEI staff met with the Director of the Tropical Renewable Energy Center (TREC) at the University of Indonesia. TREC has developed a prototype 2.5 kW DC-DC converter designed to serve DC loads from a 24 V bus and deployed it in a demonstration on the University of Indonesia campus. As this device had potential to fill a critical need for this project, a research collaboration was formed with TREC under APRISES15 to develop and incorporate three second generation “DCON” devices into the Coconut Island microgrid conceptual design as shown as item 5 in Figure 5.3.4. Then, after research collaboration with Sion Electric for microgrid controls development proved infeasible, HNEI developed a microgrid controller in-house. The microgrid controller will monitor the microgrid and manage the operation and power to microgrid devices, including switching the system between AC mode and DC mode to compare the respective operational efficiency of the modes.

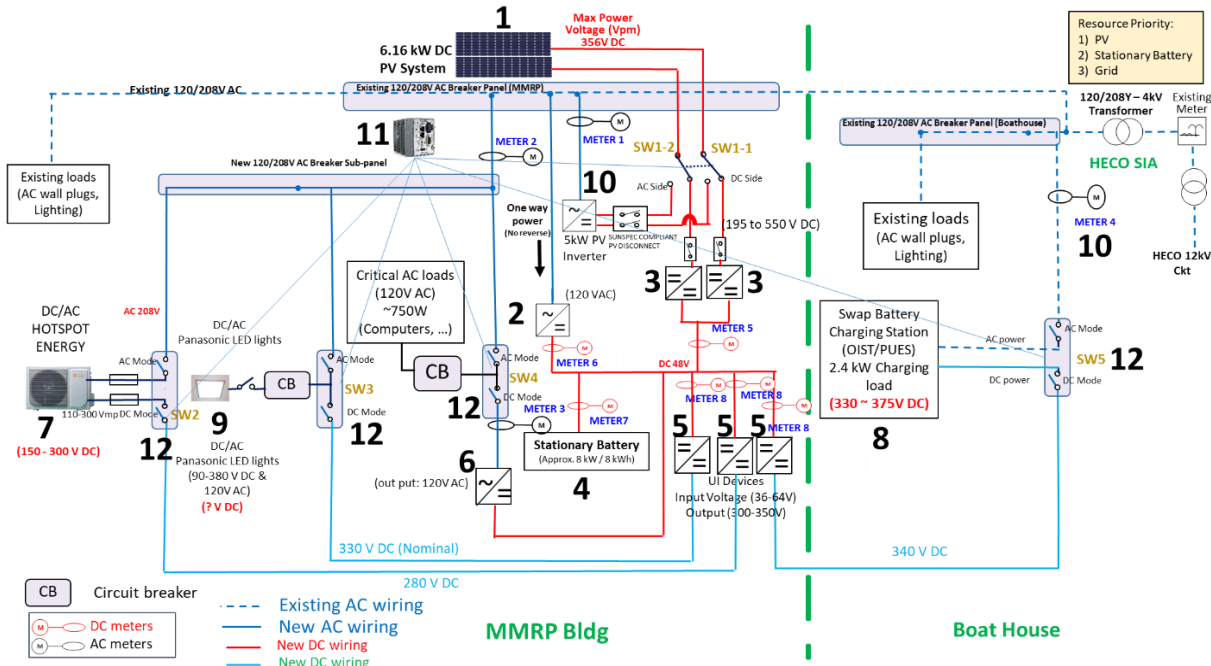


Figure 5.3.4. DC microgrid diagram with the numbered elements described below:

- PV modules installed on the MMRP rooftop as the primary source of renewable energy for the microgrid. The PV system capacity was sized at 6.16 kW DC, which will generate enough energy to support the buildings' targeted loads. PV panels were specified and designed to provide the necessary input DC voltage for effective integration with the DC microgrid controller.
- Rectifier to manage the power provided to the DC bus from the grid.
- Charge controller to manage power to the DC bus from the PV system.
- An 8 kW/8 kWh stationary BESS used to store excess PV energy produced and export the excess energy to the DC microgrid when needed to minimize the use of utility supplied power during normal operation and to maintain service to the specified critical loads in the event of utility service disruption.
- Three University of Indonesia TREC 2.5 kW "DCON" devices that manage voltage and current to power the DC loads of the microgrid from the 48V bus.
- Inverter with a capacity appropriate to supply designated critical AC end-use loads within the MMRP building served by the DC microgrid (e.g., computers, Wi-Fi network, etc.).
- An air conditioning unit that is able to operate with either a DC or AC power source. Its operating performance and efficiency under both DC and AC modes of operation will be assessed and compared.
- A swap battery charging station, designed and manufactured by PUES will charge the swappable BESS units used interchangeably in the E-boat, E-car and a portable power "suitcase battery" system. This station is capable of charging twelve (12) portable BESS units through the microgrid DC bus. The capacity of each BESS unit is rated at 1.4 kW and 1.4 kWh.
- Interior LED lighting for the MMRP building that will be modified to allow operation with either a DC or AC power source.
- AC and DC metering for performance data capture and analysis.
- Microgrid controller that monitors and controls the operation of the microgrid.
- Contactor switches to control the mode of operation (AC or DC) of the microgrid.

With this updated conceptual design completed, an Electrical Engineering firm was commissioned to work with HNEI Grid**START**'s design team to develop the detailed electrical design drawings necessary for an electrician to install the microgrid components. The detailed electrical drawings were completed to a near final form under APRISES15 funding.

Additionally, a 6.16 kW DC rooftop PV system (Figure 5.3.5) was procured, installed, and commissioned on the MMRP building under APRISES15 funding. The PV system is currently tied to the AC power system and will be utilized in the DC microgrid when operational. Other components that were identified and purchased include components for the in-house built microgrid controller, the 8 kW/8 kWh stationary battery system, the dual powered (AC and DC) air conditioner, and the contactors and switches used to control the system.

Under future APRISES funding, HNEI Grid**START** will install and commission the DC microgrid system now that the purchase of the major system components has been completed. This will enable HNEI to move into the testing, development, and evaluation phases of the research. HNEI will monitor, characterize, and identify the performance, energy efficiency benefits, and limitations of DC operation in comparison to legacy AC supply of loads, and analyze the sustainability and resiliency benefits associated with the renewable energy powered DC microgrid operation and integrated electrified transportation alternatives.

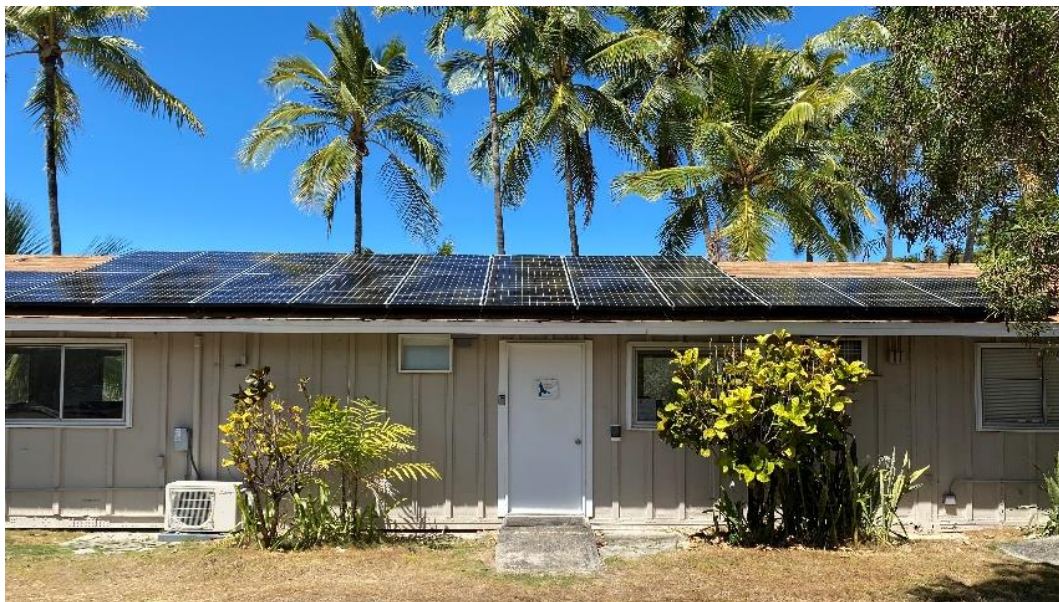


Figure 5.3.5. PV system installed on the MMRP building.

5.4 Bi-Directional EV Charging Demonstration Project

The shift towards electric vehicles (EVs) will significantly increase electricity demand, reshape grid loads, and affect utility business models. An immense opportunity exists to leverage the potential flexibility of EVs to provide grid services through managed charging. These services can provide economic value to EV owners while potentially enhancing the grid's reliability and resiliency. However, the optimization problem is complex due to the numerous categories and variants of grid services along with factors, such as potential degradation impact on EV batteries and vehicle owner preferences and scheduling requirements.

Under this demonstration project, HNEI is developing and evaluating the performance of novel algorithms to optimize the charge/discharge of shared fleet vehicles. Project experience and results will inform the University of Hawai‘i at Mānoa (UHM) consideration of options such as the electrification of fleet vehicles, advanced car share applications, integration of distributed renewable energy resources on campus, and the optimal management of campus energy use and cost containment.

In collaboration with Hitachi Ltd. (Hitachi) and IKS Co., Ltd. (IKS) on this technology development, test, and demonstration project, HNEI GridSTART is installing two bi-directional EV chargers (Hybrid-PCS) at designated parking stalls on the campus of UHM indicated by the red rectangle in Figure 5.4.1, located adjacent to the Bachman Annex 6 building indicated by the orange rectangle. New hardware for this project includes: a new 3 phase 208Y/120V distribution panel, two 7.5 kVA single phase three wire 208Y-120/240V transformers, two 6 kVA IKS charging stations, and a control box. Figure 5.4.2 shows the installation single line diagram for the system.

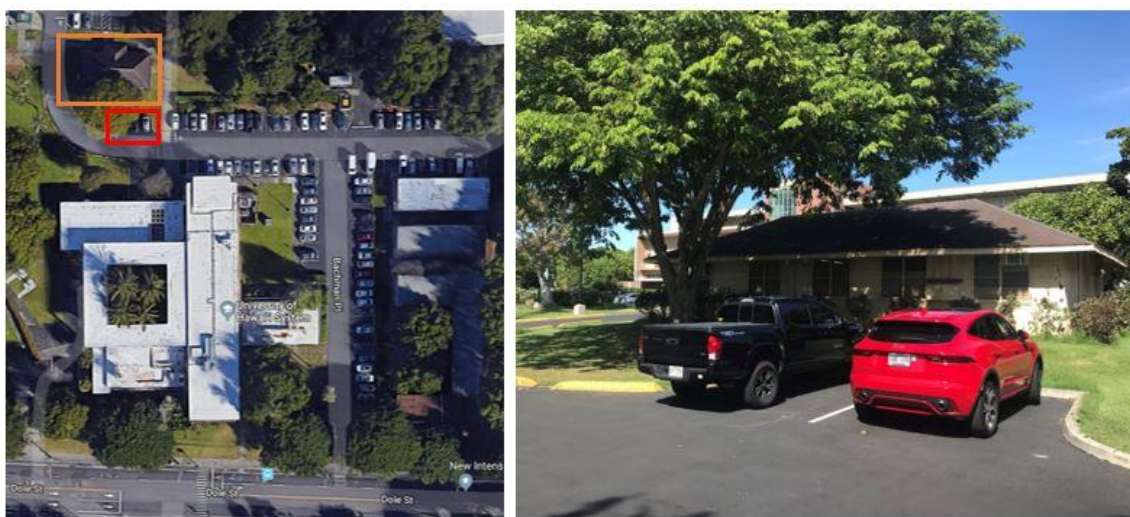


Figure 5.4.1. Location of bi-directional EV chargers on the UHM campus.

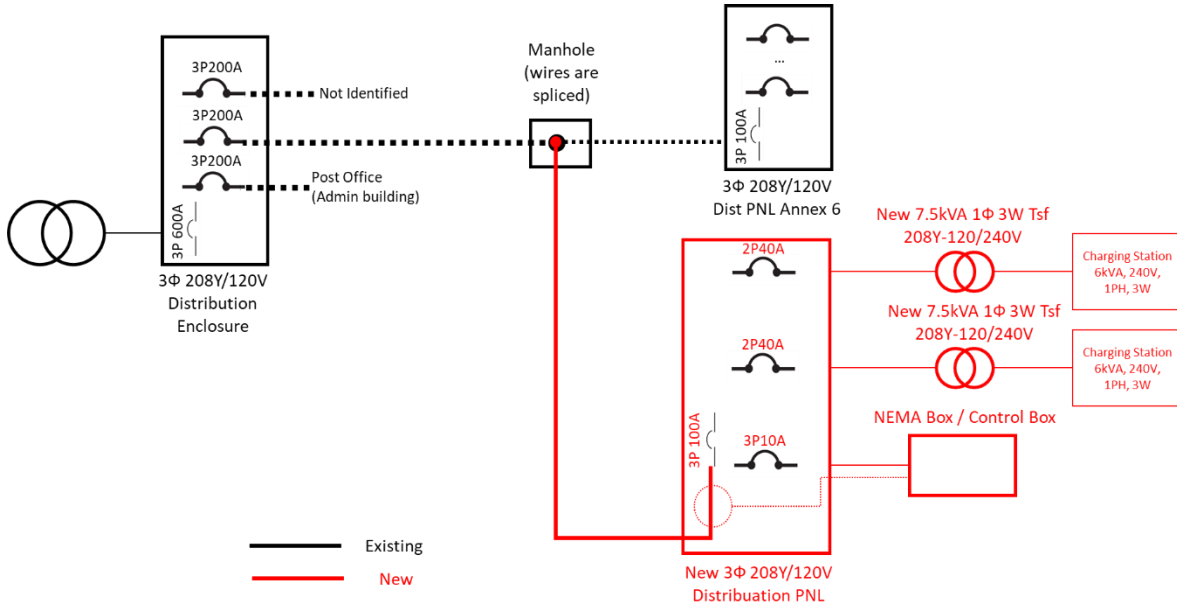


Figure 5.4.2. Installation single line diagram.

The new control algorithms will ensure that the shared vehicles for designated UH personnel are efficiently assigned and readily available for transport needs, while providing ancillary power and energy services by virtue of charging or use of the stored energy in the vehicle batteries to benefit both the customer (UHM) and possibly the operational needs of the local grid operator (Hawaiian Electric Company, Inc.).

Figure 5.4.3 delineates the overall architecture of the proposed optimized charging (OC) along with key system inputs and output.

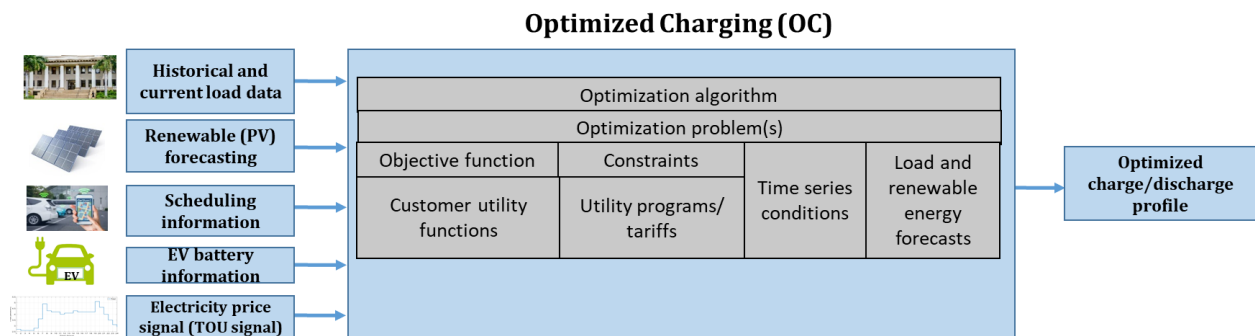


Figure 5.4.3. High-level block diagram of the OC algorithm.

Each of the key system inputs and output is described as follows:

- 1) *Historical and current load data*: a meter/controller developed by HNEI will be used to measure the load at the charging location. A machine learning (ML) based code on the

controller will use the data to forecast the gross load over a range of horizons from hours ahead to a day ahead. The forecasted load profile will be fed in to the OC algorithm.

- 2) *Renewable PV forecasting*: Under previous APPRISES funding, HNEI **T** has developed a multi-scale solar forecasting system. It is capable of monitoring irradiance in near real-time and generating PV power forecasts from minutes to days ahead based on a long-term observation database and the analysis of satellite data. This system is fully automated, generating predictions without human intervention. This solar power forecasting technique will be used to stream PV system production forecasts on the charging location. This data will be supplied to the OC algorithm on the controller as a PV forecast input.
- 3) *Scheduling information*: HNEI is developing web-based software that will help EV drivers to sign out the cars for use. The software is designed, coded, and integrated to optimize charge/discharge schedules for the EVs. Scheduling information will come from the software through a server. The scalable feature of this software will enable it to be used for a bigger fleet of cars in the future.
- 4) *EV battery information*: Chargers will read EV's battery information such as state of charge (SOC) and state of health (SOH) as soon as they are connected to the station and pass it to the controller.
- 5) *Electricity price signal*: An electricity price signal is a fixed signal which declares electricity price during different hours. This signal will be fed into the OC algorithm on the controller as an input.
- 6) *Output*: An optimized charge/discharge command will be a final output of the system.

All input information (signals) will be fed into an OC code running the main controller inside the controller box, which sits next to the charging stations. This control box, shown in Figure 5.4.4, consists of the following items: main controller, DC power supply, internet switch, modem, and antenna.

The main controller, the key hardware component of this control box, is an Advanced Real-Time Grid Energy Monitor System (ARGEMS), which was developed at HNEI under previous APPRISES funding. It is a low-cost device and system that provides enhanced situational awareness and can be programmed to work as a controller. The OC algorithm on ARGEMS at the charging station will minimize charging costs of the EV to achieve a satisfactory state-of-energy level for defined grid services. The algorithm will run once every timestep with updated inputs and forecasts for better and accurate charge/discharge commands.



Figure 5.4.4. Control box.

Additionally, a real-time simulator (OPAL-RT Technology, OP5600) is used to study the benefits of the bi-directional smart charging system and conduct system stability analysis. The real-time simulator investigates the impacts on the distribution grid of integrating bi-directionally chargeable EVs. The detailed power system model was first built using MATLAB/Simulink, then compiled in RT-LAB software. Figure 5.4.5 provides an overview of the simulation model. The control algorithm is implemented in the ARGEMS device, and the measurements and control signals are exchanged between the ARGEMS device and OPAL-RT via UDP/IP protocol.

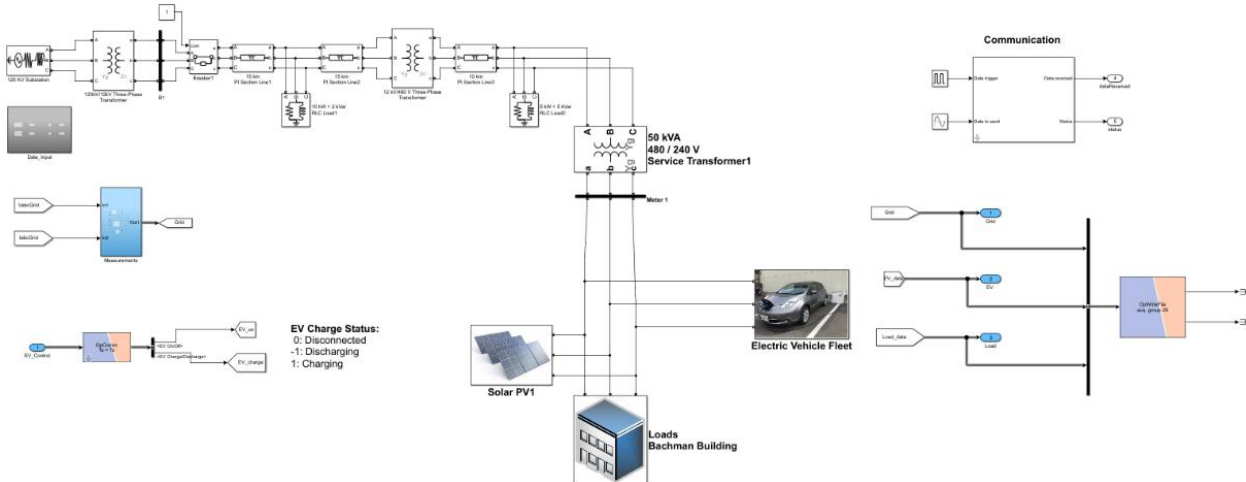


Figure 5.4.5. Overview of the simulation model.

Under future APRISES support, HNEI will install the two EV bi-directional charging stations, finalize the web scheduling software, and commission the whole control system. The performance of the proposed OC algorithm will undergo field test, evaluation, and enhancements, with operational results compared with modeled simulations across a range of use case applications and scenarios.

5.5 Hawai'i BESS + PV Virtual Power Plant Demonstration

The objective of this project is to analyze the tradeoffs and demonstrate the economic dispatch of numerous customer- and utility-side energy/power services from multiple combined behind-the-meter (BTM) battery energy storage system plus photovoltaic (BESS + PV) units. Each BESS + PV unit is small—designed to support a single family residence (several kilowatts, kW)—but at large numbers, these units could produce power that is comparable to traditional power plants (typically tens or even hundreds of megawatts, MW). At this scale, the system of systems is called a virtual power plant (VPP) because it relies on communications and software to alter the power production of physical assets that may already exist—in this case residential-scale BESS + PV units. This project is expected to provide important insights into the functional/economic trade-offs in VPP dispatch of BESS + PV resources that can help outline and quantify the business case for VPPs, including the value proposition for customer participation in a VPP and utility utilization of the same.

The main challenge lies in the coordination of the physical assets in a manner that is economic and reliable. There are numerous stakeholders in the economic optimization including the BESS + PV owner, the electric customer, the VPP aggregator/operator, and the utility. For the sake of simplicity, we assume the BESS + PV owner is the electric customer and the VPP aggregator/operator passes profits directly between the utility and customers (i.e., takes a negligible profit) and acts on the behalf of the utility to procure and pay for services. Thus, we consider only two agents or sides of the interaction: the customer side and the utility or grid side. Each agent has its own interests in using the BESS + PV to perform certain functions or services, and the utility must pay for services that require resources that the customer would otherwise use for his/her own immediate interests.

Numerous types and variants of services can be considered, and many of these were summarized under APRISES14. On the customer side, these are consumer bill savings by addressing or leveraging time of use (TOU) pricing, import/export differentials, and peak demand charges, and backup power for critical loads during grid outages. At the distribution level of the grid side, the services include peak power reduction to alleviate stress on distribution grid equipment, thus deferring costly upgrades. The peak power can be in the forward direction due to loads or in the reverse direction due to generation such as BTM PV, but regardless it can exceed the thermal limits of transformers, lines, and other equipment unless mitigated. This solution is also called “non-wires alternatives”. At the bulk level of the grid, the services include dispatchable firm capacity,) bulk power energy shifting, PV firming through end of day ramping control, and replacement reserves to protect against contingency events.

In the simplest of cases, these services could be considered to have prioritization levels such that they can be stacked or layered. However, the prioritization becomes unclear as more services are considered, and the value and need for each service may depend on various time-varying

conditions at the BTM or grid level. Thus, it would be helpful to perform a co-optimization of the services periodically during operation. In general, optimization problems are cast as a cost function to minimize (or value function to maximize) and a set of constraints. The cost function typically encapsulates multiple competing objectives as additive terms. In the case of a BESS + PV unit, these terms correspond to cost or value streams associated with the customer bill reduction and grid services. In some cases, the monetary value is clear and direct (such as for factors in the calculation of a customer's electric bill) and in other cases it may be indirect or even subjective (such as the customer value of backup power, which depends on risk tolerance). The optimization problem is paired with an optimization method or solver as an optimization algorithm. Each iteration of the optimization algorithm provides an expected optimal charge/discharge trajectory for the BESS which depends on the expected load, PV production, and other parameters up to some horizon in the future. The first step of the trajectory is executed by dispatching the BESS, and the optimization is repeated.

In this project, HNEI is utilizing up to six (four currently operating) Sunverge Solar Integration System (SIS) distributed BESS + PV units (each with a 5 kW/12.3 kWh battery and 2.5 kW PV), which were acquired at no direct cost from the New and Industrial Technology Development Organization (NEDO) of Japan. These were previously installed at the business office of Haleakala Solar (220 Lalo St, Kahului, HI) under the NEDO-funded JUMPSmart Maui (JSM) smart grid project. Originally, the project was also intended to include up to three additional older Sunverge SIS BESS units owned by Maui Electric Company, Ltd. (MECO) and installed at its Kahului base yard, but this is no longer possible due to the extended age and condition of those units.

Under APRISES14, a new electrical service was installed to connect the SIS BESS units at the Haleakala Solar location to the MECO power system and loads at the location were also transferred to the new service. All required county permits were obtained, after a few significant delays, and a conditional approval for the connection of the SIS BESS systems was obtained from MECO. Also, progress was made on defining the valuation methods and data needs, telemetry, collection and warehousing for data required to assess the customer and utility use cases.

Under APRISES15, final site and equipment inspection was completed by MECO. It was found that battery remediation work was required to bring the SIS units into operation, and this was completed for four of the six units (with the intention to leave two offline to serve as back-up units for the foreseeable future). These units are connected to the Sunverge Software Platform (SSP) which has a web front end for establishing various rulesets and sequences for SIS operation. The four units are now operating with a baseline ruleset where 500 W of PV power is used to charge the batteries during the day until 95% state of charge (SOC). All excess PV power is exported to the grid. In the evening, the batteries are discharged at 500 W down to 50% SOC. Figure 5.5.1 shows the SSP's main dashboard page, where four units are online and operating according to the

baseline ruleset shown in Figure 5.5.2. So far it is unclear why the SOC ranges from approximately 1/3 to 2/3 rather than 50% to 95%. At approximately 0200 hours, the batteries exit the discharge condition and remain in standby until sunrise.

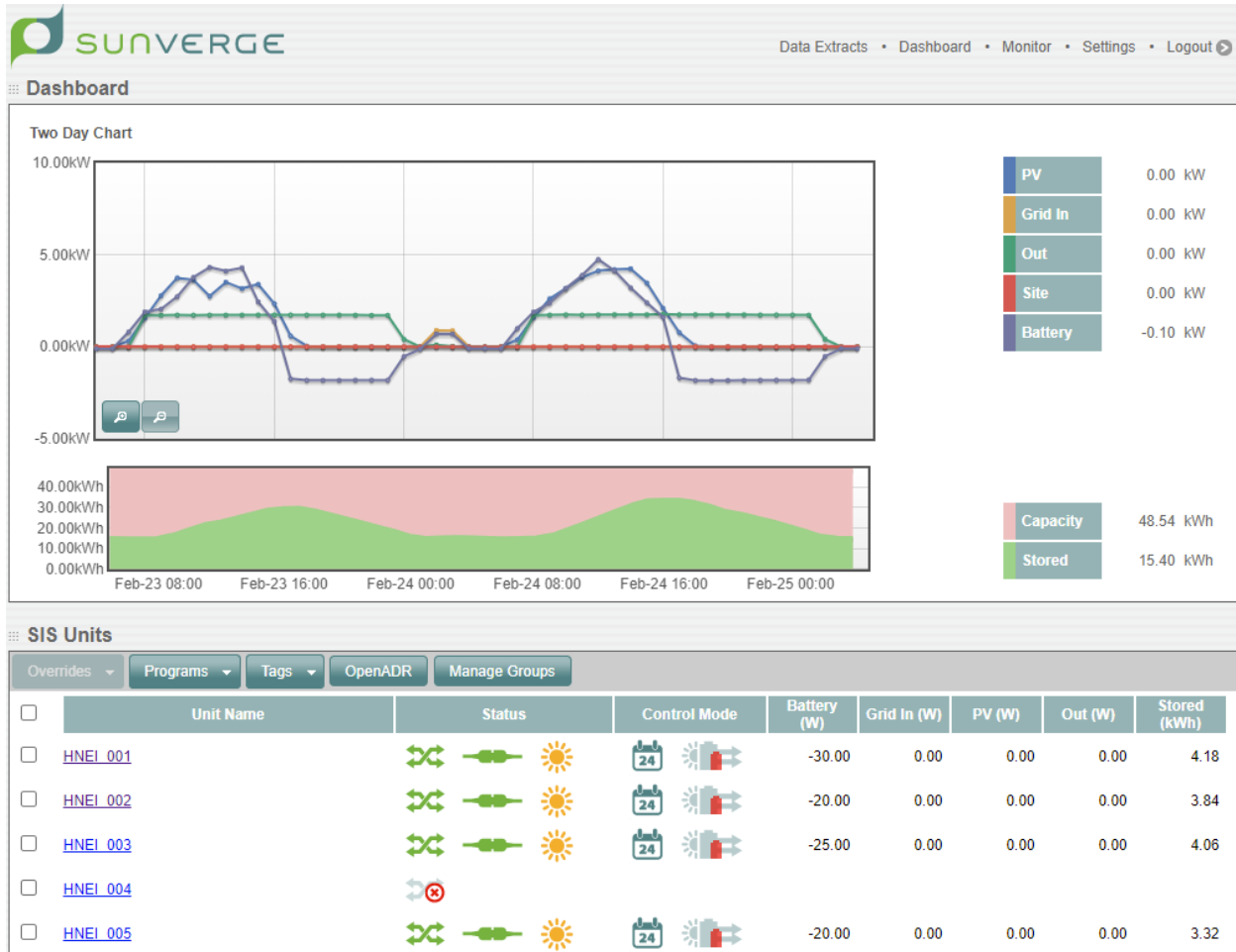


Figure 5.5.1. Dashboard of the Sunverge Software Platform (SSP).

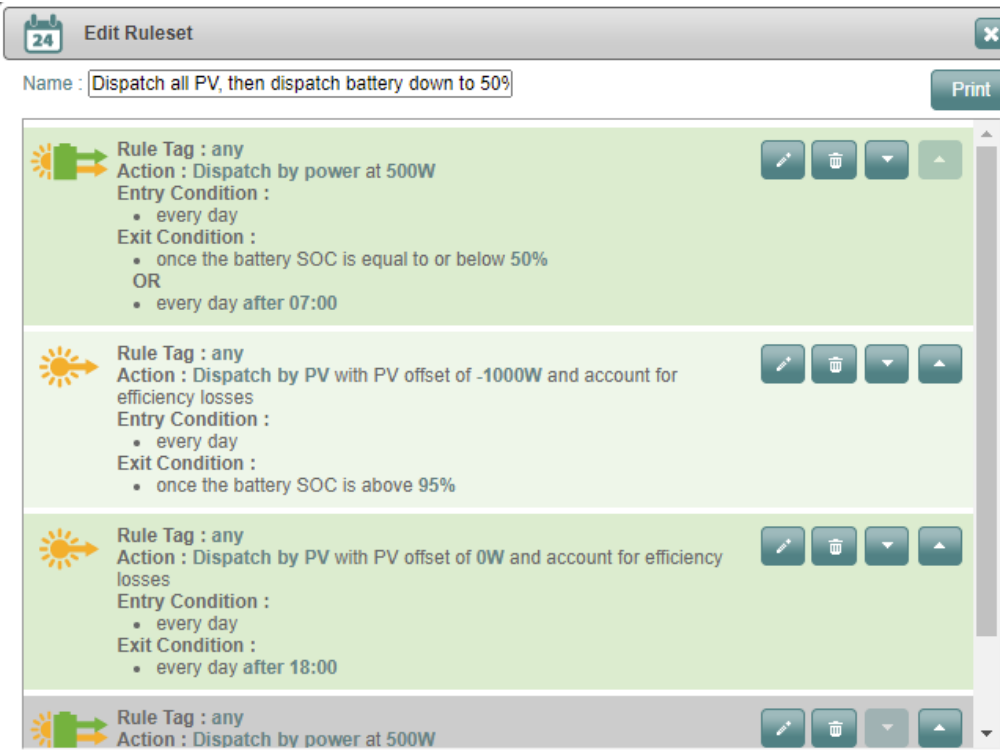


Figure 5.5.2. SSP viewer/editor for the baseline ruleset.

Although the SSP provides a powerful user interface, the rulesets represent a state machine with discrete, prescribed control conditions. This is suitable for layered or stacked customer and grid services, but it does not provide the freedom necessary to implement algorithms for full, online economic optimization. For this reason, we plan to utilize Sunverge's application programming interface (API) to allow external optimization algorithms/software to control the SIS units.

Under APRISES15, we initiated the following research approach to demonstrate and explore direct economic optimization of customer and grid services:

- (1) Create an optimization algorithm that addresses a single customer and BTM BESS + PV unit, considering both customer and grid services;
- (2) Implement the algorithm across multiple BESS + PV units as a “micro VPP” with varying load and PV profiles and backup power preferences; and
- (3) Explore the demand and supply curves of various grid services from the micro VPP by sweeping the economic parameters affecting customer reimbursement for providing grid services.

Each step will be tested in software simulation before demonstrating live control of the SIS units through the API. The research questions include:

- (1) Which customer and grid services are most synergistic, i.e. offer the best combined value proposition?

- (2) To what extent is a heuristics- or prioritization-based approach appropriate for layering or stacking services? What additional economic benefit will a full optimization provide?
- (3) What are the supply curves for VPP-based grid services from BESS + PV (while competing with customer services) under various available or proposed utility programs?

The first task is to establish the optimization problem and link it to a suitable optimization solver. This requires understanding the customer grid services from the standpoint of value streams. Figure 5.5.3 shows and objectives diagram of the optimization problem, with the high-level objective (on the left) of maximizing overall customer value by participating in the BESS + PV VPP. The fixed and variable sources of cost and revenue for customers participating their BESS + PV assets are highlighted. These are associated with customer and grid services, but in general there is not a 1:1 correspondence.

Other work is specific to the demonstration. The system architecture for the demonstration at Haleakala Solar's facility, including physical and virtual elements, is summarized in Figure 5.5.4. The ARGEMS metering box (Figure 5.5.5) has been built but not yet installed. It will independently monitor the power consumption of the four heating, ventilation, and air conditioning (HVAC) systems each comprised of a condenser and an air handler, plus the main supply to the HVAC panel. In a typical test, we plan to economically dispatch the four BESS + PV units according to those four HVAC systems which provide time-varying load profiles as inputs to the optimization algorithm.

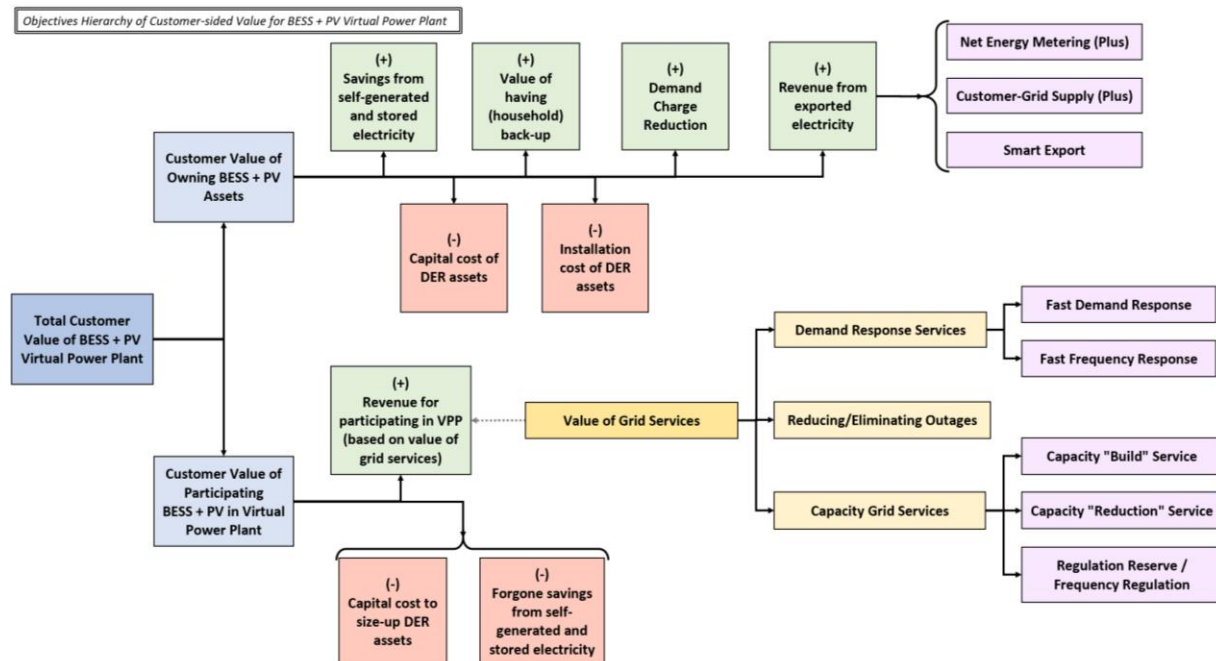


Figure 5.5.3. Objectives diagram for the economic optimization of customer and grid services.

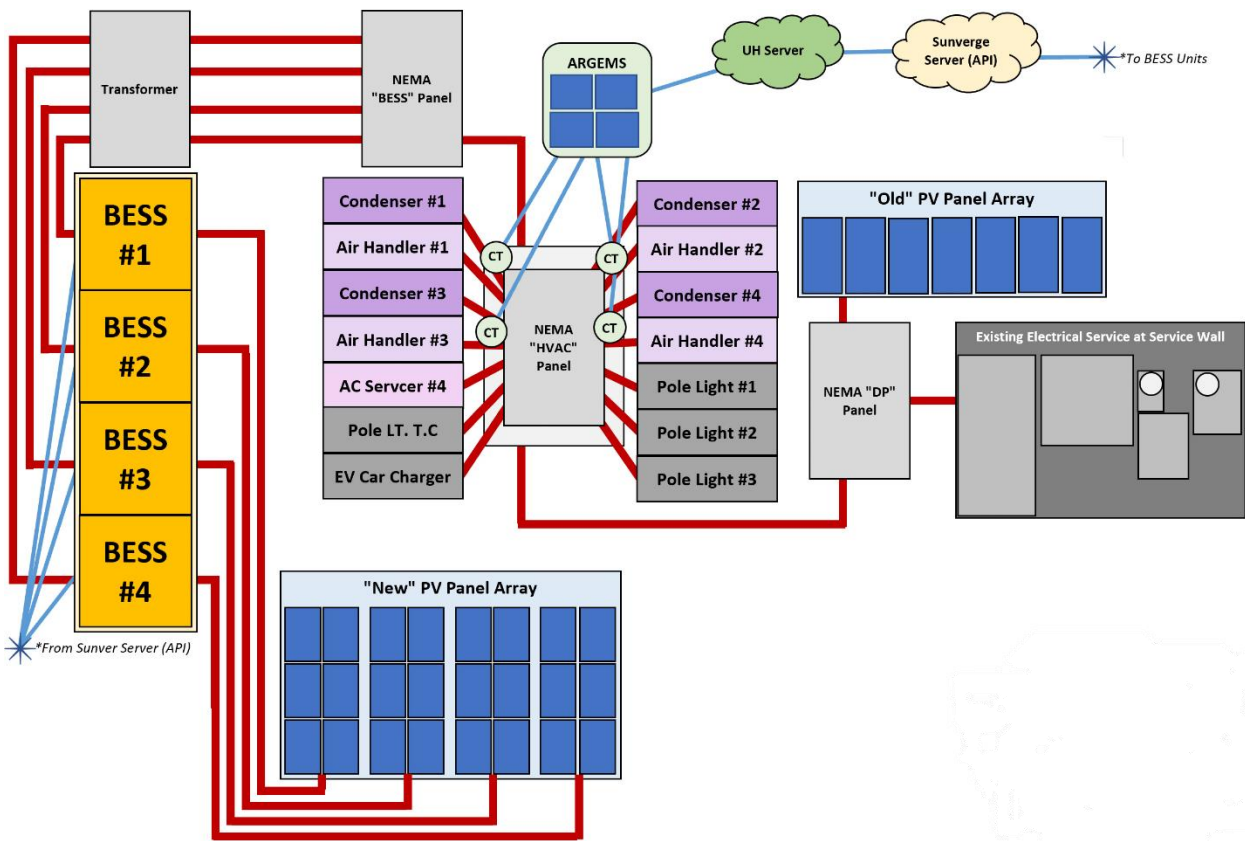


Figure 5.5.4. Power system architecture for the demonstration at Haleakala Solar.

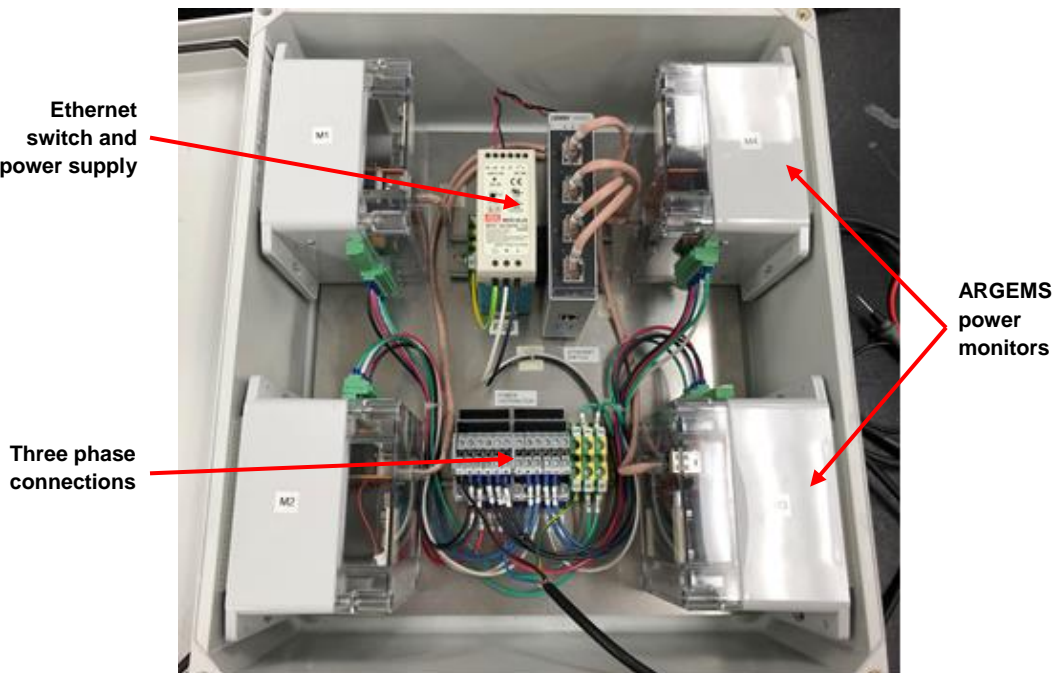


Figure 5.5.5. Real-time data acquisition box to monitor power on 11 discrete line connections.

Under future support, HNEI will continue to pursue the stated research plan. We will review progress and the services/use cases with project partners including MECO, Sunverge, and Haleakala Solar. We will pay particular attention to how the use cases and scenarios can support ongoing and evolving demand response programs and tariff structures for residential BESS + PV systems in Hawai‘i and beyond.

5.6 Power Grid Monitoring and Controls

The objective of this project is to help solve grid operational issues with high penetrations of distributed energy resources (DER) such as solar photovoltaics (PV) by offering utilities and distribution system operators (DSOs) greater situational awareness and control capabilities near the edge of the grid. Under this ongoing project, HNEI GridSTART has developed a low-cost, fully integrated, and highly flexible device and system for distributed electrical measurement, real-time analysis, and controls. It provides high-fidelity, low-latency measurement by utilizing carefully selected technology at the intersection of internet of things (IoT), RF mesh communications, open source software, single board computers, and off-the-self integrated circuits (ICs) for the power quality meter analog front end (AFE), field programmable gate array (FPGA), GPS, and power management. The device and system, called the Advanced Real-Time Grid Energy Monitor System (ARGEMS), encompasses custom board-level hardware as well as software including low-level drivers; methods to gather, report, process, store or otherwise react to measurements from the built-in power quality meter or external devices including other meters (PQube), PV inverters (SMA or Fronius), or a home energy gateway (Tesla); and a web front end for real time or historical data visualization and retrieval.

ARGEMS development, initiated under prior APRISES funding, has continued for several years and has now transitioned from conceptualization and fundamental hardware and core software development, to use cases and applications of the system involving analytics, modeling, and/or controls for in-field deployment, test and evaluation. In particular, it is currently being used in the following projects funded by APRISES15:

- *Automated Distribution Circuit PV Hosting Capacity Estimation:* Work is ongoing to use the core computer and ultimately the power measurement capabilities to model and estimate distribution power flow for in-situ PV hosting capacity analysis.
- *Real-time Health Assessment of Distribution Transformers:* The electrical/thermal transformer model has been implemented in real time, using power measurements, to estimate transformer core temperature as a stress indicator. Work is ongoing to incorporate temperature and vibration sensors in an external module for additional insight into transformer health.

- *Conservation Voltage Reduction (CVR) Demonstration*: A device is installed in Okinawa, Japan to record power measurements and control two Fronius inverters for reactive power injection according to HNEI’s CVR algorithm. This has also been an opportunity to validate its voltage readings against the well-established PQube3 commercial instrument.
- *Hawai‘i BESS + PV Virtual Power Plant Demonstration*: Four power monitors have been installed in a larger data acquisition box to measure 11 channels of power flow and implement algorithms for economic optimization of battery energy storage for numerous customer and grid services. Field deployment coordination is underway.
- *Coconut Island DC Microgrid*: The core computer (without power measurement circuitry) is retrieving and reporting DC and AC power metrics from an SMA inverter every 4 seconds.
- *GridSTART Laboratory*: The core computer (without power measurement circuitry) is retrieving and reporting AC power metrics from four Fronius inverters every 4 seconds.
- *Bi-Directional EV Charging Demonstration Project*: A device has been installed to run charge optimization algorithms and also as a field test of the hardware reliability. This project uses some of the programs and functions for data messaging, storage, and web presentation.

The ARGEMS platform is also being used in other funded projects and proposals. It was used for distributed PV inverter control for CVR under an ONR Defense University Research-to-Adoption (DURA) project led by Arizona State University (ASU), with HNEI as a sub-awardee. Under HNEI’s ONR-funded APRESA project, it is a basis for research collaboration and field deployment with Chulalongkorn University (Thailand) and a Thai distribution utility, the Provincial Electricity Authority (PEA) of Thailand. In particular, six engineers from PEA visited with HNEI for an 8-week internship in 2020 and studied three different use cases that could be implemented on the platform. HNEI recently submitted a U.S. Department of Energy (DOE) concept paper with Commonwealth Edison utility (Chicago, IL), currently under review, where the platform would be used to simultaneously gather, analyze, and report data from distribution service transformers and behind-the-meter (BTM) PV inverters to support grid operations.

The project background, original motivation, several rounds of prototype development, and web interfaces were covered in the APRISES14 final report. The project achieved the original goal of establishing a low-cost, high fidelity power monitor. Key specifications were provided in that report and remain unchanged, but a relatively minor hardware redesign was performed under APRISES15 funding to fix issues with the backup power supply and LTE modem, as well as to add an interface for a Landis+Gyr wireless mesh node and migrate to a graphic LCD display to show more information in the field. After additional improvements primarily for manufacturability, 25 devices were produced (Figure 5.6.1). Ten of these were funded by and delivered to ASU’s DURA project. Most of the printed circuit board (PCB) manufacturing and

assembly was performed by MacroFab, Inc. (Houston, TX); this was the first time the production was outsourced to industry.



Figure 5.6.1. Devices prior to shipping for external research collaboration.

Under APRISES15, software development was performed to demonstrate AC waveform capture. This work was featured in an UH Department of Electrical Engineering undergraduate's senior capstone project. The device was able to capture 128 samples per line cycle and report it to a webpage at approximately six times per second. A snapshot is shown in Figure 5.6.2, where the device captured harmonics in the operation of a desktop AC fan. These were subsequently verified on an oscilloscope.

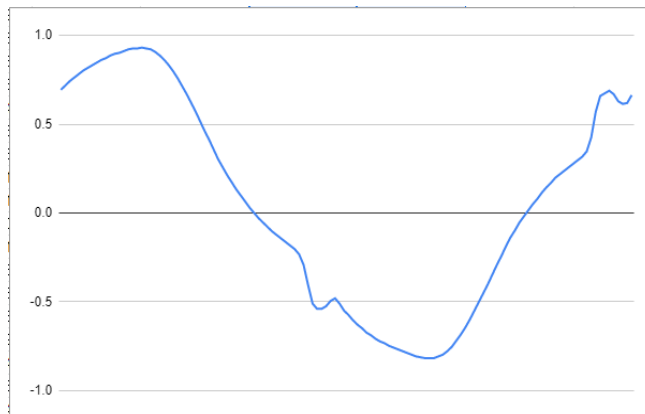


Figure 5.6.2. Current waveform of a desktop AC fan measured by the ARGEMS device.

To enable more convenient and intuitive signal analysis for the waveform capture and other projects including real-time web-based visualization, some routines were implemented in Node-RED. This is a well-supported and documented open source JavaScript-based platform that provides a visual, block-based interface for signal input, processing, and output. An example is shown in Figure 5.6.3.

Also funded under APRISES15, ARGEMS software modules were added to gather data from SMA inverters and the Tesla Energy Gateway 2.

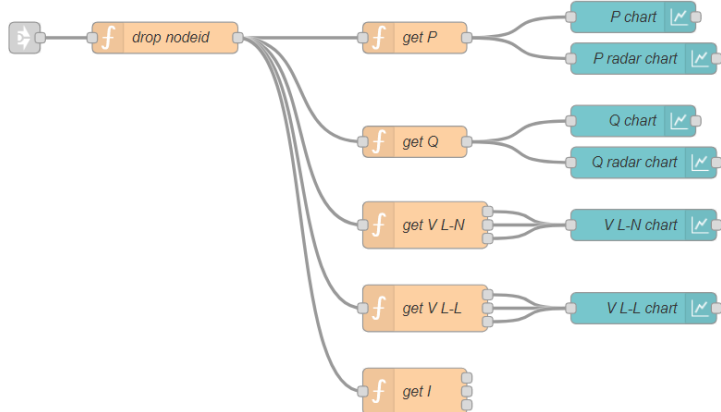


Figure 5.6.3. Diagram of signal routing and visualization routine implemented in Node-RED.

Under APRISES15 funding, the device was featured in ThinkTech Hawai‘i, SOEST Open House, and UH Sea Grant’s Voices of the Sea. The initial review of the U.S. patent application (filed November 22, 2018) was completed and work will be initiated soon to resolve the claims.

Prospective future work, if funding allows, may include a small demonstration with the Hawaiian Electric Company (HECO). Work is required to further evaluate and enhance the cybersecurity of the system. Also, some earlier ideas for time-synchronized harmonic data capture were recently related to another active area of power systems research, and this could be explored.

5.7 Real-Time Health Assessment of Distribution Transformers

This research project was initiated under APRISES15 to assess the health of distribution (service) transformers using non-intrusive sensors, contextual or environmental data, and real-time distributed algorithms implemented on Advanced Real-Time Grid Energy Monitor System (ARGEMS). Distribution transformers can fail for many reasons including oil leakage, thermal stress due to overload, harmonics, and unbalanced loading. This has important implications to the cost and reliability of electric service. Effective methods to monitor distribution transformers’ condition and health continuously, automatically, and on site could help utilities proactively mitigate failures and degradation of the transformers. This is also particularly important with the advent of higher penetrations of distributed photovoltaic (PV) systems, electric vehicles, and other energy resources that are rapidly changing the grid’s operation, since they have the potential to introduce additional stress to distribution transformers.

In this work, HNEI Grid**START** has proposed and begun to develop an online distribution transformer health monitoring method that uses real-time energy monitoring devices. The research aims to determine the most appropriate algorithms to perform accurate, low cost in-situ

transformer health monitoring and assessment. The desired outputs from an online monitoring system include metrics representing the condition of a transformer concerning pertinent failures and degradation modes as well as an overall health index (HI). Significant deviations or rapid changes in these outputs could be used to provide advance notice of the need for maintenance (i.e., predictive maintenance), circuit reconfiguration, equipment upgrade, or replacement.

For the proposed online monitoring system, top oil temperature, vibration, transformer loading (TL), and power factor are chosen as desired parameters. Top oil temperature and vibration are estimated using dynamic models and real-time data from the energy monitoring device. Fuzzy logic is used to combine various indicators of transformer health with an overall HI. Algorithms are implemented on the host computer to analyze the distribution service transformer's operational characteristics and predict the need for maintenance, reconfiguration, upgrade or replacement.

The main components of the online monitoring system are shown in Figure 5.7.1. The system uses data from energy/power monitoring devices (e.g., ARGEMS) and presents results through a user interface (UI). The UI also provides a means to input various system parameters (e.g., transformer ratings). A flowchart for the data processing and decision-making steps is shown in Figure 5.7.2.

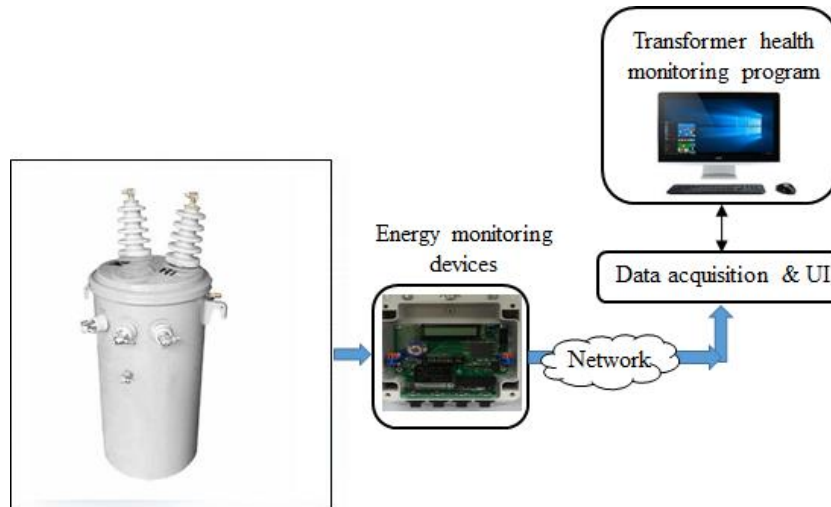


Figure 5.7.1. High-level diagram of the online transformer health monitoring system.

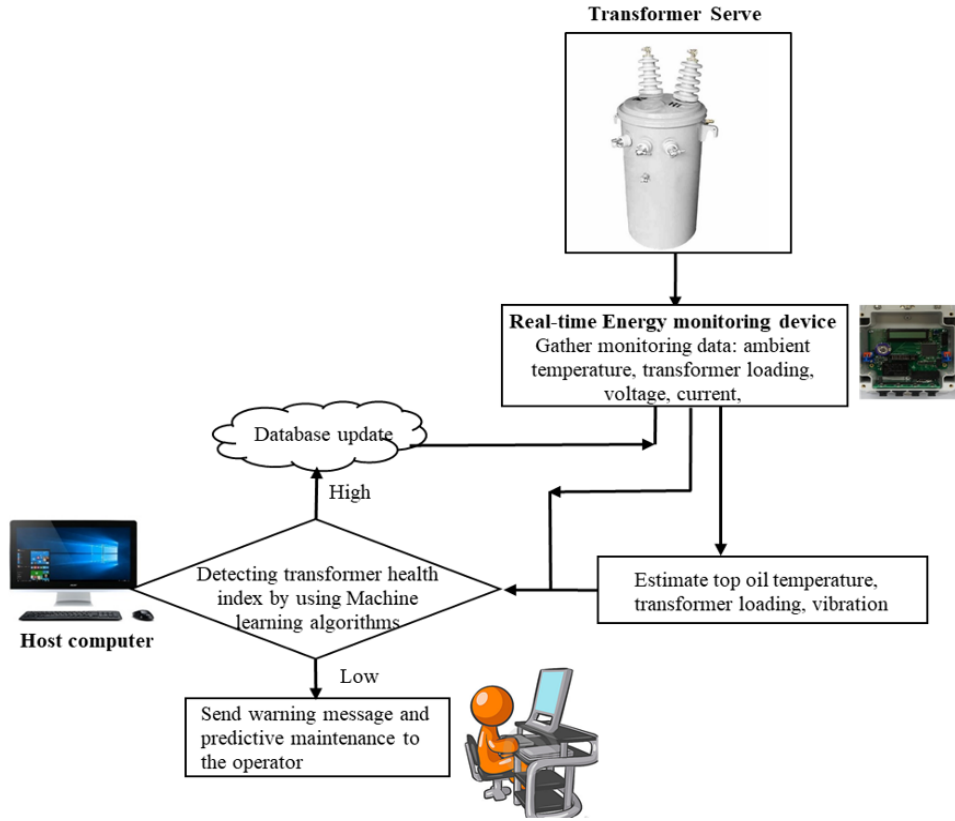


Figure 5.7.2. Flowchart of real time transformer health monitoring process.

Several techniques, such as fuzzy logic, artificial neural network, and HI calculation, were considered to process data for the assessment of transformer health. Fuzzy logic was chosen for this project because the other two candidate techniques were not suitable. Artificial neural networks are a good tool for this type of problem; however, they require a large amount of historical transformer failure data and cannot be applied to small sample datasets. Although HI calculation strongly depends on experience parameters, it cannot provide precise results as it is difficult to implement.

Fuzzy logic is applied by assigning membership functions which describe the extent to which a value of each input parameter (e.g., top oil temperature, vibration, TL, and power factor) indicates “good,” “average,” “poor,” and “very poor” transformer health. Trapezoidal and triangular curves are applied as “expert rules” over the respective ranges to describe these associations. Overall, transformer health or HI is the final output of the fuzzy inference system. The expert rules are constructed following the important order of parameters to produce the distribution transformer’s HI. The top-oil temperature is selected as the most important parameter in contributing to the transformer’s health, followed by TL, vibration, and power factor. Figure 5.7.3 provides a block diagram of the assessment process using a fuzzy logic system. The algorithms are implemented and executed in MATLAB. The limits of HI and the corresponding recommended actions are illustrated in Table 5.7.1.

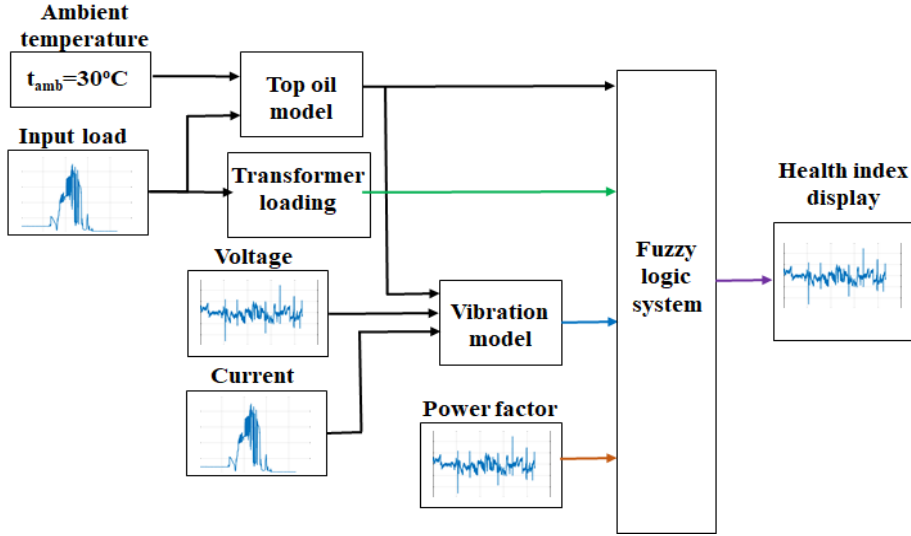


Figure 5.7.3. The model of the distribution transformer health assessment process.

Table 5.7.1. Limits of health index.

Health index range	Condition	Recommended action
$7.5 \leq HI \leq 10$	Good	Normal maintenance
$5 \leq HI \leq 7.5$	Fair	Increase diagnostic testing
$3.0 \leq HI \leq 5.0$	Poor	Start planning change request
$HI \leq 3.0$	Very poor	Immediately assess risk

The important parameters to assess the condition of the transformer (top oil temperature, vibration, TL, and power factor) are calculated or estimated locally at the transformer and sent for a final health assessment at the central server. A review of health assessment techniques for distribution transformers in smart distribution grids has been published in Applied Sciences (Tran, 2020).

A case study was carried out on a simulated 50 kVA, 7.2/0.208 kV distribution transformer to show the effectiveness of the proposed model. A real-time energy monitoring device measured the electrical conditions on the transformer in November and December of 2019.

The profile of apparent power and voltage sent from the smart meter are shown in Figures 5.7.4 and 5.7.5, respectively.

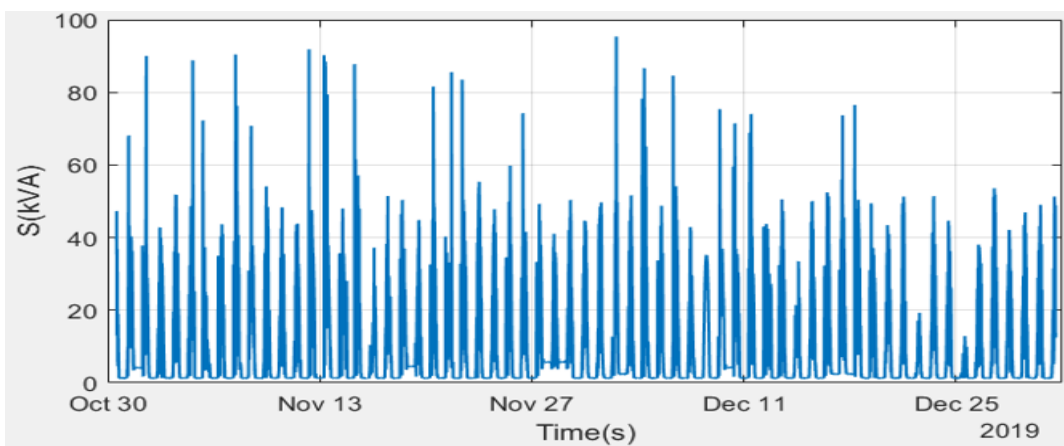


Figure 5.7.4. The profile of apparent power.

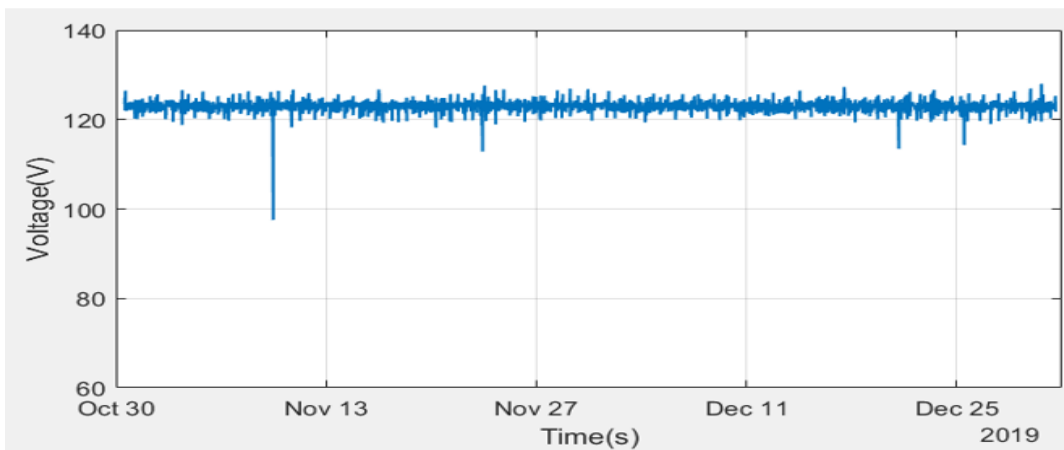


Figure 5.7.5. The voltage profile of transformer.

Figures 5.7.6 and 5.7.7 show the variation in top oil temperature and vibration indicated by the model.

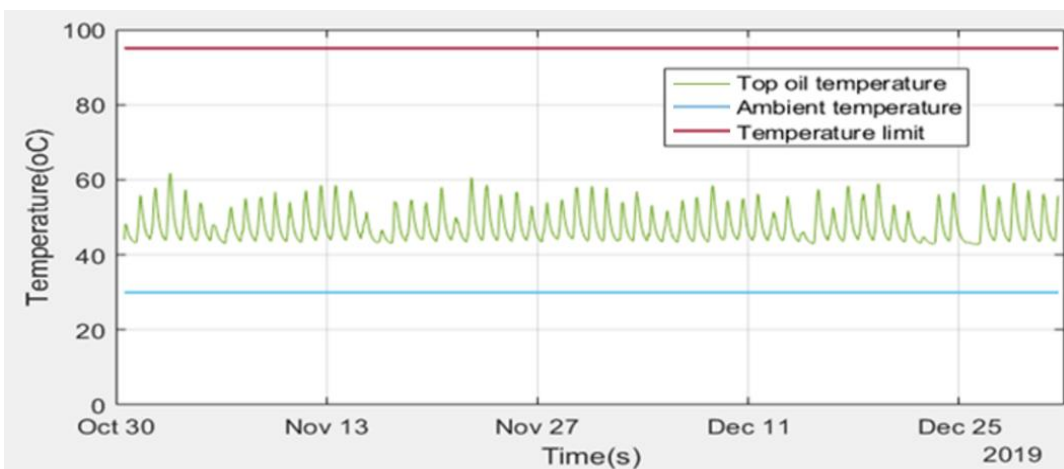


Figure 5.7.6. The top oil temperature estimation.

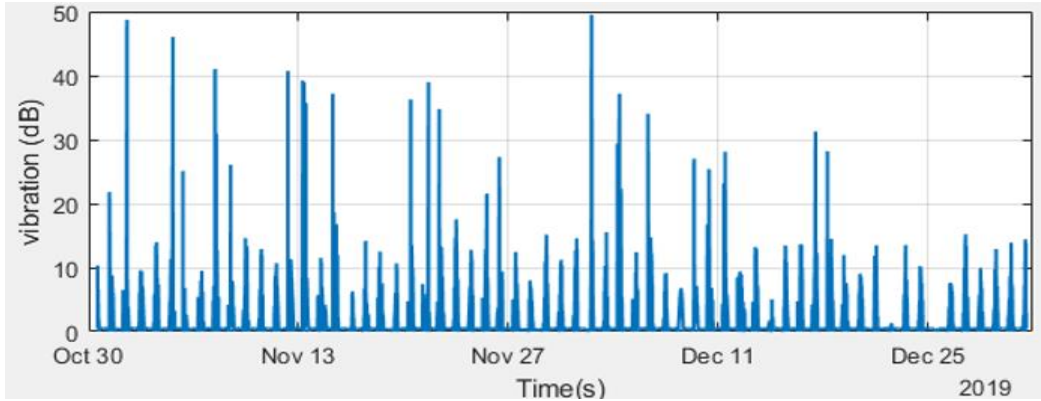


Figure 5.7.7. The vibration estimation.

The TL and power factor profile are provided in Figures 5.7.8 and 5.7.9, respectively.

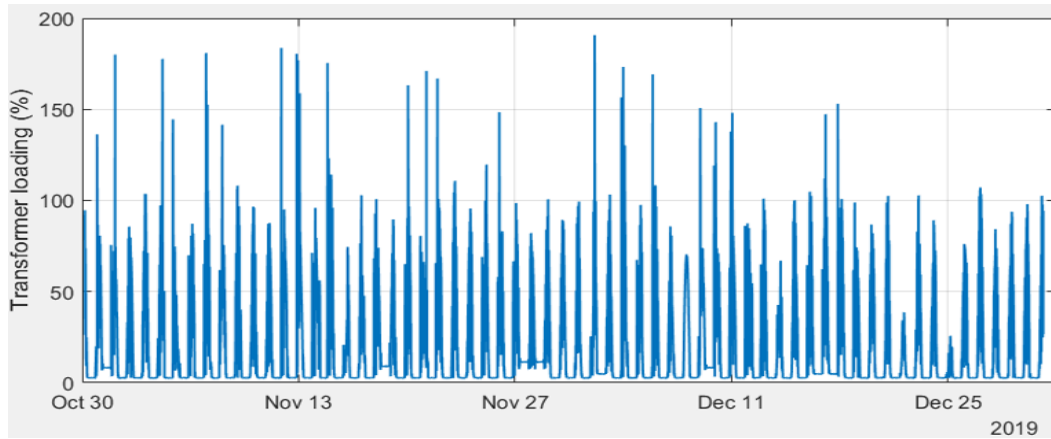


Figure 5.7.8. The transformer loading profile.

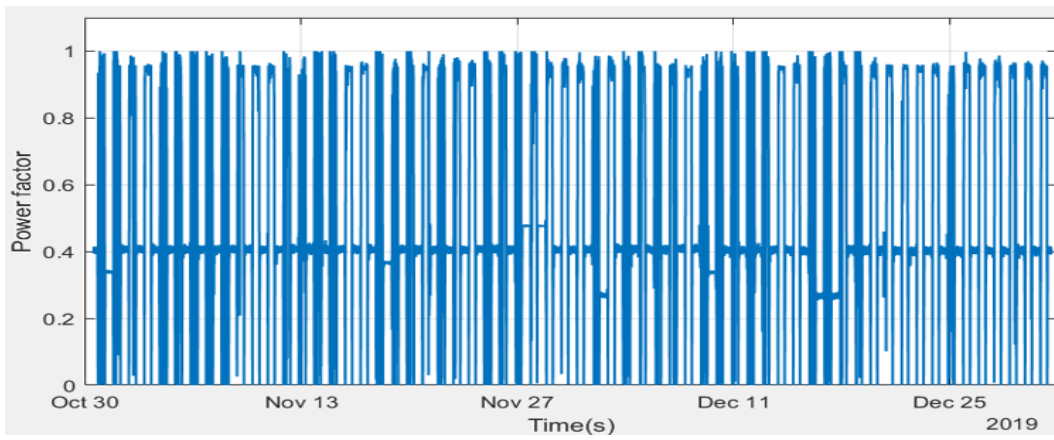


Figure 5.7.9. The power factor profile.

The HI of the distribution transformer is the final output of the system after applying the fuzzy logic. The results are shown in Figure 5.7.10.

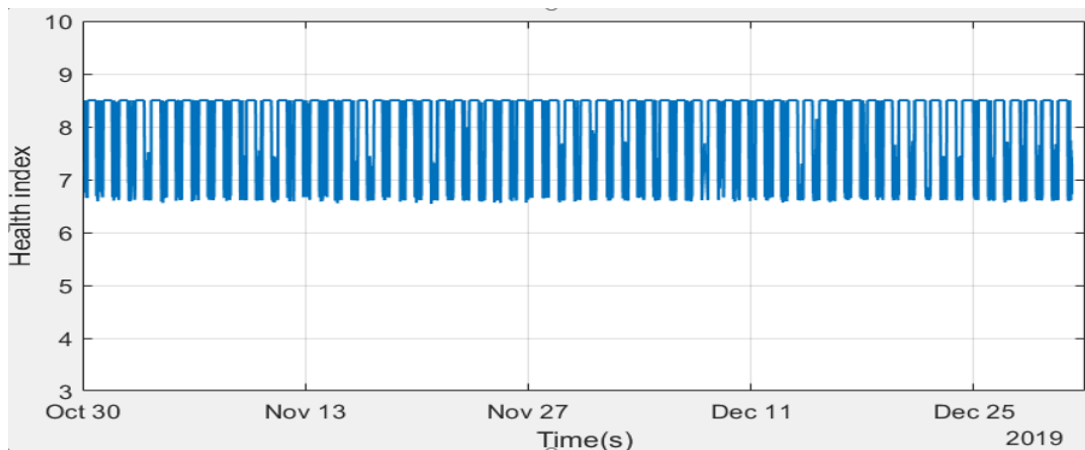


Figure 5.7.10. The estimated health index of distribution transformer.

The HI varies diurnally between 6.7 to 8.5. The results indicate that transformer maintenance is not required, but diagnostic testing should be performed to identify potential damages. In this case study, the top oil temperature and TL appear to be the most important input variables. While the maximum oil temperature is relatively stable, the value of HI can be observed to vary proportionally with the fluctuation of TL. Therefore, a transformer load adjustment plan appears necessary to avoid overload and potential breakdown.

In this research project, an online distribution transformer health monitoring method was presented. A case study on a 50 kVA distribution transformer was performed to illustrate the effectiveness of the proposed model. The proposed non-invasive method can be implemented at a low cost and with minimal disruption. In further work, this monitoring model will be applied to larger transformers and real sensors in different scenarios to analyze the sensitivity of parameters and provide the overall validation.

Publications and Presentations

Peer-Reviewed Publications

1. Tran, Q.T., Davies, K., Roose, L., Wiriyakitikun, P., Janjampop, J., Riva Sanseverino, E., and Zizzo, G. (2020). A Review of Health Assessment Techniques for Distribution Transformers in Smart Distribution Grids. *Applied Sciences*, 10(22), 8115.

Conference Proceedings and Presentations

1. Tran, Q.T., Davies, K., Roose, L. Doan, B.V., and Nguyen, N.Q. (2020). Online distribution service transformer health assessment using real-time grid energy monitor. Proceeding of the IEEE Kansas Power and Energy Conference, Manhattan, Kansas.

5.8 Automated Distribution Circuit PV Hosting Capacity Estimation

HNEI was a sub-awardee to the University of Central Florida for a previous U.S. Department of Energy (DOE) project: Sustainable Grid Platform with Enhanced System Layer and Fully Scalable Integration. The objective of that project was to meet the long-term goal of designing highly scalable technologies for distribution systems to operate reliably and securely with extremely high penetration of solar photovoltaic (PV) systems. Methods to estimate the PV hosting capacity of distribution feeders based on stochastic analysis were developed.

Building on the work of this earlier DOE project, HNEI Grid**START** has continued to advance PV hosting capacity estimation method applications under APRISES15. The inherent stochastic nature of energy production by distributed PV resources, particularly at high penetration levels, cause issues on distribution circuits (e.g., voltage limit violations, voltage flicker, and increased transformer tap actions). This research endeavors to develop an automated means to efficiently assess and determine the “hosting capacity” of each distribution circuit within a utility’s service territory. More specifically, the aim is to develop an approach to determine the maximum level of distributed PV that can be accommodated on a secondary distribution service while maintaining reliable and quality service to all customers in the context of existing infrastructure and controls. The proposed hosting capacity application will be implemented on Advanced Real-Time Grid Energy Monitor System (ARGEMS) ultimately for field installation on utility service transformers. ARGEMS will enable the application to report hosting capacity results to utility engineers and operators. Further, the capability of the application will be extended to a distributed control of PV inverters, envisioned to result in increased hosting capacity of a distribution circuit. The distributed control algorithms for the on-load tap changers and PV smart inverters will also be implemented on ARGEMS.

In this work, a case study is conducted using a feeder and data collected from a research site, the Maui Meadows residential subdivision on the island of Maui, Hawai‘i. The Maui Meadows feeder serves approximately 800 customers, and the collected load and PV data are validated. The total installed rooftop PV capacity on this feeder is approximately 2 MW, and the daytime minimum load on the feeder is 976 kW. There are 104 single-phase service transformers on this test feeder for which detailed information has been collected. A utility owned transformer load tap changer (LTC) located at the Maui Electric Company’s Wailea Substation manages the voltage at the Maui Meadows 12.47 kV feeder head-end and along the length of the entire feeder. Figure 5.8.1 depicts the Maui Meadows residential subdivision and distribution feeder serving customer loads (red circles) and grid-tied rooftop PV systems (green circles).

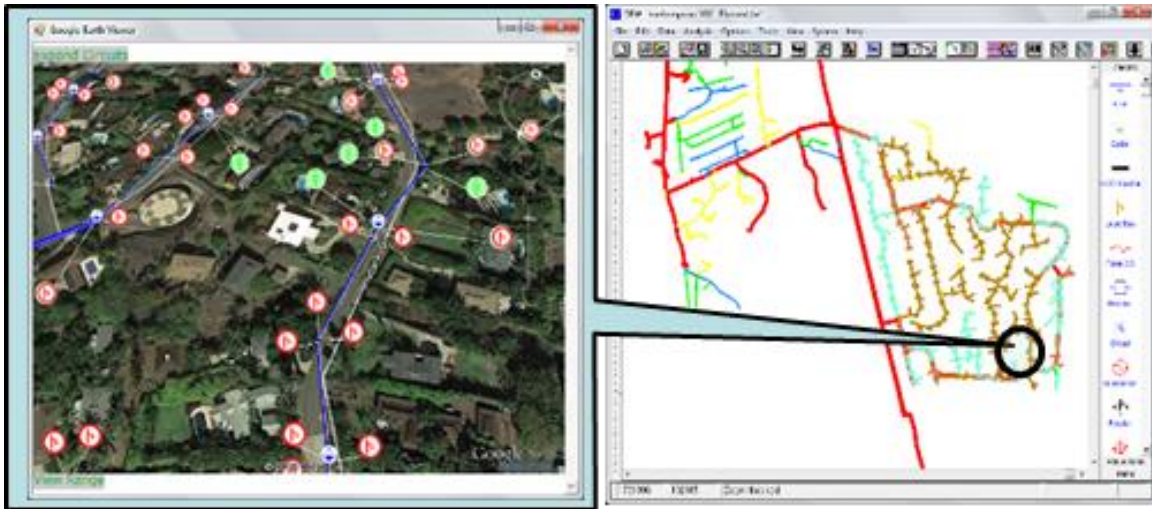


Figure 5.8.1. Maui Meadows subdivision and distribution circuit.

Pandapower, a Python based open source tool, is used in this project for distribution system modeling and optimization. In the previous DOE funded project, HNEI Grid**START** developed a conversion tool to automatically convert the model from a DEW software format to an OpenDSS software format. A full-size test feeder of the Maui Meadows residential subdivision with single-house level resolution is developed via the conversion tool. Some simulation results are shown in Figure 5.8.2.

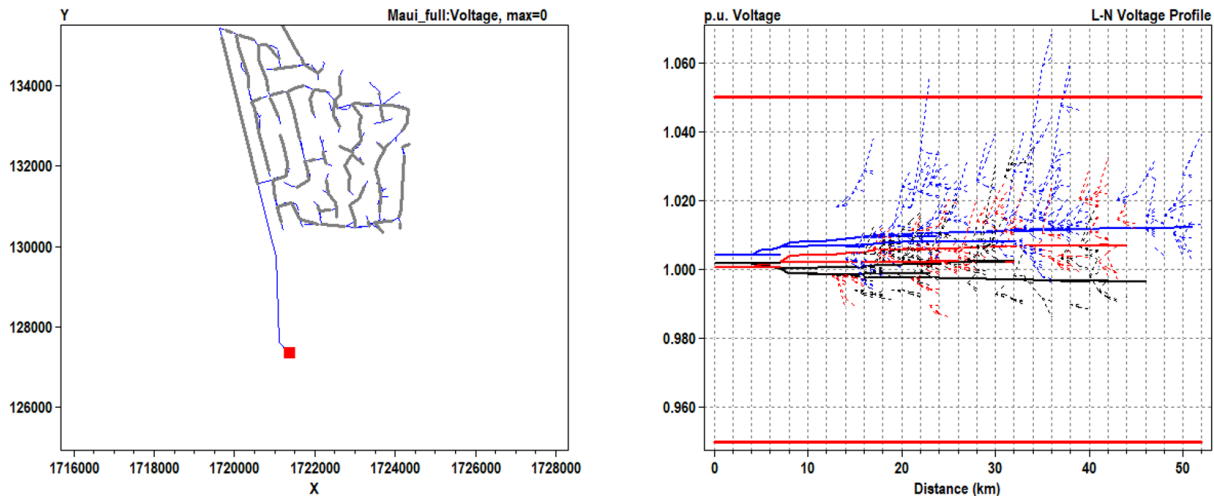


Figure 5.8.2. The topology of the Maui Meadows test feeder (left) and the bus voltage magnitudes along the feeder (right).

For the next step, a new conversion tool will be developed to convert the full-size Maui Meadows test feeder from an OpenDSS format to a pandapower software format. HNEI Grid**START** also offered a Senior Capstone Design course (EE 496) for the Spring 2021 semester at University of Hawai‘i at Mānoa, and two senior students registered for this course. In this course, the students will learn how to develop the simulation models with OpenDSS and pandapower. They will also

learn and implement the PV hosting capacity estimation method and the PV inverter control algorithm on the ARGEMS device. HNEI will mentor these two students and work together to investigate the approaches to quantify the PV hosting capacity quickly and accurately by using some techniques such as parallel computing, model decoupling, and Quasi-Monte Carlo simulation. All of the methods will be implemented in Python language so that the developed tools are expandable and portable for different operation systems.

5.9 Load and PV Synthesis

Under prior APRISES funding, methods to synthesize load and photovoltaic (PV) data based on nearby field measurements were initially developed. The overall objective of this project is to improve means to synthesize PV and load data from a limited number of field measurements in order to enable realistic distribution feeder modeling with high distributed PV penetration.

The feeder at the research site, the Maui Meadows residential subdivision on the Island of Maui, Hawai‘i, serves approximately 800 customers. The total installed rooftop PV capacity on this feeder is approximately 2 MW, and the daytime minimum load on the feeder is 976 kW. A utility owned transformer load tap changer (LTC) located at Maui Electric Company’s Wailea Substation manages the voltage at the Maui Meadows 12.47 kV feeder head-end and along the length of the entire feeder. Figure 5.9.1 depicts the Maui Meadows residential subdivision and distribution feeder serving customer loads (red circles) and grid-tied rooftop PV systems (green circles).

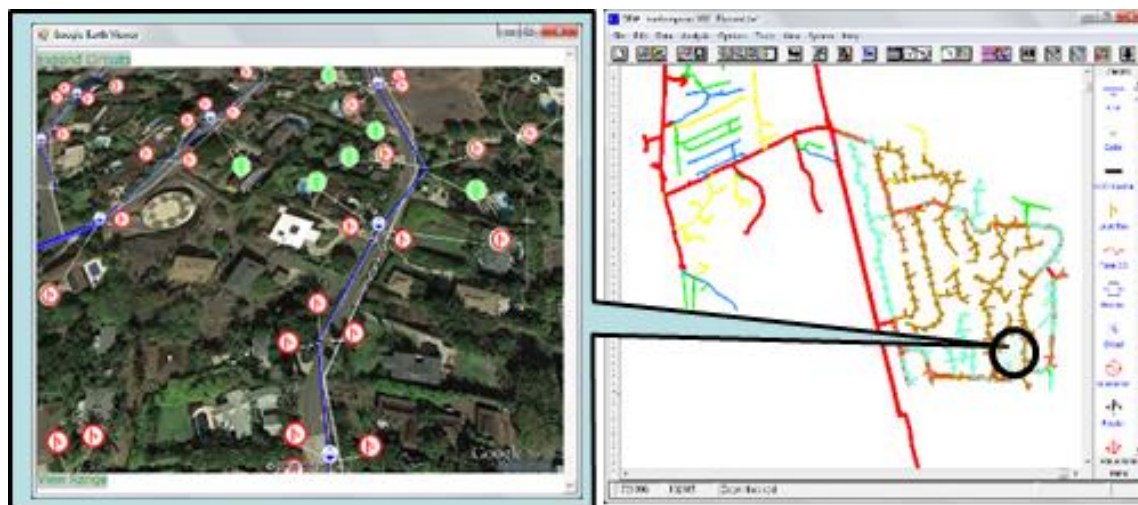


Figure 5.9.1. Maui Meadows subdivision and distribution circuit.

Under prior APRISES funding, HNEI Grid**START** developed methods that disaggregate the load and PV data to estimate the gross load data at each distribution service transformer. This allowed for the testing of distributed control algorithms that utilize the distributed resources at customer

locations located behind the meter (BTM) for various use-case scenarios. Building upon this foundational work, a data-driven method (DDM) is proposed to estimate the instantaneous output of the invisible (unmetered) rooftop PV sites with high temporal resolution, which is necessary information to gain more insights into the fluctuation of PV output. The PV output is estimated from a statistical regression model where a Minimum Redundancy Maximum Relevance (MRMR) algorithm is applied to preselect the optimal composite of the reference PV systems. The performance of the proposed method is compared with a spatial interpolation method (SIM) and a model-based method (MBM).

The basic architecture of the developed data collection system is depicted in Figure 5.9.2. With customers' permission, two meters were installed at each house: one meter recorded the gross residential load and the other meter measured the solar generation directly from the PV inverter. Each meter collected data from its location and transmitted the data to the server located at the University of Hawai'i via a local cellular network.

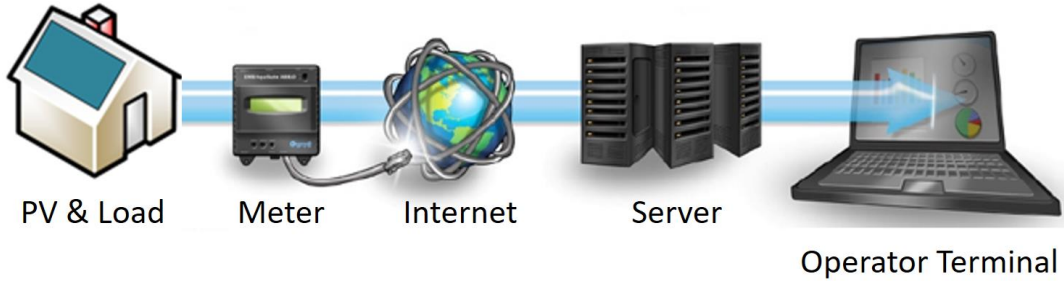


Figure 5.9.2. Overview of the data collection system.

Figure 5.9.3 is the map of the 18 meters (marked with red circles) installed at the PV inverters in the Maui Meadows neighborhood. To protect the privacy of the customers, all personally identifiable information is removed. The meter IDs are renumbered from 1 to 18.

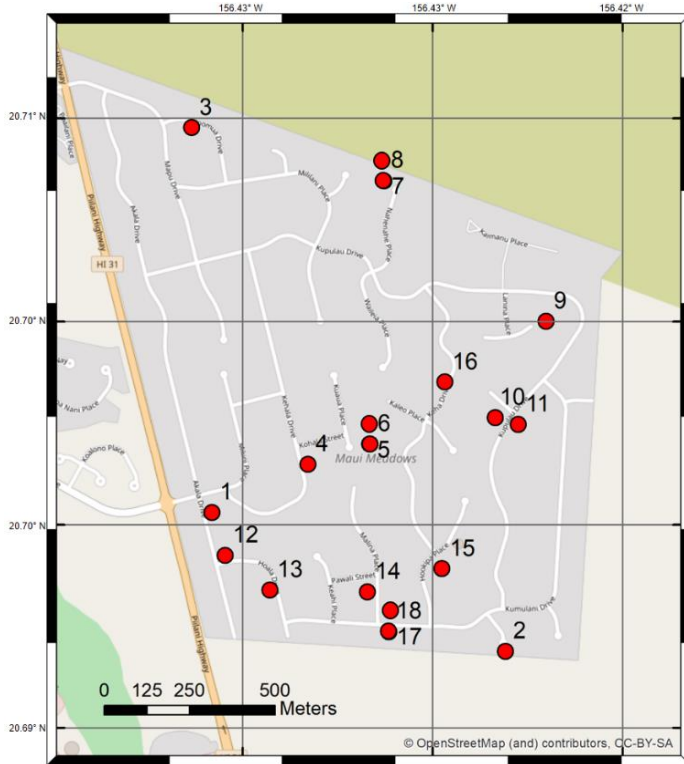


Figure 5.9.3. Map of the 18 monitored PV systems (red circles) in the region of Maui Meadows, Hawai‘i.
 (Photo credit: OpenStreetMap)

The raw records were processed to prepare a dataset because several factors, such as meter failures, PV inverter malfunctions or manually turned-off, or shadows caused by surrounding trees, can lead to anomalous measurements in the dataset. The steps to prepare a “clean dataset” from the raw records are as follows:

Step 1: Detect and delete duplicate data. If data have the same timestamp, the duplicate datum is deleted.

Step 2: Fill the missing data. If the missing timestamps are less than 60 seconds, the data are filled based on the adjacent measurements so that there are 86,400 time-points within a day. Otherwise, the PV record on this date is removed from the list of PV generation data.

Step 3: Remove the outliers. The Hampel filter is applied to eliminate the spikes while keeping the original information of the measurements.

Step 4: Check if any PV system is off or broken. The anomalous PV output and load recordings that express zeros continuously on any day are removed.

After going through these steps, the data were time-synchronized and down-sampled to once per minute using interval averages. To demonstrate the key characteristics of the clean load and PV

datasets, the load and generation profiles on two consecutive days (February 1 and 2, 2017) are shown in Figure 5.9.4 as examples.

As it can be observed from Figure 5.9.4, the shapes of the load profiles are significantly different, while the shapes of the PV generation profiles are similar. The variability of customer load is high since it is affected by customers' energy use behaviors. The peak values are decided by the capacity of the installed PV systems.

The PV output estimation algorithms are tested on a randomly selected PV system (PV site 1) with one-week data (January 7, 2017 to January 13, 2017, time period of each day from 6:00 am to 6:00 pm) as an example. The solar generation of PV site 1 is assumed to be unknown and only used in the evaluation procedure.

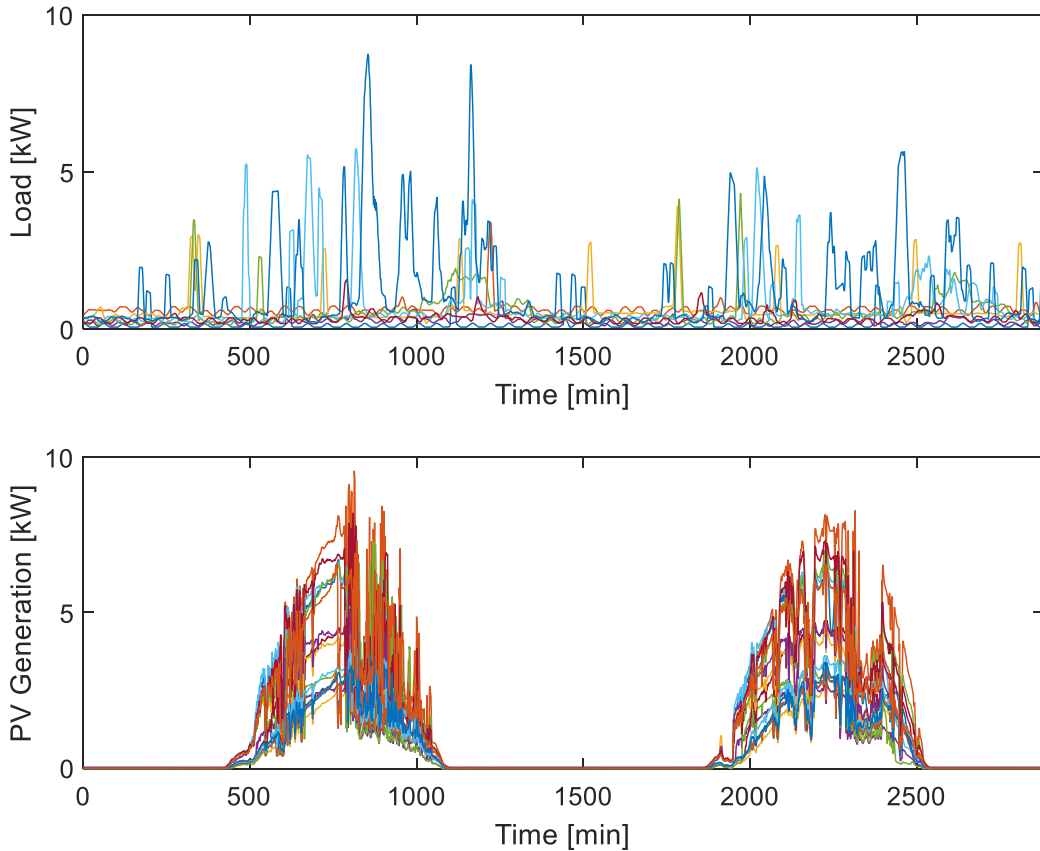


Figure 5.9.4. House load (top) and PV output (bottom) profiles on February 1, 2017 and February 2, 2017.

To quantify the performance of the three methods (DDM, SIM and MBM), the error is evaluated using the Mean Bias Error (MBE) and the Root Mean Squared Error (RMSE). The comparison of the performance metrics is summarized in Table 5.9.1, and the estimation results of these three methods are shown in Figure 5.9.5.

Table 5.9.1. Estimation of different methods' performances.

Method	MBE	RMSE	MBE%	RMSE%
DDM	-0.02	0.48	-0.85%	16.66%
SIM	0.51	0.74	17.61%	25.61%
MBM	-0.02	0.81	-0.58%	27.89%

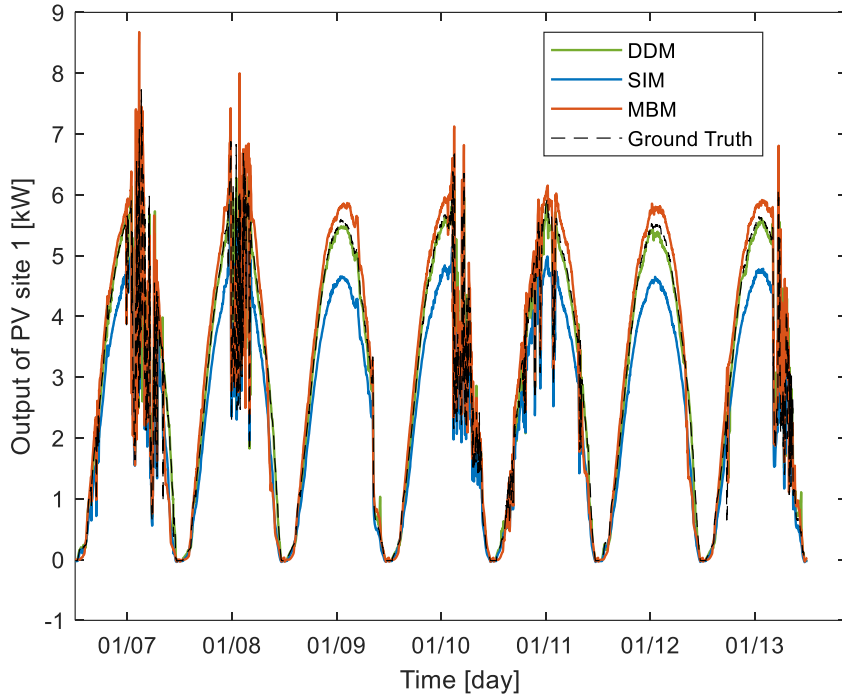


Figure 5.9.5. Estimation results of PV site 1 within a one-week period.

As depicted in Figure 5.9.5, the results show that without detailed information of the PV system, the proposed DDM can estimate the PV output with high accuracy both during sunny and cloudy days.

HNEI will continue building a detailed Maui Meadows model at the residential house level. The model and the validated synthetic data will be used in different applications and projects such as PV hosting capacity estimation, Hardware-In-the-Loop (HIL) testing, and the impacts of EVs on distribution systems.

Publications and Presentations

Conference Proceedings and Presentations

- Chen, Y., Matthews, D., Sadoyama, S., and Roose, L. (2021). A data-driven method for estimating behind-the-meter photovoltaic generation in Hawai‘i. IEEE/PES Innovative Smart Grid Technologies Conference, Held virtually, February 16-18, 2021.

2. Chen, Y., Sadoyama, S., Kobayashi, J., and Roose, L. (2020). Design and verification of a CVR scheme for distribution systems with photovoltaic penetration. IEEE/PES Transmission and Distribution Conference and Exposition, Chicago, Illinois, October 12-15, 2020.

5.10 Solar Forecasting

Power output from PV systems is directly related to the power of the sunlight striking the panel, which is measured in irradiance (W/m²). Extraterrestrial, or top of the atmosphere, irradiance varies with sun-earth geometry. Ground-level irradiance is further modulated by the absorption and scattering of sunlight by water and ice particles in clouds, fog and haze, and other particulates such as dust, ash, and smog. Complex, nonlinear processes coupled with atmospheric dynamics affect these particles, causing large and erratic fluctuations in irradiance and solar power generation. At high penetration levels, photovoltaic (PV) generation variability and the accompanying uncertainty of future PV generation can cause a range of challenging issues for electric grid operations.

The goal of this project is to develop, test, and employ solar forecasting methods and technologies. Under APRISES15 funding, HNEI Grid*START* continued development of the HNEI solar forecasting system, which combines three separate forecasting components that focus on, and are more accurate at different time and space scales (Figure 5.10.1).

- Regional, **day-ahead (DA)** forecasts are generated using numerical weather prediction (NWP) models.
- Regional, **hour-ahead (HA)** forecasts are generated using satellite image-based algorithms.
- Local, **minute-ahead (MA)** forecasts are generated using sky image-based algorithms.

Project activities under APRISES15 focused on: (1) developing probabilistic solar forecasting methodology; (2) completing a significant update to the HA forecasting component to allow for operational forecasting using GOES-17 imagery; (3) expanding the capabilities of the operational forecasting management system (OFMS); (4) developing visualization tools to show real time observations and predictions; (5) continuing development and testing of hardware and software for MA solar forecasting; and (6) continuing to expand the coverage and capabilities of a solar resource observation database for the Hawaiian Island region. Key accomplishments and details of the work conducted are described below.

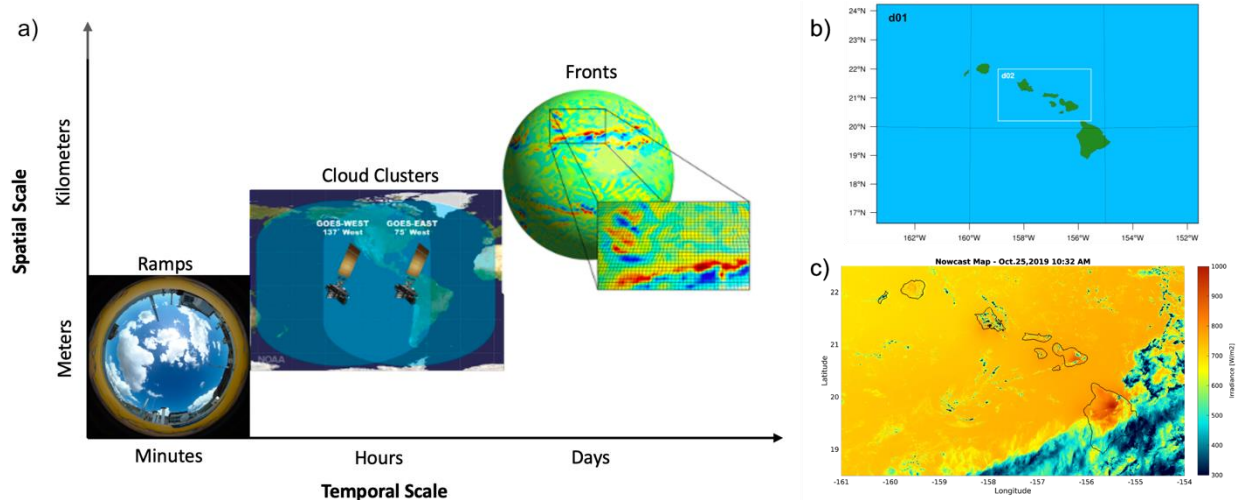


Figure 5.10.1. (a) Representation of the time and space scales covered by each forecasting component. The spatial coverage of the (b) DA and (c) HA components are also shown.

The HNEI solar forecasting system is designed to predict irradiance and PV power over a range of timescales by combining forecasts from three components (sky images, satellite images, and NWP). More accurately, the system is designed to combine multiple overlapping forecasts from each component to allow for probabilistic forecasting using ensemble methodology. In theory, the probabilistic forecast should be more accurate than any one of the individual, deterministic forecasts that it is comprised of. The probabilistic forecast will also contain information on the uncertainty of the prediction, which can act as an indicator of upcoming variability. The set of available forecasts for a particular time and space form the ensemble. The probabilistic forecast is made from the combination of ensemble members, expressed in terms of a probability distribution.

Under APRISES15, we developed methodology to efficiently generate ensembles from individual DA and HA forecasts and then generate probabilistic irradiance forecasts. We have found that the probabilistic forecasting accuracy is heavily dependent on the number of ensemble members used to generate it, as well as the forecasting horizon lengths of the ensemble members. More ensemble members with shorter forecasting horizons results in more accurate probabilistic forecasts.

Regional HA forecasts rely on observations from geostationary satellites, which provide information on regional cloud conditions. Geostationary (i.e., equatorial geosynchronous) satellites orbit above a fixed point on the Earth allowing for consistent monitoring of meteorological conditions. The National Oceanic and Atmospheric Administration (NOAA) operates two geostationary environmental satellites, GOES-East, which focuses the continental United States (positioned at 75°W), and GOES-West, which monitors the eastern Pacific Ocean (positioned at 135°W).

The HA forecasting algorithms for the Hawaiian Island region use GOES-West images. Until Spring 2019, GOES-West duties were performed by GOES-15, which released a new set of images every 15 minutes. The operational forecasting system generated a regional nowcast irradiance map and a 6-hour ahead, 15-minute resolution, regional irradiance forecast within that time. This allowed the system to generate a forecast from each set of images with minimal computation latency issues.

In the spring of 2019, GOES-West duties were assumed by GOES-17. GOES-17 is considered a next generation geostationary environmental satellite, which relative to GOES-15, produces images at twice the spatial resolution, using 10 additional spectral channels, more often. GOES-17 generates a new image set every 5 minutes. In initial tests, the increased resolution and size of GOES-17 images pushed the computation time required to generate a 6-hour ahead forecast to well over half an hour.

To reduce the computation time of the HA component software, we began looking for inefficiencies in each line of code; searching for and identifying computations not required to be run in real-time; and evaluating sequencing and data flow to optimize the process. We also took advantage of this update to add new functionality (e.g., all algorithms and functions are now region independent and can be applied to multiple domains) and new prediction methodology. The added functionality increases computation time but allows for more realistic cloud simulations.

This new prediction methodology estimates the rate of cloud generation and dissipation and utilizes that information in the forecasting process. Cloud generation and dissipation are estimated using an augmented version of the Maximum Cross-Correlation (MCC) method that we use to estimate cloud motion. The augmented MCC method is able to track cloud changes as they move. We refer to this observation as a cloud generation rate – it is the change in cloud reflectance over the time between sequential images. The methodology has proven to be able to capture small scale orographic cloud generation, as well as diurnal and regional scale cloud evolution.

We show an example cloud motion vector field along with the estimated cloud generation rate in Figure 5.10.2. The conditions shown are representative of a typical summer morning on O‘ahu. Skies are relatively clear above the island, except over the Ko‘olau mountain range, which runs along the eastern (windward) shoreline. The cloud motion vector field shows the interruption of the trade winds by O‘ahu and the resulting wake in the lee of the island as airflow is deflected by topographic steering. The cloud generation rate field shows more cloud formation relative to cloud dissipation, which is expected as a day grows warmer. Cloud formation is strongest above the southeast corner of O‘ahu and offshore of the windward side of the island. Cloud formation due to forced convection does not start at the coastline, as one might expect, but farther offshore as the airflow stacks up against the mountain range. In a tight band directly leeward of the Ko‘olau mountains, we find a region of cloud dissipation as the airflow descends. The cloud motion vector

and cloud generation rate fields offer complementary views of the interaction of airflow and topography, capturing both 2-D horizontal advection and vertical convection.

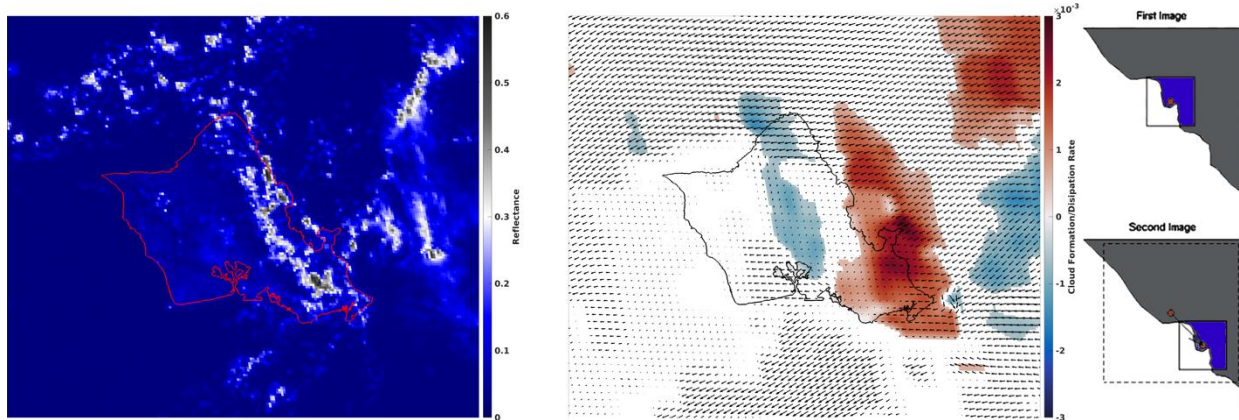


Figure 5.10.2. Cloud motion vectors and cloud generation rates are estimated from an augmented version of the Maximum Cross Correlation method (illustrated far right) applied to sequential GOES-17 reflectance images.

Future cloud conditions are predicted utilizing a finite element fluid dynamics solver, which approximates solutions to the Navier-Stokes equations to simulate atmospheric motion. In our original solver formulation, the model accounted for viscous diffusion, tracer advection (cloud properties), and self advection (the velocity field moving along itself). This formulation accurately predicted offshore cloud evolution, but often produced unrealistic results near and above the island as terrain interrupts advection and drives convection.

To improve cloud simulating capabilities near and above the island, we reformulated the solution to the Navier-Stokes equations. The formulation now includes a source term, populated by the cloud generation rates described above, and output from a neural net model (NNM). The NNM ingests a high-resolution digital elevation map and observations, including cloud reflectance, cloud top height, cloud motion vectors, and cloud generation rates, to predict orographic cloud formation. Updates to the dynamics solver also included methodology to ensure mass conservation and incorporate time-evolving horizontal boundary conditions pulled from the NWP forecasts.

The HNEI solar forecasting system is fully automated – operational forecasts are generated in real time without human intervention. Automation is controlled by a set of tools packaged as the Operational Forecast Management System (OFMS). Under APRICES15, we expanded the capabilities and responsibilities of the OFMS. It now performs the following tasks:

- Queries internal and external data sources, pulling new data as available;
- Processes, performs quality checks, and stores incoming data files, extracting regional information, if required;
- Ensures pre-dawn computations are completed;

- During daylight hours, the OFMS monitors computational resources and manages a queue of potential new jobs, optimizing computation times by controlling the start times of new processes;
- Monitors the state of the forecasting system, sending email alerts if problems are detected; and
- Transfers data to both internal and external sources.

The OFMS coupled with reduced computation time has allowed the Hawai‘i domain, operational forecasting system to run without interruption since October 2020. The system has been able to generate HA forecasts from more than 80% of GOES-17 image sets.

We have developed web-based visualization tools that show real time observations and predictions. HNEI has access to real-time irradiance observations at two test sites in Hawai‘i.

- Natural Energy Laboratory of Hawai‘i Authority (NELHA): Located on the island of Hawai‘i, the National Renewable Energy Lab (NREL) maintains a horizontal pyranometer. Observations and predictions are currently driving the web-based visualization system that is under development. Sample output from the visualization system is shown in Figure 5.10.3. Real time visualizations can be found at: <http://128.171.156.27:5100/hawaii/>
- UH Flexible Response to Ongoing Growth (FROG) Building: Located on the UH Mānoa campus on the island of O‘ahu, HNEI maintains pyranometer instruments and PV production monitoring for the FROG building PV system. Real time visualizations can be found at: <http://128.171.156.27:5100/uhfrog/>

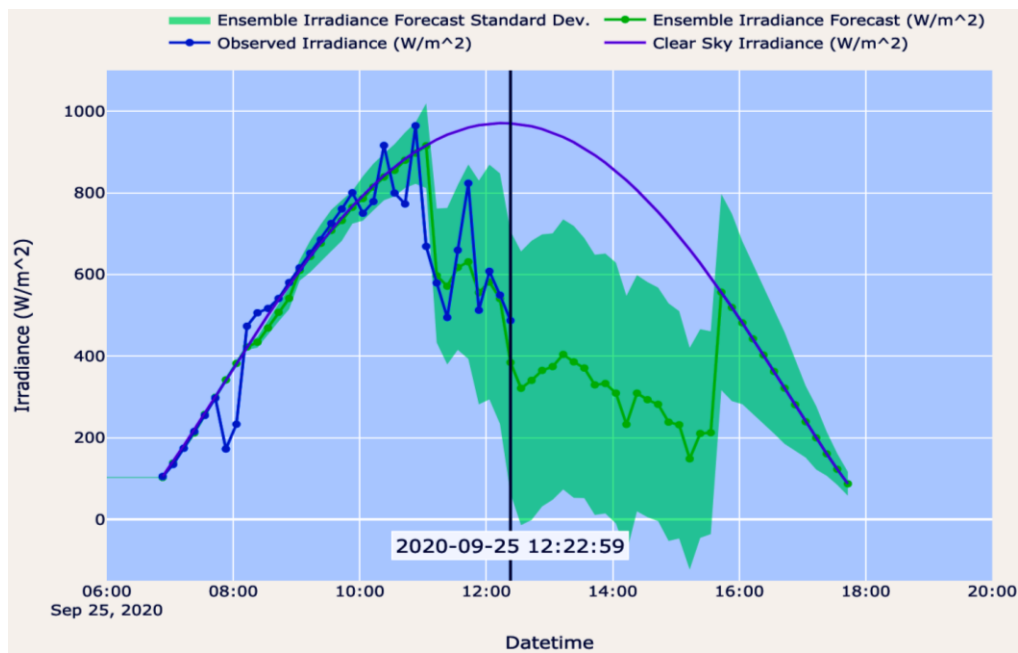


Figure 5.10.3. Sample output from the NELHA web-based visualization tool.

Under APRISES15, HNEI has continued development and testing of the Affordable High-Resolution Irradiance Prediction System (AHRIPS). AHRIPS is designed for short-term, high-resolution MA solar forecasting. The instrument directly measures solar irradiance and environment conditions; monitors sky conditions using an omnidirectional camera; and incorporates on-board computing, controls, and communications for wireless operations, self-monitoring, and edge computing functionality.

Versions 1 and 2 of AHRIPS were developed under previous APRISES funding. AHRIPS Version 1 was a minimal proof-of-concept prototype. AHRIPS Version 2 is a full product design that focuses on minimizing production costs. The Version 2 hardware limits the instrument to observation collection and communication.

AHRIPS Version 3 incorporates higher quality components for increased robustness and reliability and contains significantly more computing power. While it can act as an observation and communication platform, similar to Version 2, Version 3 is designed to operate using edge computing functionality, with forecasting capabilities at the instrument. The additional computing power of AHRIPS V3 is provided by a single board computer with quad core Intel Apollo Lake processors and 8 GB of LPDDR4 RAM. Progression of the AHRIPS instrument from Version 1 to Version 3 is shown in Figure 5.10.4.

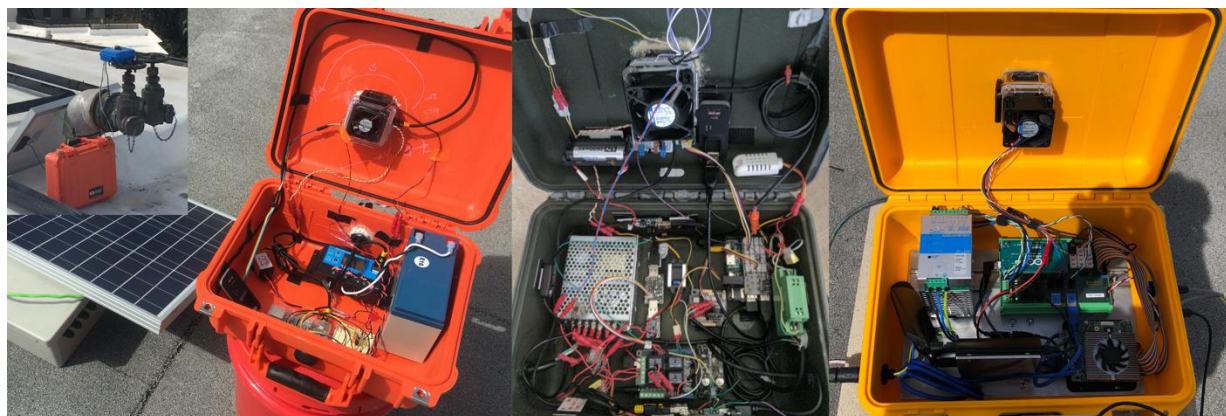


Figure 5.10.4. The progression of the AHRIPS instrument from V1 to V3.

Under APRISES15 funding, a variety of sensor-related communications issues were solved and the first AHRIPS V3 instrument was completed in October 2020. It has undergone two month-long test deployments on the roof of the Hawai‘i Institute for Geophysics (HIG) building on the UH campus. In these tests, AHRIPS V3 performed as expected.

Along with the hardware development above, HNEI also continued to develop software for AHRIPS. We have developed a new cloud mapping algorithm that varies its approach depending on cloud conditions and employs new methodology to identify and remove solar effects and sun-saturated pixels from a sky image. The cloud cover shown in a sky image is estimated using

information derived from the red, green, and blue image channels. For each pixel in that image, cloud map values indicate if that pixel is cloud containing, has clear skies, or the sky is obstructed. Figure 5.10.5 shows three example cloud maps generated at 10:09 AM on consecutive days (October 24-26, 2020). These examples present three different sky conditions, partly cloudy with the sun obstructed by clouds, partly cloudy with the sun in view, and completely overcast. These three different sky conditions trigger three different cloud mapping approaches. In response to partly cloudy skies with the sun obstructed by clouds, the algorithm identifies and removes solar effects from cloud containing pixels. In response to partly cloudy skies with the sun unobstructed by clouds, the algorithm aggressively identifies and removes all solar effects from the image. In response to overcast skies, no corrections are made. The benefits of the new methodology are most apparent in the partly cloudy skies with the sun unobstructed by clouds. Only minimal residual effects of the sun can be seen in the resulting cloud map, and the clouds just above and just below the sun in the image are correctly identified and delineated in the cloud map.

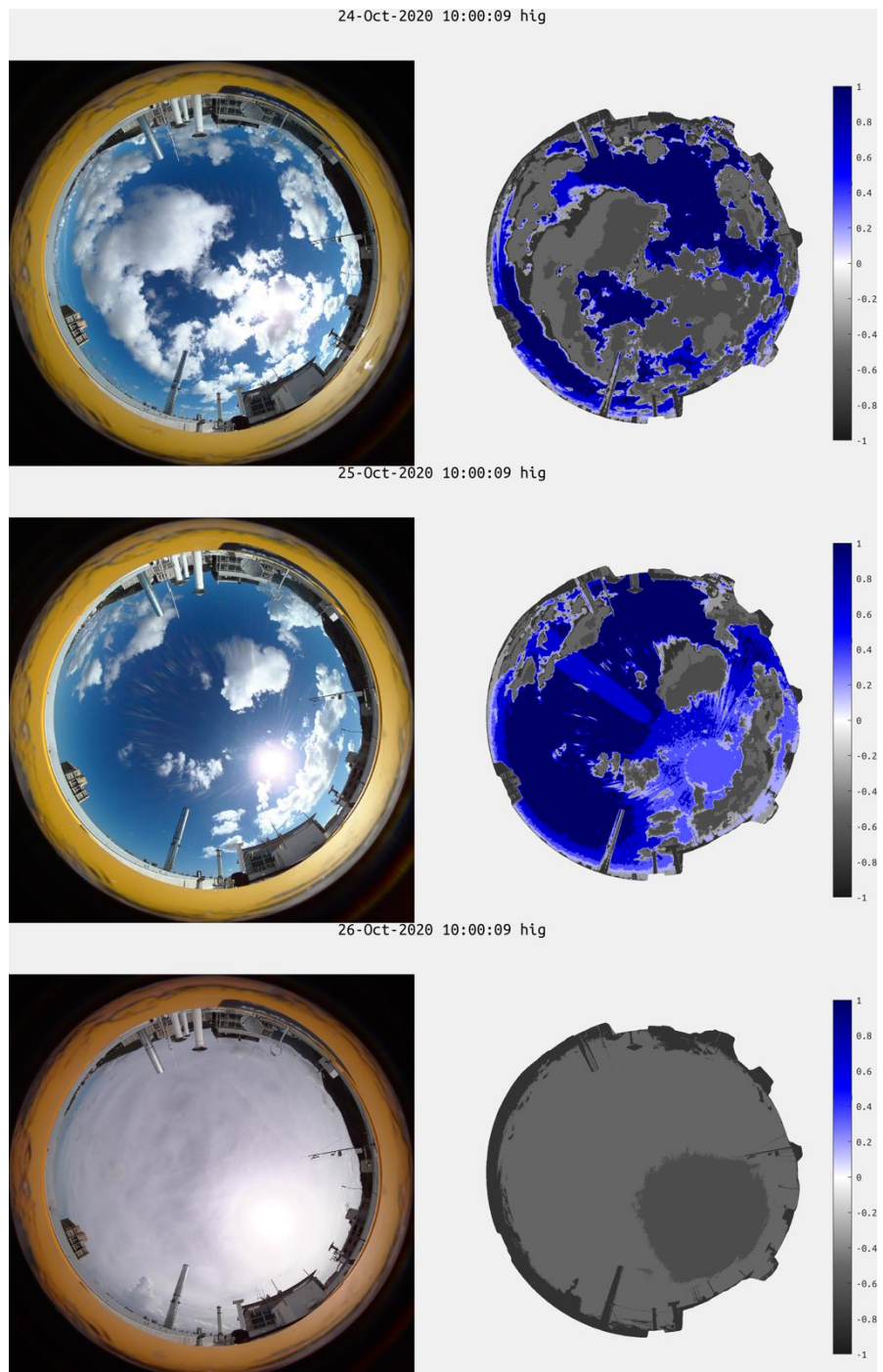


Figure 5.10.5. HNEI has developed new methodology for identifying and characterizing clouds in sky images. The method is able to better resolve cloud containing pixels near to the solar disk, while removing solar effects.

Under APRISES15 funding, HNEI has continued to expand the database of long-term irradiance and PV power observations for the Hawaiian Islands region started under previous APRISES funding. The primary purpose of this database is for solar forecasting calibration and validation. Additionally, the database has been used to develop a regional turbidity climatology for the Hawaiian Islands region, which has been shown to significantly improve the accuracy of the clear sky model used in the HNEI solar forecasting system. This database now contains over 18 years of observations of global horizontal irradiance (GHI), direct normal irradiance (DNI) and PV power output from monitored PV systems. Observations have been collected from over 60 locations on the islands of O‘ahu, Moloka‘i, Lanai, Maui and Hawai‘i. The temporal and spatial coverage of the database is shown in Figure 5.10.6.

The database employs methodology to homogenize and classify observations as either clear sky or cloud affected (using methodology based on Reno *et al.*) and, if necessary, to estimate panel or instrument orientation if unknown or questionable [1]. From these observations, we generate two main products, a clear sky index, derived from all observations including PV power, and estimates of turbidity.

The clear sky index is the ratio of the observed irradiance, or PV power, to the clear sky irradiance or clear sky power, estimated from a clear sky model and a PV system simulation tool. A clear sky index value of 0 indicates complete attenuation of solar irradiance, a value of 1 indicates clear skies, and a value over 1 indicates cloud enhancement effects. The clear sky index captures the short time scale fluctuations driven by the atmosphere.

Estimates of turbidity are generated from irradiance observations identified as clear skies. Turbidity represents the amount of attenuation of light by air molecules and suspended atmospheric particles [2]. Turbidity is required to accurately estimate clear sky radiation.

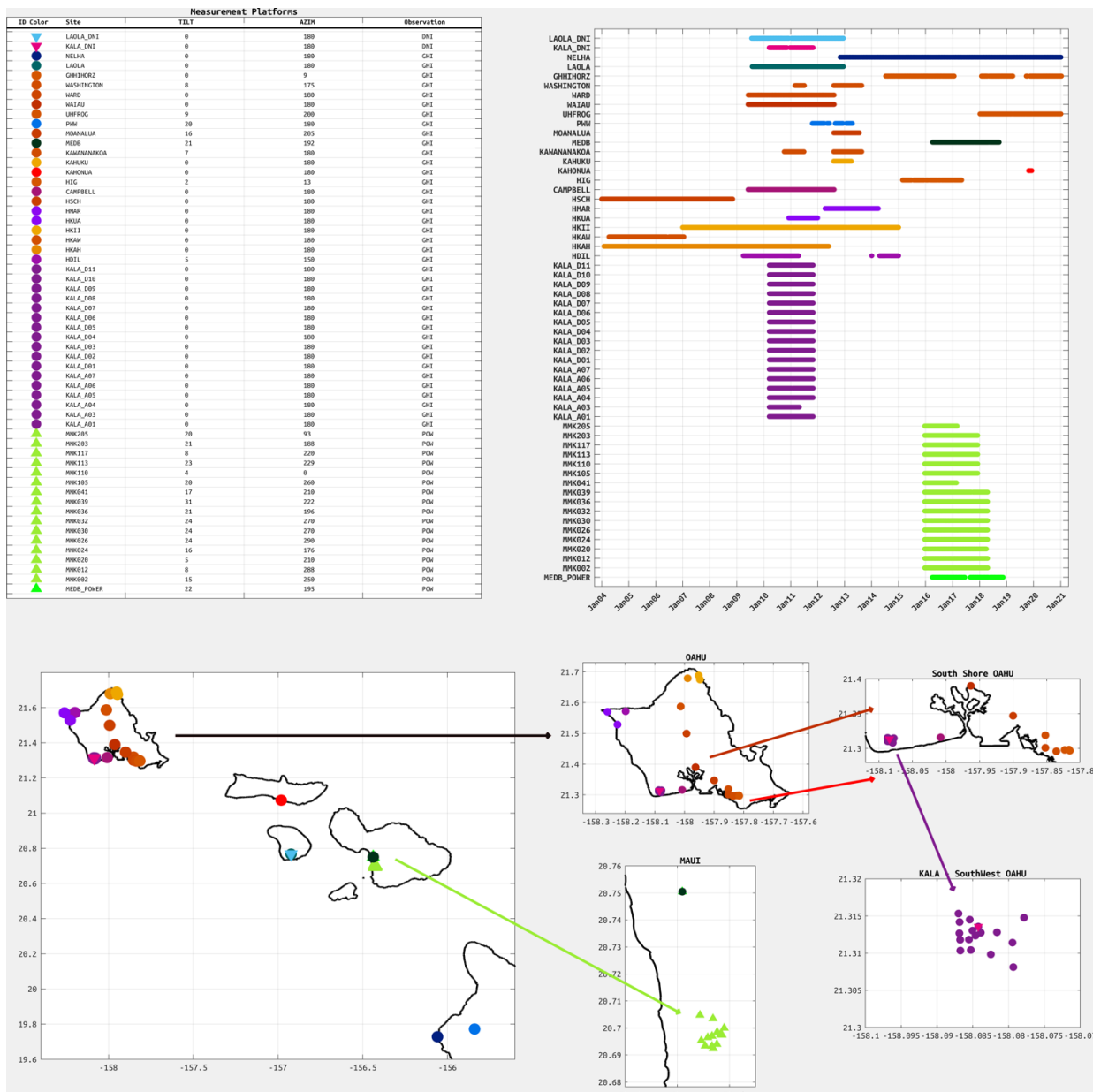


Figure 5.10.6. The solar resource observation database contains GHI, DNI, and PV power measurements providing a valuable resource for testing, calibration, and validation of different solar forecasting methodologies.

References

- [1] Reno, J. and Hansen, C. (2016). Identification of periods of clear sky irradiance in time series of GHI measurements. *Renewable Energy*, 90, 520-531.
- [2] Ineichen, P. and Perez, R. (2002). A new airmass independent formulation for the Linke turbidity coefficient. *Solar Energy*, 73(3), 151-157.

5.11 Marine Corps Base Hawai‘i Installation Energy Security Plan

HNEI is supporting Marine Corps Base Hawai‘i (MCBH) in completing its Installation Energy Security Plan (IESP) to enhance installation energy resilience and improve mission assurance. The IESP will document the current and future energy security requirements of MCBH (Figure 5.12.1), its ability to meet those requirements and plans to address high-priority gaps. It will consider resource constraints, statutory mandates, executive policy, and service-level priorities.



Figure 5.12.1. Marine Corps Base Hawai‘i at Kāne‘ohe Bay. (Photo credit: MCBH)

On May 30, 2018, the Office of the Assistant Secretary of Defense Energy, Installations, and Environment (OASD-EI&E) issued a memorandum, “Installation Energy Plans – Energy Resilience and Cybersecurity Update and Expansion of the Requirement to All DoD Installations,” mandating an IESP be prepared for MCBH. The IESP must consider the capacity, reliability and condition of the existing energy infrastructure on base, and the ability to meet future growth requirements. The IESP is envisioned to discuss, compare and contrast alternatives for energy security and resiliency, and recommend technical strategies and solutions. The solutions are to be based upon technologies that are already proven to be commercially viable and ready to implement. In developing the IESP, close coordination is required between HNEI and MCBH stakeholders through regular interaction and exchange to secure necessary information on the electrical infrastructure, plans, operations, critical load priorities and relevant base studies/assessments, among other things. The IESP includes seven stages and follows the planning framework shown in Figure 5.12.2.

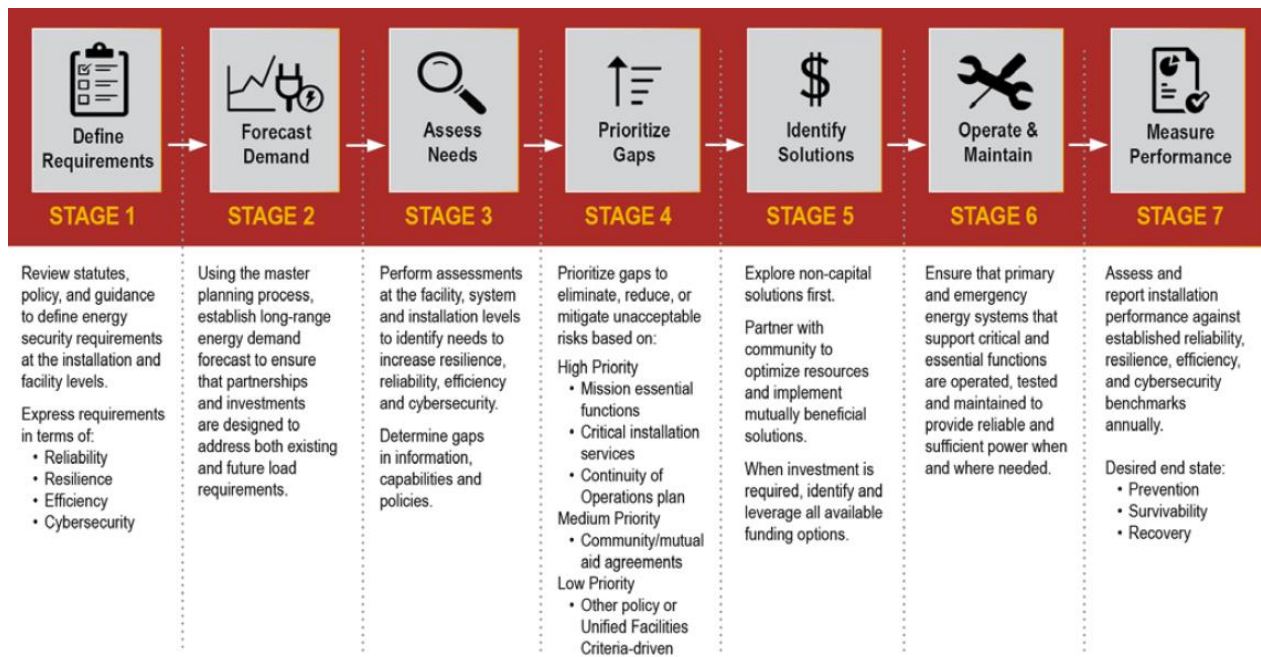


Figure 5.12.2. Marine Corps Installations Command IESP framework.

An initial draft report of the IESP including stages 1, 2, 3 and 4 above has been delivered by HNEI to MCBH and is currently under review. HNEI continues its work on stage 5 of the IESP. Stage 5 proposes solutions addressing the installation's energy resilience requirement of 14 days without commercial power. Alternative microgrid designs are being developed and assessed, including a microgrid solution that powers the entire base and smaller microgrids that maintain power to base priority loads.

HNEI uses a cloud-based software called XENDEE to evaluate different microgrid design options, new resources and resilience requirements. XENDEE implements a physically-based economic decision support system that couples financial optimization with detailed electrical power system analysis to verify resilience and the financial viability of microgrid projects.

Figure 5.12.3 below illustrates a conceptual microgrid design that utilizes the existing rooftop photovoltaic (PV) system at MCBH and proposes additional generation and energy storage resources to power the entire base through an extended utility service outage.

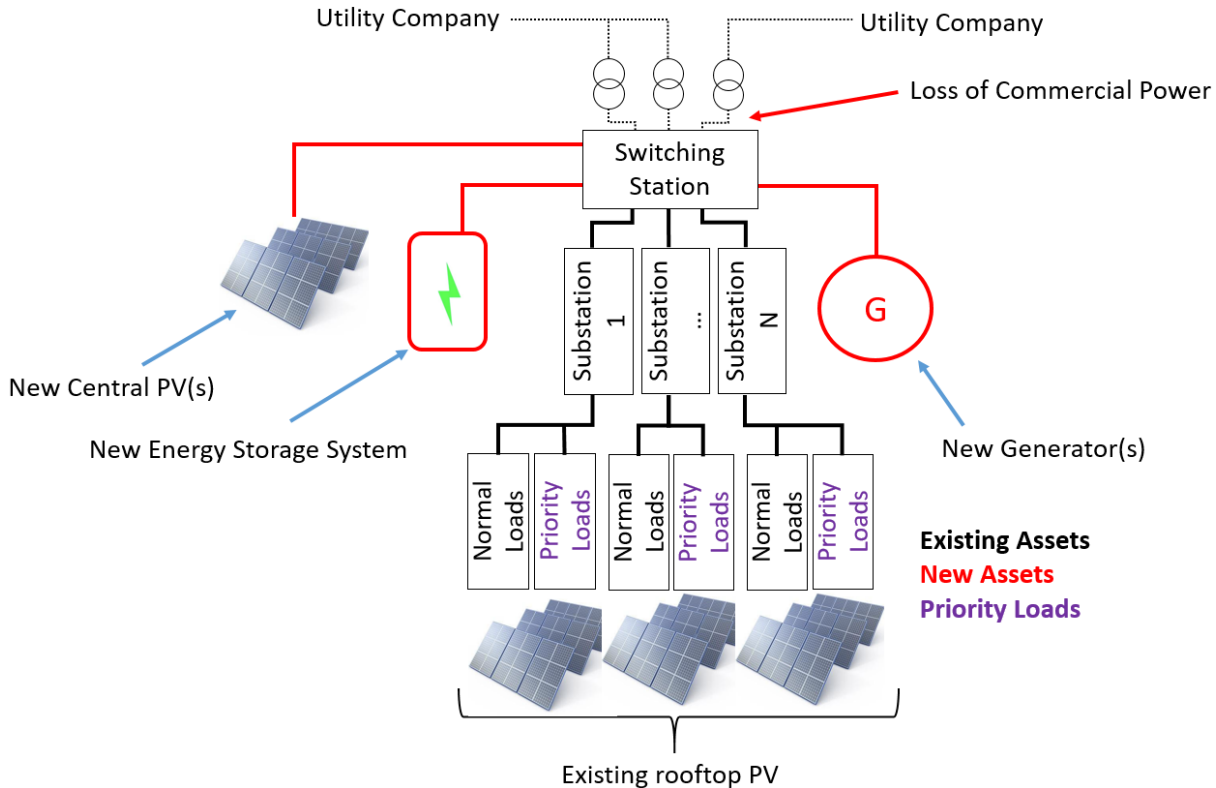


Figure 5.12.3. Conceptual design of a full base microgrid.

TASK 6: OCEAN ENERGY

The Ocean Energy Task supported two subawards. Makai Ocean Engineering continued efforts located within the Natural Energy Lab of Hawai‘i Authority (NELHA) in Kailua-Kona, Hawai‘i to develop thin foil heat exchangers applicable to a variety of U.S. Department of Defense (DOD) applications. The University of Alaska Fairbanks identified and evaluated techno-economic benefits or issues associated with integrating wave energy along with other variable renewable energy sources into small, isolated grid systems.

6.1 Ocean Thermal Energy Conversion (OTEC)

Under subaward to the University of Hawai‘i, Makai Ocean Engineering has been developing Thin Foil Heat Exchangers (TFHX) for use in seawater-refrigerant, air-water, and water-water applications. The work conducted under APRISES 15 was performed between August 2018 through January 2020. During this period, Makai made two iterations to the TFHX design. Makai reported that with each iteration, the materials cost was reduced by half, whereas the labor and

overhead cost remained roughly constant. Makai is developing a design for a High Speed Welding Station (HSWS) which is projected to speed up the fabrication process, specifically, the welding and expansion step. Under APRISES15, Makai conducted performance testing of the TFHXs, expanding testing fluids to include air in the external channels and installed air-water testing apparatuses. Seawater-ammonia and seawater-seawater performance testing was also conducted at the 100 kW test station. The first commercial TFHX unit was installed at Cyanotech. The TFHX was able to maintain the Cyanotech pond temperature below the maximum threshold temperature and used less cold seawater compared to Cyanotech's existing system. Following a three month test period, Makai discontinued monitoring but the TFHX unit remained installed and functional at Cyanotech.

In addition to producing plates for performance testing, Makai has also fabricated over 300 plates for characterization studies. Characterization studies focused on 1) determining the effective internal channel spacing, 2) determining the pressure rating (supported and unsupported burst pressures), 3) establishing a fatigue life (cycles to failure), and 4) determining the hydraulic performance for different fluids. Each test required multiple samples of the same plate for statistical analysis and demonstration of repeatability. Particularly for the fatigue tests, the variation in results has been larger than expected. Additional studies were conducted to understand the cause of this variability.

After over 10 years of experimental work, Makai concluded the aluminum corrosion testing program. The 10-year samples reinforced Makai's previous conclusion: aluminum alloy performance in seawater is unpredictable

The full technical report "**Ocean Thermal Energy Conversion (OTEC) Heat Exchanger Development: 2018-2020**" is available on the HNEI website at <https://www.hnei.hawaii.edu/publications/project-reports/aprises-15>.

6.2 Wave Energy Advancement

The objective of this project was to identify and evaluate techno-economic benefits or issues associated with integrating wave energy along with other variable renewable energy sources into small, isolated grid systems. This work was conducted by the University of Alaska Fairbanks (UAF) under subaward to the University of Hawai'i. Yakutat, a small Alaskan community of approximately 600 residents with diesel-based electrical loads of approximately 700 kW, is the focus of the study. The objective was achieved using a mix of tools including the Hybrid Optimization of Multiple Energy Resources (HOMER) model, the UAF-developed Micro Grid Renewable Integration Dispatch and Sizing (MiGRIDS) package, a Mathworks Simulink-based model. Inputs to the models included high-fidelity wave and solar photovoltaic (PV) resource data

and a high fidelity Simulating WAves Nearshore (SWAN) simulation. Economic assessments were conducted using output from MiGRIDS and HOMER. The potential for grid impacts for different mixes of wave and solar PV, a battery energy storage system (BESS), and existing diesel-based electrical generation assets was assessed using a basic Simulink simulation.

Electrical load data for Yakutat was provided by the Alaska Village Electric Cooperative (AVEC) for the year 2018 in 15 minute resolution. While MiGRIDS is intended for working with load data at intervals of several seconds, meaningful estimates of wave power were constrained to longer intervals, closer to 5 minutes [1,2]. Thus, an interval of 5 minutes was used for all simulations. Five minute interval load data, was derived from the AVEC provided data using a Langevin algorithm implemented in MiGRIDS (Vandermeer *et al.*, in prep). Community electrical demand peaks in summer when the local fish processing plant is operating and varies from a minimum of approximately 500 kW in January to a maximum of over 1000 kW in late summer. Oceanographic instruments to measure the local wave spectra were deployed beginning in June 2018 and a meteorological station with a Hukseflux SR30 pyranometer to record Global Horizontal Irradiance (GHI) was installed in August 2018. To avoid introducing any unknown biases into the analyses, it was decided that it was important to use wave and solar PV resource estimates from the same time period as the load data. Thus, a series of steps were taken in order to synthesize time series of the distributed energy resources that overlapped with the available load data and that were at the same sample interval.

In order to produce synthetic time series of wave power, the regional SWAN model described in Tschetter *et al.* was updated to present [3]. While the 2016 SWAN model utilized NOAA’s Global Forecast System (GFS) winds for forcing and NOAA WaveWatch III output for boundary conditions, the updated simulation employs winds and wave information from the European Center for Medium range Weather Forecasting’s (ECMWF) ERA5 product. The updated SWAN model was used to generate hourly time series of surface wave spectra for the same time period as the load data. SWAN output was validated against two nearby NOAA wave buoys as well as the in situ oceanographic moorings. The hourly SWAN output was then upsampled following Robertson *et al.* to match the 5 minute interval of the load data [2]. Predicted electrical outputs were then calculated by applying the 5 minute wave information to the power matrix for a given wave energy converter (WEC). In this manner, a time series of predicted power output for any number or design of WECs can be calculated. An example time series of power output from two 100 kW “Wave Bob” WECs is shown in Figure 6.2.1. Finally, custom scripts were written to feed the predicted WEC power output into HOMER and MiGRIDS.

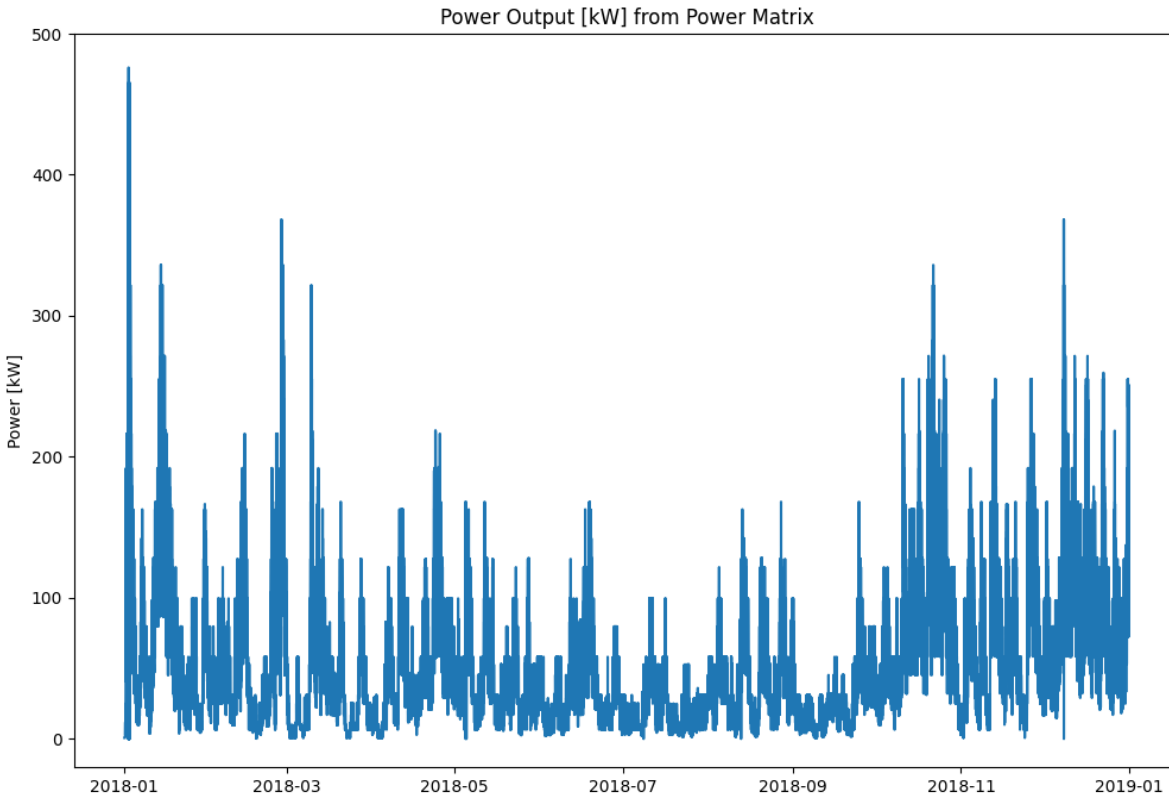


Figure 6.2.1. Predicted power output for two 100kW Wave Bob WECs for calendar year 2018.

A synthetic time series of GHI was produced using ERA5 data for Yakutat. This data is publicly available from NREL at a 1 hour sample interval. Following Wilber *et al.*, in situ GHI data measured by the pyranometer on the met station was averaged to hourly [4]. Then each day of satellite data was matched to a “representative day” from the in situ data. Representative days were found by minimizing the mean square error between the two hourly time series day by day. A synthetic time series was then generated by piecing together representative days from the 1 minute data. This time series was then corrected to equal the hourly average values found in the satellite dataset. Finally, the time series was averaged to 5 minute intervals. Figure 6.2.2 shows the resulting time series with a resolution of 5 minutes that matches the variance of the in situ data and the magnitude of the satellite data.

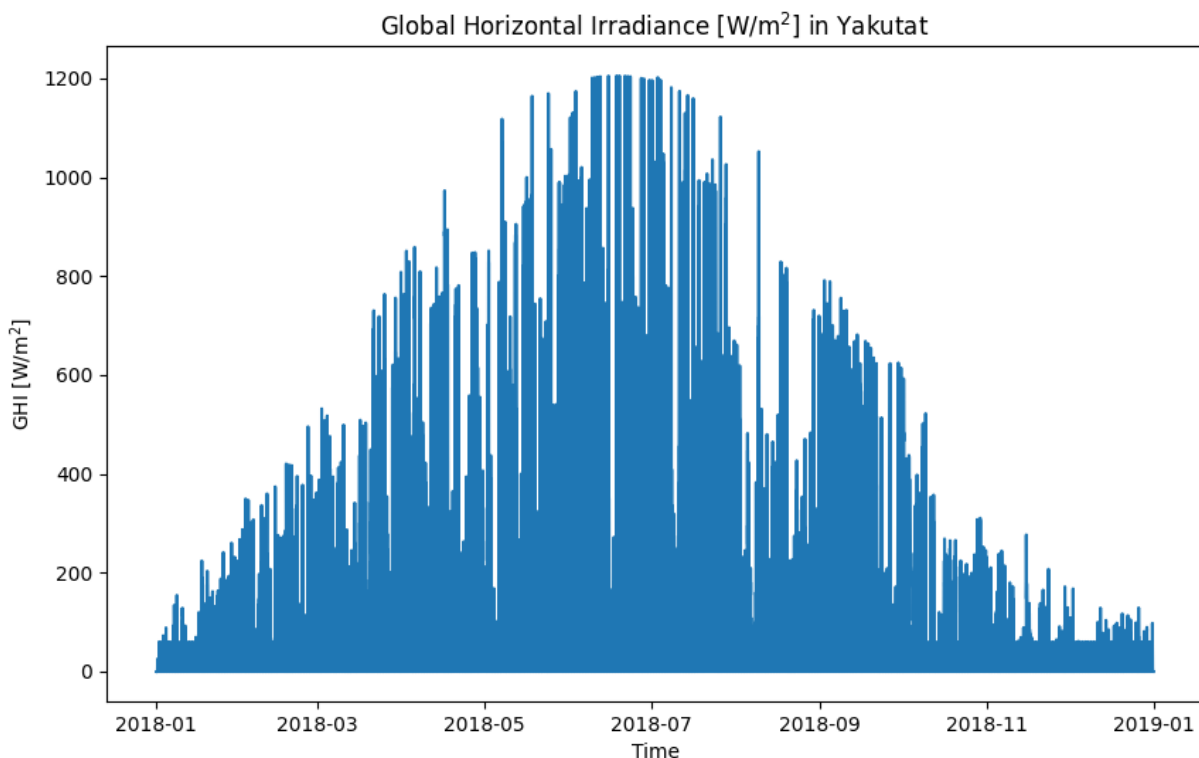


Figure 6.2.2. Synthetic timeseries of Global Horizontal Irradiance (GHI) for Yakutat in 2018.

Using these data, a series of HOMER and MiGRIDS simulations were carried out to quantify how much, if any, cost savings could be achieved by the introduction of solar PV and wave energy into the community's generation mix.

In order to maximize the potential penetration of the Distributed Energy Resources (DER) into the grid, a BESS was included in most simulations. In addition, the effects of system cost decreases with time were estimated using learning rates estimated from the literature.

Utilizing current conservative cost estimates, diesel generation was found to be the most economic option for the community with DER technologies slightly below cost-parity. However, future projections as early as 2030, with only modest average cost reductions, show the DER technologies could contribute to significant cost savings for Yakutat. While not showing near term value to the community, the development of the methodologies to include wave energy in simulation tools such as HOMER and MiGRIDS is an important outcome of this work.

Preliminary analysis of power quality issues following the introduction of PV and wave energy devices was conducted using Simulink. While the introduction of the WECs introduced a ripple that led to variations in frequency of up to 0.18 Hz, a more in-depth investigation would be needed to reach firm conclusions.

The full technical report “**Wave Energy Integration into Small Islanded Electrical Grids**” is available on the HNEI website at <https://www.hnei.hawaii.edu/publications/project-reports/aprises-15>.

References

- [1] Vandermeer, J., Mueller-Stoffels, M., Morgan, T., and Broderson, D. (n.d.). MiGRIDS (micro grid renewable integration dispatch and sizing).” Retrieved 2018, from <https://github.com/acep-uaf/MiGRIDS>.
- [2] Robertson, B., Bailey, H., Leary, M., and Buckingham, B. (2021). A methodology for architecture agnostic and time flexible representations of wave energy converter performance. *Applied Energy*, 287, 116588.
- [3] Tschetter, T., Kasper, J., and Duvoy, P.X. (2016). Yakutat Area Wave Resource Assessment. Alaska Center for Energy and Power. Retrieved from https://acep.uaf.edu/media/212381/Yakutat-Wave-Assessment_Nov2016.pdf.
- [4] Wilber, M. and Pike, C. (2018). Yakutat Instrumentation Documentation (Research Log). ACEP Internal Documentation.

TASK 7: ENERGY EFFICIENCY

Task 7 evaluates two aspects of the two mixed-mode, net zero energy buildings constructed on the University of Hawai‘i at Mānoa campus constructed under previous ONR grants: the impact on interior CO₂ levels from operational decision-making in mixed-mode buildings, and the variability of thermal comfort in a mixed mode building with the use of ceiling fans.

7.1 Energy and Indoor Air Quality in Mixed Mode Buildings

Under this subtask, HNEI conducted a study to determine the impact of user decision-making on adequacy of fresh air measure by measuring energy performance and using CO₂ as a marker for indoor air quality and fresh air exchange. Significantly different CO₂ concentrations were observed in the two identical classrooms. This study highlights the importance of user-familiarity with building operation in order to maintain a healthy indoor environment.

Climate change, population growth, building efficiency, and indoor air quality are conflicting drivers in the effort to meet aggressive carbon emission goals being imposed by several U.S. states and European countries [1]. Thus, today’s buildings should be designed to maximize energy efficiency in both the current and future warmer climates [2]. Mixed-mode buildings, a hybrid

energy design that can be either naturally ventilated or mechanically heated/cooled as conditions demand, are a potential solution to these challenges.

Air-conditioned classrooms, including mixed-mode, and retrofits in particular, often do not meet ventilation requirements through heating, ventilation, and air conditioning (HVAC) operation alone [3]. Mini-split AC units do not provide outside fresh air while window AC units often provide inadequate ventilation [4]. High levels of CO₂ resulting from insufficient ventilation can lead to lethargy and lower productivity when the concentration exceeds the acceptable threshold [5]. The ability to improve ventilation is becoming more acute and desirable in the current global pandemic [6,7].

Mixed-mode buildings rely on operable windows, skylights, clerestories, and other apertures to create natural ventilation opportunities. An unintended consequence of manually controlled mixed-mode classrooms can be poor fresh air exchange if insufficient outside air is introduced, due to either lack of awareness or training of the user. While clearly problematic, these under-ventilated conditions are not necessarily obvious to the user as demonstrated by high CO₂ concentrations measured in this study and by others. Chan *et al.* evaluated 104 classrooms in California to confirm inadequate ventilation and determine the root causes [3]. Fisk's comprehensive literature search found that "based on a review of literature published in refereed archival journals, ventilation rates in classrooms often fall far short of the minimum ventilation rates specified in standards" [8].

In this study researchers monitored the two classrooms to evaluate the energy savings of a unique and dedicated *on-demand* AC thermostat while monitoring CO₂ levels and other indoor variables. The work was conducted in two identical mixed-mode classroom buildings located in International Energy Conservation Code climate zone 1 at the University of Hawai'i at Mānoa (UHM).

The two identical 134 m² (1,440 ft²) classroom buildings dubbed FROG1 and FROG2 (Figure 7.1.1) were constructed on the UHM campus in 2015-2016 to test building design and fabrication strategies and research new technologies and energy control systems. These single-room classroom buildings were equipped with split-system AC units with an outside air supply. Monitoring systems were installed during construction to measure temperature, humidity, light, CO₂, energy flows, and outdoor conditions over three calendar years. Hourly outdoor temperatures complied with the American Society of Heating, Refrigerating and Air-Conditioning Engineers (ASHRAE) Standard 55's adaptive comfort standard for 80% satisfaction for 87% of hours of the year (only 2.5% of hours were too hot), which makes the buildings suitable for mixed-mode [9]. Detailed building characteristics and environmental conditions can be found in the full technical report referenced below. The interior conditions of the FROGs were found to be highly dependent upon the knowledge and preference of the user to choose between using natural ventilation or activating the on-demand AC unit.



Figure 7.1.1. FROGs 1 and 2 at the University of Hawai‘i at Mānoa. (Photo credit: University of Hawai‘i)

In addition to serving as research platforms, the FROGs are used as classrooms for middle school students in the morning and university students in the afternoon and evening. They generally operate in change-over mode, when natural ventilation and AC operation are mutually exclusive. Because they are manually controlled, they may be alternatively run in a concurrent mode, when AC and natural ventilation occur simultaneously. The mode is chosen by user preference.

The classrooms were monitored over three calendar years (two school years) to measure thermal comfort, CO₂ concentrations, and energy performance. The schedules of the classrooms are dynamic with user group and class size that vary broadly by hour and day. While the buildings are fully occupied during the mornings (8:00 a.m. to 1:00 p.m.) by several groups of middle school students (45-min classes), during the 2-1/2 to 3-hour afternoon and evening sessions, the buildings are not at full capacity.

Previous researchers have reported that the more engaged the users are in the operation of their space, the more adaptive and tolerant they are of higher and lower temperatures [10,11]. Both FROG classrooms were designed to actively engage users, while also utilizing some degree of automated controls. In particular, the AC systems were outfitted with a manually activated, on-demand thermostat control that allows the AC to run for 60 minutes. This required user engagement to optimize comfort, while reducing energy use by limiting the run-time during unoccupied periods.

While the two buildings, located adjacent to each other experience the same outdoor conditions, have the same equipment, and on average have the same number of occupants with similar activities, the users operated the AC, lighting, ceiling fans, and windows quite differently. During the first school year of investigation, the users of FROG1 frequently engaged the AC upon arrival in the morning without opening windows, while users of FROG2 primarily relied on natural ventilation. When the FROG1 users relied on AC only, the average hourly CO₂ concentration frequently exceeded the 1,100 ppm acceptable maximum and occasionally reached the sensor’s upper range limit of 2,000 ppm (Figure 7.1.2) [12]. This was despite the AC systems passing the

testing, adjusting, and balancing commissioning tests. During a period when both AC systems were simultaneously down for repair and maintenance in October 2018, the users had to rely upon open windows and ceiling fans for thermal comfort and ventilation resulting in far lower CO₂ concentrations (Figure 7.1.3).

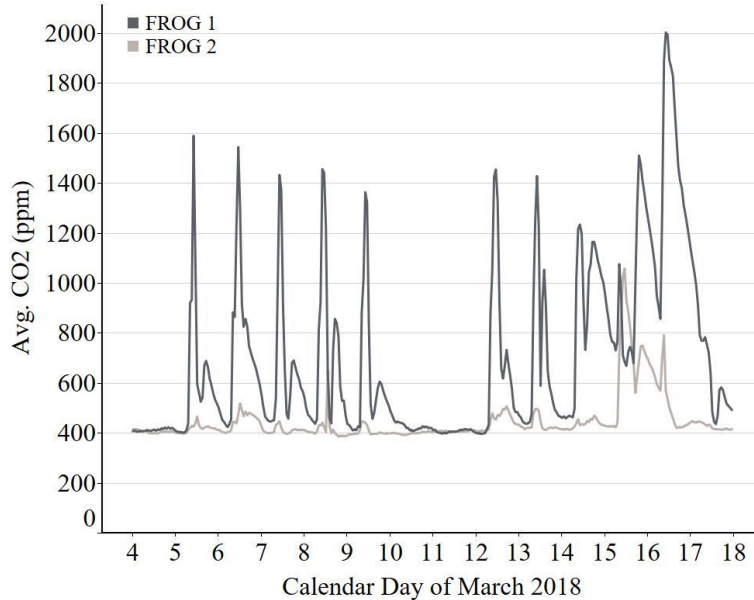


Figure 7.1.2. Two weeks of hourly average CO₂ data in March 2018. FROG1: AC on daily resulting in higher CO₂ concentrations. FROG2: AC used only on one day (16 Mar. 2018) resulting in lower overall CO₂ levels.

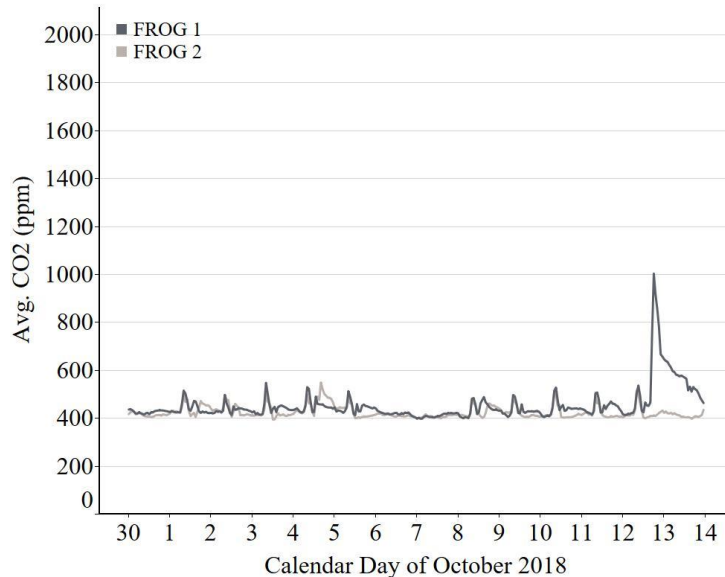


Figure 7.1.3. Two weeks of hourly average CO₂ data in October 2018 when both AC units were under repair and not operational, which resulted in open windows and use of ceiling fans for comfort. The spike on 13 Oct. 2018 is likely due to windows not being opened.

Energy consumption in the buildings was divided into four primary end-uses: HVAC, ceiling fans, lighting, and “other loads” that include telecommunications, fire-alarm, multimedia, and miscellaneous plug loads. In order to compare the energy used by the buildings during the different months, the normalized energy values (kWh/day), evaluated over a 24-hour period, were used, while also making a distinction between school-day and non-school day operation. Although the two buildings are located on the same site, experienced the same outdoor conditions, have the same equipment installed, and are occupied, on average, by the same number of occupants and occupant type during the morning (middle school students) daily, afternoon and evening sessions (university students) with high variability in occupancy, each building’s features, such as HVAC and ceiling fans are used quite differently. The morning instructors in charge of each building were the same every day for the entire school year. Both buildings used more electricity during the morning sessions with the higher consumption during the 2017-2018 school year. Users in FROG2 consciously did not turn the AC system on and used the ceiling fans more consistently. Greater variability occurs in the afternoon and evening sessions with the buildings being frequently unoccupied.

Researchers provided initial instructions to users with the intention of fostering an understanding of building operation and instill more energy-conscious behavior. To provide visual feedback, the buildings’ performance was displayed on a wall-mounted dashboard in each classroom that graphically rendered the energy consumption, energy generation, CO₂, and environmental conditions in both buildings. Even with initial training, data showed that during the first calendar year of study (2017) many of the instructors ran the AC unit frequently and seldom opened windows.

After two years of operation, it became apparent that a more focused training was required to optimize building operation and maintain a healthy indoor environment. Training sessions at the beginning of the third calendar year (January 2019) focused on ensuring that the instructors understood the importance of providing ventilation by opening windows when AC was not in use. Concurrent use of AC and natural ventilation was also recommended in spite of being contrary to typical use of AC where it is customary to close the windows to prevent cooling losses and outside heat intrusion. The 2019 results showed that training and user awareness of the CO₂ issue significantly impacted how occupants operated the buildings. Figure 7.1.4 shows how the number of CO₂ readings exceeding 1,000 ppm (up to the sensor limit of 2,000 ppm) was reduced in 2019.

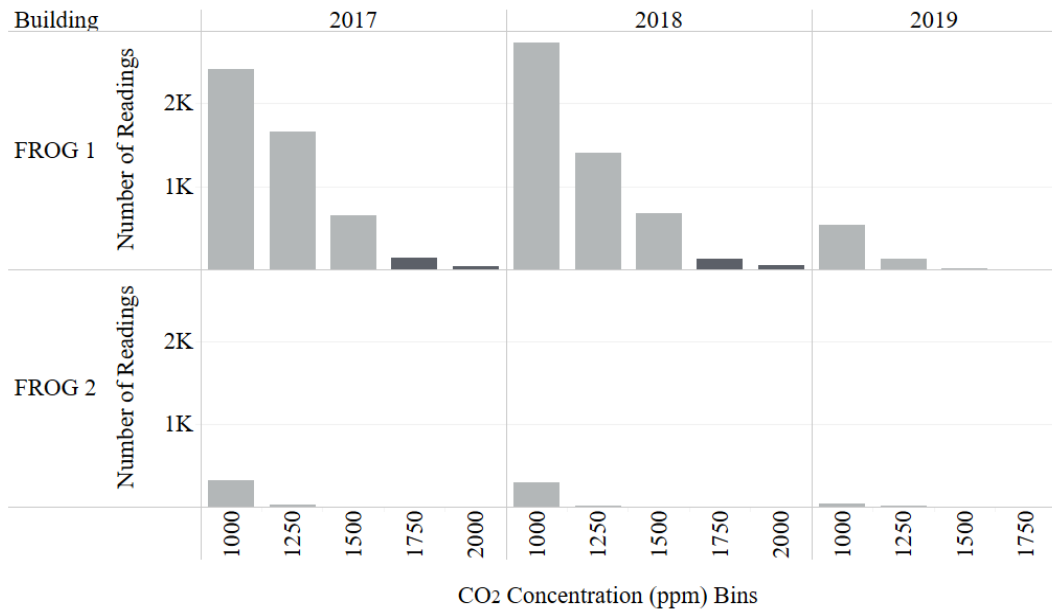


Figure 7.1.4. Histogram of the number of 5-minute CO₂ readings that exceeded 1,000 ppm on weekdays between 7:00 AM and 8:00 PM for three calendar years of monitoring.

During the first two calendar years, the CO₂ levels occasionally spiked after the AC automatically turned off, suggesting that the occupants had not left the building nor opened windows. The dashboard display was not effective in cuing the users to the increasing CO₂ levels. In the third calendar year, an LED CO₂ indicator light was installed in a conspicuous location in line of sight of the instructor as a visual cue. This multi-LED indicator displayed the current status of CO₂: green (< 1,000 ppm), yellow (>1,000 ppm), and red (> 1,750 ppm). This provided instructors with additional information to determine if a manual intervention was necessary, such as opening windows. Through these human-driven interventions and manual control of the indoor space and ceiling fans, they were able to maintain a healthy and comfortable learning environment.

Frequently, when the windows were not opened, the CO₂ continued to rise during the afternoon and evening classes but slowly decreased overnight such that early morning values (between 6:00 a.m. and 6:59 a.m.) were higher than the baseline (400 ppm), indicating the room was not sufficiently diluted and diffused prior to entering the building in the morning. This non-diffusion/dilution of overnight CO₂ has a perverse effect on the readings of the CO₂ monitoring instruments. The recalibration process assumes that the room has been ventilated well enough to reach the outdoor CO₂ baseline value of 400 ppm. Because the actual early morning CO₂ levels may be higher than the artificial basis of 400 ppm, the readings the next day will be underestimated.

As a response to environmental and indoor public health challenges, mixed-mode buildings provide an opportunity for users in tropical, cooling-only climates to control their indoor environment at a lower energy cost. On one hand, mixed-mode allows users to choose to open windows to increase ventilation rates. Conversely, mixed-mode can provide a false sense of well-

being when the user feels that the choice between natural ventilation and air conditioning is a binary decision and that either one will provide adequate ventilation. In many cases, because AC may not provide adequate fresh air, CO₂ concentrations are likely to increase without the user.

This report has focused on CO₂ concentration as a proxy for indoor air quality. The analysis was also performed in the context of maintaining acceptable levels of thermal comfort. The perception of thermal comfort is a driver for a user's decision to mechanically cool. As evidenced by the marked differences in HVAC usage by FROG1 and FROG2 under identical conditions, there appears to be a fine line between one's perceived comfort and another's discomfort. While one FROG user may request air conditioning every day, another may not. Mixed-mode buildings' manual and mechanical systems can accommodate each mode. Thermal comfort is a determinant as to whether to run AC or open windows is not necessarily a binary choice. In areas such as Hawai'i, windows may be opened to allow air circulation concurrently with the AC being on to maintain comfort as well as natural ventilation. The investigation also showed that outdoor conditions were not the single driver for difference in use of the HVAC systems. Buildings experiencing the same outdoor conditions used HVAC and ventilation differently.

Repeated training and conspicuous visual cues such as LED CO₂ indicators assist the users in understanding the appropriate operating protocols for the building and the effect on decision-making. An energy saving, on-demand thermostat that automatically turns off the AC after one hour might leave an untrained occupant without adequate ventilation if they did not re-activate the AC or open the windows. This on-demand timer/controller requires more training of users than a conventional thermostat. As a result of the potential weaknesses in classroom AC systems to provide adequate fresh air, as well as fallible human decision-making, automated systems activated by temperature, humidity, and CO₂ sensors are a healthier solution to ensure mixed-mode classrooms remain healthy, vibrant learning environments in a tropical environment.

Other variables, including detailed hourly analysis by time of day, AC operation, and indoor environment that offer additional insight into indoor air quality in two mixed mode buildings are evaluated in the full technical report "**A Case Study of Indoor Air Quality in Mixed Mode Buildings in Tropical Environments**" available on the HNEI website at <https://www.hnei.hawaii.edu/publications/project-reports/aprises-15>.

Publications and Presentations

Peer-Reviewed Publications

1. Cerri, S., Maskrey, A., and Peppard, E. (2020), Retaining a healthy indoor environment in on-demand mixed-mode classrooms, *Developments in the Built Environment*, 4, 100031.

References

- [1] Darby, M. and Gerretsen, I. (2019, June 14). Which countries have a net zero carbon goal? Climate Home News. [https://www.climatechangenews.com/2019/06/14/countries-netzero-climate-goal/](https://www.climatechangenews.com/2019/06/14/countries-net-zero-climate-goal/)
- [2] de Wilde, P., Coley, D., (2012). The implications of a changing climate for buildings. *Building and Environment*, 55, 1-7.
- [3] Chan, W.R., Li, X., Singer, B.C., Pistochini, T., Vernon, D., Outcault, S., Sanguinetti. A., and Modera, M. (2020). Ventilation rates in California classrooms: Why many recent AC retrofits are not delivering sufficient ventilation. *Building and Environment*, 167, 106426.
- [4] Sheet Metal and Air-Conditioning Contractors' National Association. (2019). Mini-split systems in residential retrofit applications. Retrieved from https://www.smacna.org/docs/default-source/market-sector---residential/mini-split-systems-residential-retrofit-applications-2019.pdf?sfvrsn=b9ebcaa5_4.
- [5] Allen, J.G., MacNaughton, P., Satish, U., Santanam, S., Vallarino. J., and Spengler, J.D. (2016). Associations of cognitive function scores with carbon dioxide, ventilation, and volatile organic compound exposures in office workers: A controlled exposure study of green and conventional office environments. *Environmental Health Perspectives*, 124(6), 805–812.
- [6] Morawska, L. and Cao, J. (2020). Airborne transmission of SARS-CoV-2: The world should face the reality. *Environment International*, 139, 105730.
- [7] Correia, G., Rodrigues, L., Gameiro da Silva, M., Gonçalves, T. (2020). Airborne route and bad use of ventilation systems as non-negligible factors in SARS-CoV-2 transmission. *Medical Hypotheses*, 141, 109781.
- [8] Fisk, W.J. (2017). The ventilation problem in schools: literature review. *Indoor Air*, 27(6), 1039-1051.
- [9] American Society of Heating, Refrigerating and Air-Conditioning Engineers. (2017). Thermal environmental conditions for human occupancy (Standard 55). Retrieved from <https://www.ashrae.org/technical-resources/bookstore/standard-55-thermal-environmental-conditions-for-human-occupancy>.
- [10] Pigman, M., Brager, G.S., and Zhang, H. (2018). Personal control: Windows, fans, and occupant satisfaction. Windsor Conference: Rethinking Comfort., Windsor, United Kingdom, April 12-15, 2018.
- [11] Brager, G., Paliaga, G., and de Dear, R. (2004). Operable windows, personal control and occupant comfort. *ASHRAE Transactions*, 110(2).
- [12] American National Standards Institute/American Society of Heating, Refrigerating and Air-Conditioning Engineers. (2013). Ventilation for acceptable indoor air quality (Standard 62.1-201). Retrieved from <https://www.ashrae.org/technical-resources/bookstore/standards-62-1-62-2>.

7.2 Ceiling Fan and Thermal Comfort Assessment for Mixed-Mode Classrooms in Hawai‘i

This subtask summarizes research on the impact of ceiling fans on thermal comfort experienced in the FROG buildings (FROG1 and FROG2) located on the University of Hawai‘i’s Mānoa campus. The research used both subjective and objective data to comprehensively describe fan performance, fan control preferences, occupant responses to thermal conditions, and compared user perceptions with industry-accepted thermal comfort model predictions.

Thermal comfort analyses were performed using the American Society of Heating, Refrigerating and Air-Conditioning Engineers (ASHRAE) Standard 55’s Adaptive Comfort Model (ACM) and the Predicted Mean Vote (PMV) model. For each, the percentage of people expressing satisfaction in the survey is compared to the level of satisfaction that would have been predicted by the models using measured environmental conditions [1]. The researchers concluded that, in Hawai‘i’s tropical climate, the ASHRAE models are inconsistent and sometimes poor predictors of thermal comfort. The two FROG mixed-mode classroom buildings, described in more detail under Subtask 7.1, were designed to provide natural ventilation, as well as a single zone air conditioning (AC) system for use when warmer conditions demand. The classrooms were also equipped with three sets of three ceiling fans, each set with a 7-speed controller. Given the choice of using natural ventilation, ceiling fans, and/or AC, the behaviors and preferences of the users resulted in very different operating conditions of the buildings throughout the weekly schedule and from semester to semester. The full technical report describes details of how the buildings were operated, including frequency of ceiling fan use, ceiling fan speeds, AC use, and whether windows were opened for natural ventilation. A survey asking occupants to vote on their level of satisfaction with the thermal conditions in the room was conducted in FROG1. The results of the survey were matched with the environmental conditions in the room preceding each vote. The percentage of people expressing satisfaction in the survey was then compared to the level of satisfaction that would have been predicted by the ASHRAE Standard 55’s ACM and the PMV model. A detailed description of FROG equipment and methods can be found in the full technical report referenced at the end of this section.

The FROGs have three banks of three ceiling fans, each bank metered separately: north bank located in the entryway and middle and south banks in the classroom (Figure 7.2.1).

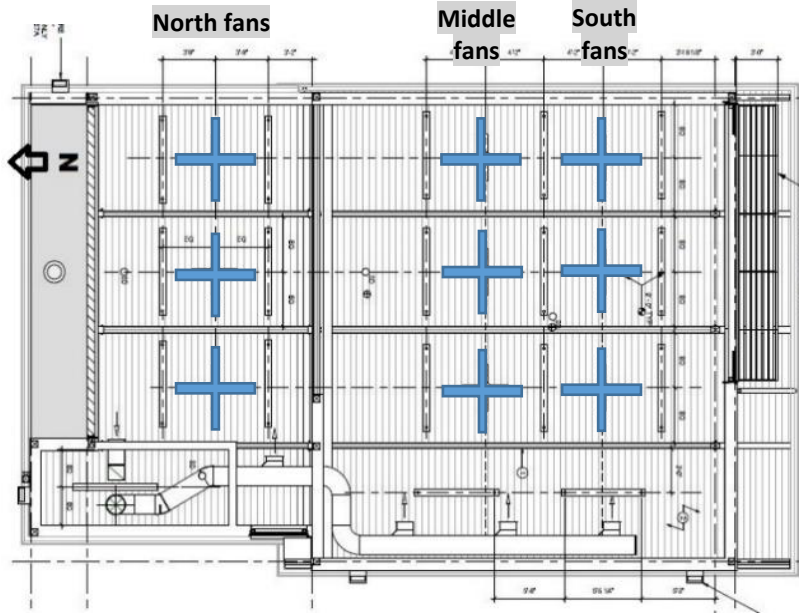


Figure 7.2.1. Three banks of fans in FROG buildings: north in the entryway and middle and south banks in primary classroom.

In FROG1, the ceiling fans were the only option for “cooling” while the AC was out-of-service in the early fall of 2019 (late August through October 30). They were used 96% of the time and the windows were open 93% of the time. During late fall, after the AC was repaired, the ceiling fans were used 94% of the time, the AC was used 56% of the time, and the AC and ceiling fans were on concurrently 55% of the time (in other words, the ceiling fans were nearly always in use when the AC was on). In the late fall, the windows were open only 14% of the time and were rarely left open when the AC was ON. Conversely, in FROG2, the ceiling fans were used 82% of the time in early fall during the period the AC was out of service, and the windows were open 88% of the time. In the late fall, a similar usage of ceiling fans (85%) and open windows (86%) was the dominant pattern. The AC was used only 6% of the time (vs 56% for FROG1). However, this instructor chose the option of leaving at least one window open while the AC was on. A kiosk was installed in FROG1 on August 26, 2019 through March 30, 2020 that collected a one-question thermal comfort response from occupants (Figure 7.2.2). The question on the survey was “How acceptable is the room temperature?” (Figure 7.2.3). The possible responses were on a 7-point Likert scale: highly acceptable, moderately acceptable, slightly acceptable, neutral, slightly unacceptable, moderately unacceptable, and highly unacceptable. Participation was voluntary and the instructions for participation encouraged the occupant to respond at the end of their class period, so they would be acclimated to the conditions.

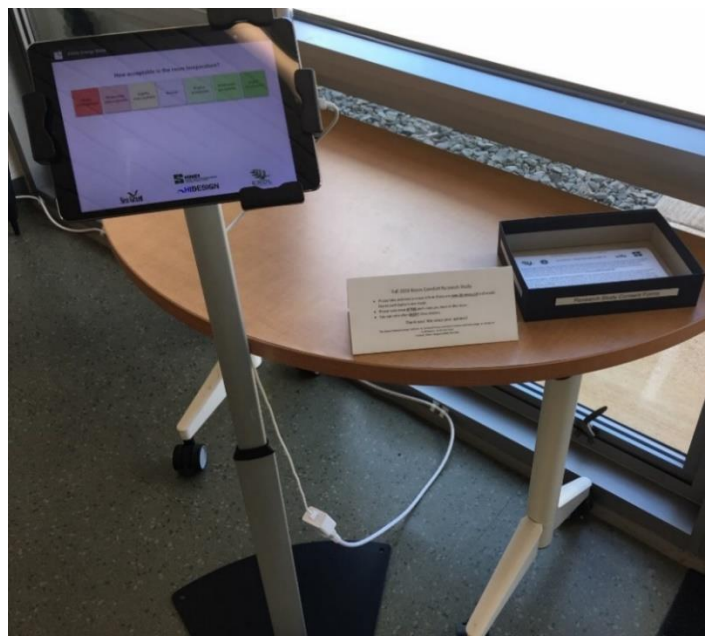


Figure 7.2.2. A kiosk made of a tablet on a stand was installed by the door of FROG1 with a sign giving instructions and a box of consent forms.

How acceptable is the room temperature?

Highly unacceptable	Moderately unacceptable	Slightly unacceptable	Neutral	Slightly acceptable	Moderately acceptable	Highly acceptable
---------------------	-------------------------	-----------------------	---------	---------------------	-----------------------	-------------------

Figure 7.2.3 A screenshot of the question on the tablet. Pressing a box on the screen triggers a “Thank You” message and automatically logs the timestamped response. The screen re-sets to the question in 3 seconds in order to avoid creating a queue.

A summary of all 407 responses is shown in Figure 7.2.4, with only 34% of the responses in the neutral to highly acceptable categories.

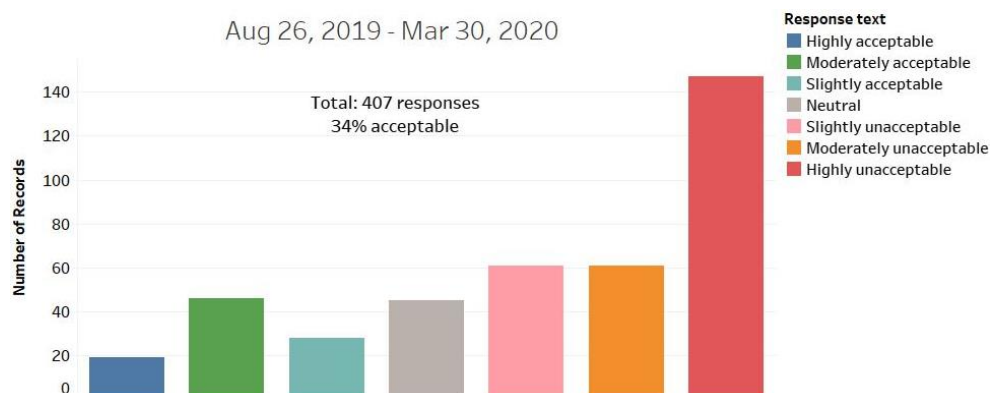


Figure 7.2.4. Number of responses in each category of acceptability of the room temperature for the duration of the study.

The AC was out-of-service from August 26 through October 31, 2019. Figure 7.2.5 compares the responses from before the AC was repaired to the responses after it was repaired. The weather also cooled off after October and the rate of “acceptable” responses increased to 50%.

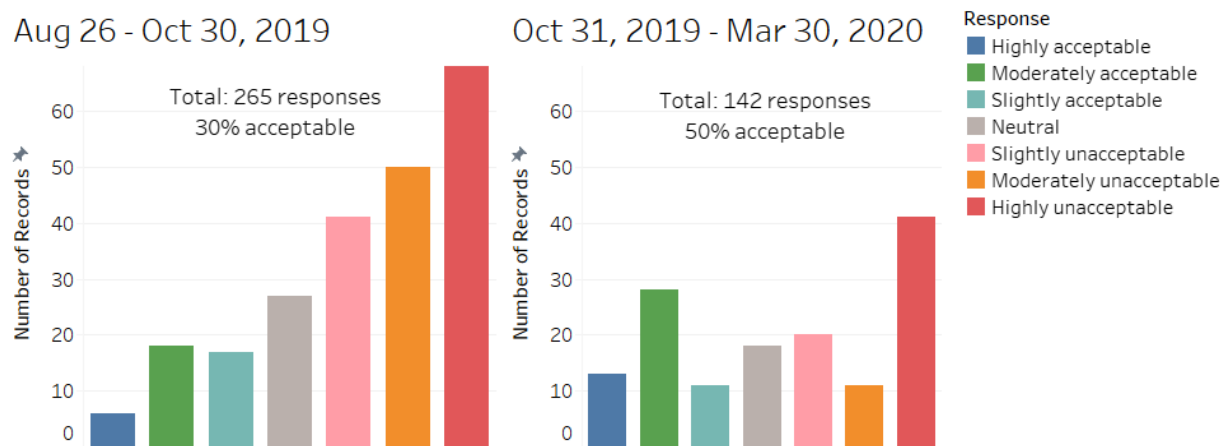


Figure 7.2.5. Number of responses in each category of acceptability of the room temperature before and after the AC was repaired.

The ASHRAE Standard 55-2017 for Thermal Environmental Conditions for Human Occupancy has established two accepted thermal comfort models: 1) the ACM, which was originally designed for spaces that are naturally ventilated and have no AC system installed and 2) the PMV model that was developed to predict thermal comfort in mechanically conditioned spaces [1]. The FROG buildings are mixed-mode, and traditionally the PMV model would be used because air conditioning is present. Recently, however, researchers from the UC Berkeley Center for the Built Environment (CBE) and the University of Sydney concluded that the ACM is a better fit for mixed-mode buildings than the PMV model [2]. For the analysis of the thermal comfort survey, the responses were compared with the predictions of the two models.

The ***Adaptive Comfort Model (ACM)*** of ASHRAE Standard 55-2017 defines the acceptable thermal conditions for occupant-controlled, naturally ventilated spaces under the following conditions: a) there is no AC system in operation; b) occupants have metabolic rates ranging from 1.0 to 1.5; c) occupants are free to adapt their clothing; and d) the prevailing outdoor temperature is greater than 50°F and less than 92.3°F [1]. The data was analyzed again using the adaptive comfort model graph in the following conditions to make a comparison between the model prediction and the actual votes. Figure 7.2.6 illustrates the process flow.

- All votes under all conditions plotted on the graph with the standard 80% acceptability limits for the upper and lower boundaries for the comfort zone, no filtering or adjustments for conditions.
- Votes filtered for when AC was OFF during the previous 30 minutes in order to analyze only the naturally ventilated conditions.

- Votes when AC was OFF displayed with adjustments to the operative temperature according to the estimated air speed based on middle fans power use. Since it is unknown where the occupant was sitting in the classroom, three cases were considered:
 - No elevated air speed included in the model;
 - Air speed calculated for an occupant seated directly under a ceiling fan; and
 - Air speed calculated for an occupant seated between two ceiling fans.

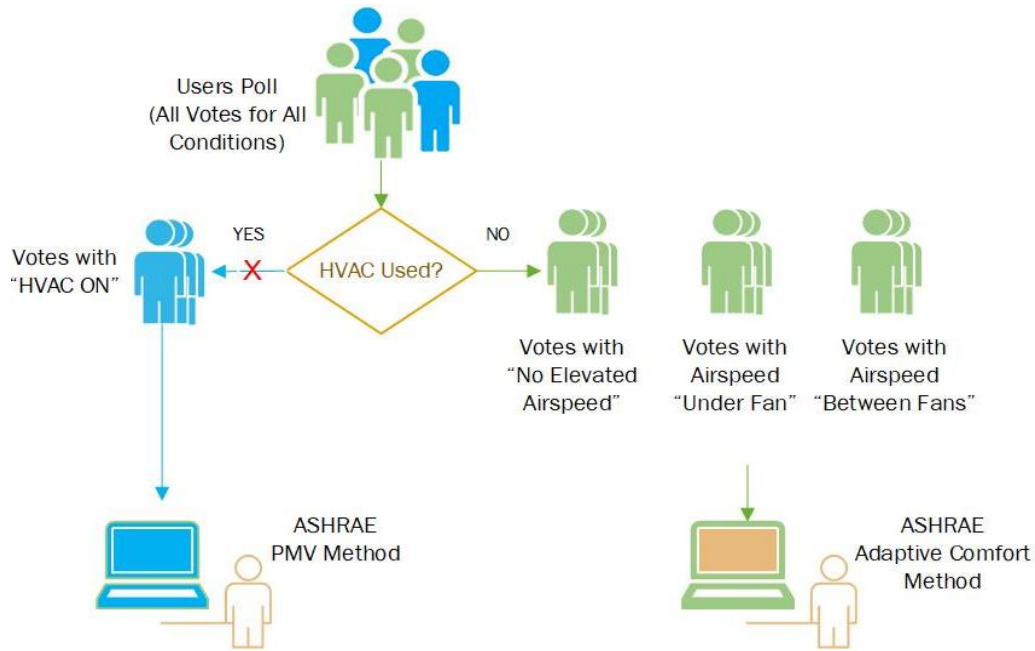


Figure 7.2.6. Work flow for data analyses using the ASHRAE-2017 ACM.

The graphic comfort zone method of the model plots a graph of operative temperatures (Figure 7.2.7) on the y-axis and prevailing outdoor air temperatures on the x-axis and defines comfort zone. It defines a comfort zone where 80% of respondents would find the operative temperature acceptable within upper and lower limit boundary lines.

Figure 7.2.7 is an example of an ACM graph with the 90% acceptable range in dark blue and the 80% acceptable range which also includes the areas in light blue.

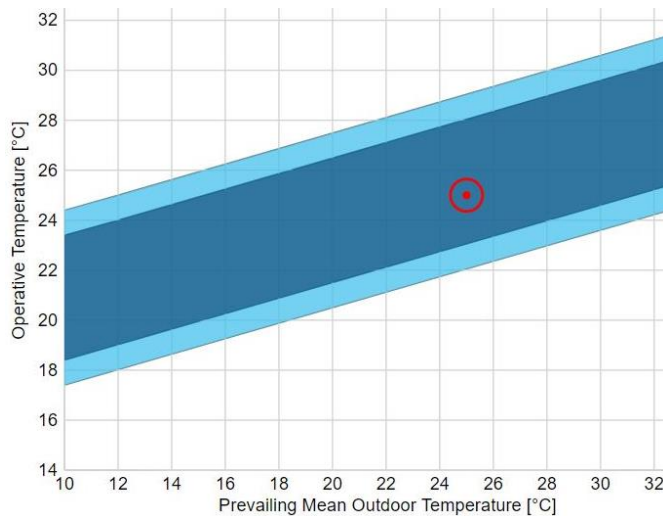


Figure 7.2.7. Center for the Built Environment online Thermal Comfort Tool (CBE) displays the thermal comfort range for the ACM [3,4].

The thermal comfort survey was deployed on a tablet kiosk in FROG1 from August 26, 2019 to March 30, 2020. Of the 407 total overall votes, 138, or 34% of the responses considered the spaces to be acceptably comfortable (“highly acceptable”, “moderately acceptable”, “slightly acceptable” and “neutral”). The results were plotted on an adaptive comfort graph (Figure 7.2.8). In this figure, the color of the point indicates the voter response (pink, orange, and red are *not acceptable*), while the region between the lines indicate conditions predicted by the model to be acceptable to 80% of respondents. Of the 407 total responses, 351 were recorded when the data was filtered for AC OFF and 162 responses when the conditions fell between the ASHRAE boundary lines for 80% acceptability. Of the 162, only 47% were reported as acceptable, an indicator that the model may not be a good predictor of the responses.

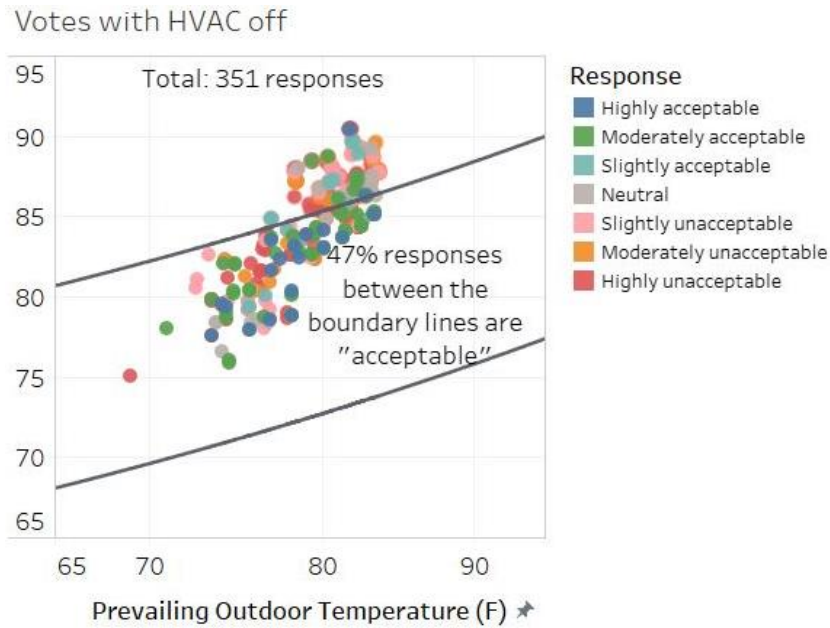


Figure 7.2.8. Thermal comfort votes plotted on the ACM's graph: operative temperature vs prevailing outdoor temperature. The color of the dot indicates the response category. Results from all responses are displayed on the left, responses when HVAC was turned OFF are displayed on the right.

The tests were run at different air speed conditions since ceiling fans improve the perception of comfort quantified in degrees Fahrenheit. The upper operative temperature limit in an adaptive comfort graph increases between 2 to 4 degrees Fahrenheit when air speed is elevated. Table 7.2.1 compares the ASHRAE comfort model predictions against the actual responses under different air speed conditions. For example, of the 162 votes that ASHRAE would have found acceptable at no elevated air speed, only 47% of the respondents found them so. In none of the cases did the actual responses approach the ASHRAE estimates. The ASHRAE adaptive comfort Model is therefore was shown to be a poor predictor of performance in these buildings in this climate.

Table 7.2.1. ASHRAE 55 Standard ACM predictions for thermal comfort vs the actual survey votes of occupants. Three possible air speed conditions were analyzed. Of the 351 total votes during periods of no elevated air speed, 189 did not comply with ASHRAE acceptable conditions, yet 19% or the respondents found the space acceptable.

ASHRAE 55 adaptive comfort model results	Air speed assumption used in model		
	No elevated air speed	Air speed between fans	Air speed under a fan
Complied with standard (80% acceptable)	Actual votes: N=162 47% Acceptable	Actual votes: N=260 38% Acceptable	Actual votes: N=325 34% Acceptable
Did not comply (too hot)	Actual votes: N=189 19% Acceptable	Actual votes: N=91 13% Acceptable	Actual votes: N=26 8% Acceptable

The second ASHRAE test compared to actual responses is the ***Predicted Mean Vote (PMV) model*** which is applied to a mixed-mode building when AC is being used. The PMV model is intended to predict the mean value of thermal sensation votes (see Table 7.2.2 for values of votes associated with different thermal sensations) of a large group of people. The acceptable range is: $-0.5 < \text{PMV} < +0.5$. Related to this range is an index of the predicted percent dissatisfied (PPD) of <10 , or less than 10% of people experiencing the thermal conditions are predicted to report being dissatisfied. The Standard also states that “local discomfort effects are assumed to contribute an additional 10% PPD to the discomfort predicted by PMV, so that the total PPD expected in a building with $\text{PMV} \pm 0.5$ will be 20%”, in other words an 80% satisfaction rate [1].

Table 7.2.2. Values associated with thermal sensation survey responses used to formulate the PMV model for ASHRAE Standard 55.

PMV vote value	Thermal sensation
-3	Cold
-2	Cool
-1	Slightly cool
0	Neutral
+1	Slightly warm
+2	Warm
+3	Hot

There were 37 survey votes cast under AC ON conditions: 19 acceptable and 18 unacceptable. Thermal conditions that are found to be compliant with ASHRAE 55 using the PMV model would be expected to have an 80% acceptability rate for a group of people experiencing those conditions. A summary of the comparison between the PMV prediction, assuming three different air speed possibilities, and the actual votes:

- The PMV prediction for data with no elevated air speed resulted in 18 cases that would have been compliant with the ASHRAE Standard (Table 7.2.3), but only 56% of the actual votes were acceptable (10 of the 18 responses).
- The PMV prediction using an elevated air speed for a location between two ceiling fans resulted in 27 cases that would be compliant (the elevated air speed allowed more unacceptably hot cases move to acceptable and a few acceptable move to unacceptably cold (Table 7.2.3); and only 48% of the actual votes were acceptable (13 out of 27)).
- The PMV prediction using an elevated air speed for a location directly under a fan resulted in only six cases when the conditions would have been compliant due to the rest being categorized as unacceptably cool (Table 7.2.4), in other words the PMV was below -0.5. The actual votes that were acceptable were 67%, or four out of the six votes.

Table 7.2.3. ASHRAE 55 Standard PMV model predictions for thermal comfort vs the actual survey votes of occupants. The PMV predictions were estimated for three possible air speed conditions: no elevation in air speed, air speed for a seat located between fans, and air speed for a seat located under a ceiling fan.

ASHRAE 55 PMV model results	Air speed assumption used in model					
	No elevated air speed		Air speed between fans		Air speed under a fan	
	Actual votes	Acceptable Unacceptable	Actual votes	Acceptable Unacceptable	Actual votes	Acceptable Unacceptable
Complied with standard	10	8 Unacceptable	13	14 Unacceptable	4	2 Unacceptable
Did not comply (too hot)	9	10 Unacceptable	0	0 Unacceptable	0	0 Unacceptable
Did not comply (too cool)	0	0 Unacceptable	6	4 Unacceptable	15	16 Unacceptable

The PMV model was not a good predictor of actual thermal comfort per polling of the users. By ASHRAE definition, conditions that comply with the model are expected to have an 80% satisfaction rate but only 48% to 67% of the voting occupants found the conditions acceptable.

In summary, the interior conditions in FROG1 were evaluated with the two thermal comfort models in ASHRAE Standard 55-2017 for Thermal Environmental Conditions for Human Occupancy: ACM and PMV, to determine whether the actual conditions complied with the models. The theoretical results from the models were compared with actual survey responses of the classroom occupants. The ACM was applied when the classroom was naturally-ventilated and the PMV model was used when the air conditioning was ON. Neither ASHRAE 55-2017 model was a good predictor of the survey responses in the tropical climate of Hawai‘i. Cheung *et al.* analyzed the accuracy of the PMV-PPD model using over 50,000 responses from the ASHRAE Global Thermal Comfort Database II and also found the model not to be inaccurate, at the extreme ends of the thermal sensation scale (cold and hot) [5]. Appendix D in the full technical report, referenced below, provides summary notes on their findings.

The full technical report on this assessment “**Ceiling Fan and Thermal Comfort Assessment for Mixed-Mode Classrooms in Hawai‘i**” is available on the HNEI website at <https://www.hnei.hawaii.edu/publications/project-reports/aprises-15>.

References

- [1] American Society of Heating, Refrigerating and Air-Conditioning Engineers. (2017). Thermal environmental conditions for human occupancy (Standard 55). Retrieved from <https://www.ashrae.org/technical-resources/bookstore/standard-55-thermal-environmental-conditions-for-human-occupancy>.
- [2] Parkinson, T., de Dear, R., and Brager, G. (2020). Nudging the adaptive thermal comfort model. Energy and Buildings, 206, 109559.

- [3] Center for the Built Environment. CBE Thermal Comfort Tool. Accessed on September 1, 2020, from <https://comfort.cbe.berkeley.edu/>.
- [4] Tartarini, F., Schiavon, S., Cheung, T., and Hoyt, T. (2020). CBE Thermal Comfort Tool: Online tool for thermal comfort calculations and visualizations. *SoftwareX*, 12, 100563.
- [5] Cheung, T., Schiavon, S., Parkinson, T., Li, P., and Brager, G. (2019). Analysis of the accuracy on PMV – PPD model using the ASHRAE Global Thermal Comfort Database II. *Building and Environment*, 153, 205-217.
- [6] Yu, J., Ouyang, Q., Zhu, Y., Shen, H., Cao, G., and Cui, W. (2012). A comparison of the thermal adaptability of people accustomed to air-conditioned environments and naturally ventilated environments. *Indoor Air*, 22(2), 110-118.